UNIVERSITÉ DE GENÈVE
Département de physique nucléaire et corpusculaire

FACULTÉ DES SCIENCES
Professeure M. Kowalska
Directrice de thèse

UNIVERSITÉ DE MAASTRICHT
Maastricht Centre for Systems Biology (MaCSBio)

FACULTÉ DES SCIENCES ET D'INGÉNIERIE
Professeur R. B. Jolivet
Co-directeur de thèse

γMRI: Towards a Novel Clinical Imaging Modality Using Long-lived Aligned Gamma Emitters

THÈSE

Par

Karolina KULESZ

de Bialystok (Poland)

THÈSE N° 5770

GENÈVE

2023

UNIVERSITÉ
DE GENÈVE

FACULTÉ DES SCIENCES

DOCTORAT ÈS SCIENCES, MENTION PHYSIQUE

Thèse de Madame Karolina KULESZ

intitulée :

«γMRI: Towards a Novel Clinical Imaging Modality Using Long-lived Aligned Gamma Emitters»

La Faculté des sciences, sur le préavis de Madame M. KOWALSKA, professeure titulaire et directrice de thèse (Département de physique nucléaire et corpusculaire), Monsieur R. JOLIVET, professeur et codirecteur de thèse (Maastricht Centre for Systems Biology (MaCSBio), Maastricht University, Maastricht, The Netherlands), Monsieur D. BUDKER, professeur (Helmholtz Institute, Johannes Gutenberg University, Mainz, Germany / Department of Physics, UC Berkeley, Berkeley, United States) et Monsieur D. DELLA VOLPE, professeur associé (Département de physique nucléaire et corpusculaire), autorise l'impression de la présente thèse, sans exprimer d'opinion sur les propositions qui y sont énoncées.

Genève, le 3 octobre 2023

Thèse - 5770 -

La Doyenne

N.B. - La thèse doit porter la déclaration précédente et remplir les conditions énumérées dans les "Informations relatives aux thèses de doctorat à l'Université de Genève".

We owe to the people we loved and lost
to live the lives that they couldn't

To my mother and grandmother…

Abstract

This thesis presents a study of the production and hyperpolarization (HP) of metastable xenon radioisotopes (^{129m}Xe, ^{131m}Xe, and ^{133m}Xe referred to as mXe) and the investigation of the angular distribution of their γ radiation. The thesis is a collection of three research articles, presented in the order which reflects the first steps of the GAMMA-MRI medical imaging modality that is currently under development: production of mXe isomers, their subsequent orientation, and detection of their asymmetric gamma emission:

1. the production of ^{131m}Xe from decay of ^{131}I in Chapter 3;
2. the production of ^{129m}Xe and ^{131m}Xe via neutron activation with thermal neutrons in Chapter 4;
3. a numerical study of the anisotropic distribution of γ-ray emission from hyperpolarized ^{129m}Xe, ^{131m}Xe, and ^{133m}Xe in Chapter 5

   In addition, the production of ^{131m}Xe and ^{133m}Xe at the Radioactive Ion Beam (RIB) facility ISOLDE at CERN, is given in Annex A.

   Finally, the first proof-of-principle experiments devoted to hyperpolarization of ^{129m,131m}Xe and detection of emitted γ radiation are described in Chapter 6.

The above-mentioned studies are a part of the GAMMA-MRI research project aiming to develop a new medical imaging modality based on the physics of magnetic resonance imaging (MRI) and single photon emission computed tomography (SPECT). Preliminary studies of the technique indicate that it could have benefits over existing conventional imaging techniques if a high enough level of ^{129m}Xe, ^{131m}Xe, and ^{133m}Xe spin polarization can be achieved and maintained long enough to acquire changes in γ-ray angular distribution under rf pulses.
The presented thesis is submitted in partial fulfillment of the requirements for the degree of *Philosophiae Doctor* at the University of Geneva. The research presented here was conducted at CERN, under the supervision of professor Magdalena Kowalska and professor Renaud Blaise Jolivet. The work presented in the thesis was performed within an accepted Letter of Intent and Proposal to the ISOLDE and Neutron Time-of-Flight Committee (no. I-205 and P-598). Research funding was provided by CERN's Medical Applications Fund, and since 2021 by the EU Research and Innovation Council within grant no. 964644 (GAMMA-MRI). In addition, the Swiss Government Excellence Scholarship was provided to KK by the Swiss Federal Commission for Scholarships for Foreign Students. Future developments in the scope of the above-mentioned grant will include the fabrication of tailored-to-experiment magnet coils, advancements in the design of the detectors, and further hyperpolarization studies using newly produced samples of mXe.

Acknowledgements

I extend my gratitude to my supervisors, Magdalena Kowalska and Renaud Jolivet, for their vital support, funding and their timely presence. I would like to express my heartfelt thanks to Jochen Ballof, Ulli Köster, Razvan Lica, Sorin Gabriel Pascu, and Stuart Warren for discussions regarding GAMMA-MRI project. Your ideas and enthusiasm have greatly enriched my research journey. Special thanks to Mateusz Jerzy Chojnacki for his assistance in the iodine experiments. I wish you the best for your GAMMA-MRI thesis.

I express my sincere appreciation to the groups of VITO, gamma-MRI, EP-SME-IS, SY-STI, HSE-RP for their consistent support and insightful discussions throughout the experiments and experimental preparations — their design, logistics, and infrastructure. In particular, I am very grateful to Elodie Aubert, Nikolay Azaryan, Mikolaj Baranowski, Ermanno Barbero, Mark Bissel, Mathieu Bovigny, Bernard Crepieux, Matthieu Deschamps, Alexandre Dorsival, Laura Lambert, Peter Plattner, Sebastian Rothe, and Jose Antonio Ferreira Somoza for their invaluable contributions.

I cannot overlook the immense impact of my friends and family on this academic journey. Michal Beme, Florian Dachs, Wanda Gres, James Iddon, Priscillas Kong, Mark Kovacs, Wioletta Kozlowska, Hubert Krzysik, Ewa Kulesz, Tomasz Miller, and Stuart Warren. You have been the steadfast pillars of this narrative. Thank you for your kindness and your unyielding faith in me.
Thank you as well to Kévin André, Niels Stache Bidault, Corti team, David Linton, Willy Pilpay, Ricardo Carlos Puente Rico, Viros Sriskaran, and Francesca Stocker for being integral parts of my PhD journey. Your presence, big or small, has shaped my experience in many different ways.

Geneva, October 2023

Contents

List of Publications

Publication 1

Kulesz K., Azaryan N., Baranowski M., Chojnacki M. J., Köster U., Lica R., Pascu S. G., Jolivet R. B., Kowalska, M. " A Thermal Sublimation Generator of ^{131m}Xe". In the Special Issue of: *Instruments: Medical Applications of Particle Physics.* Vol. 6, no. 4:76 (2022), DOI: 10.3390/instruments6040076.

Publication 2

Chojnacki M. J. (contributed equally), **Kulesz K. (contributed equally)**, Michelon I., Azaryan N., Barbero E., Crepieux B., Lica R., Murawski Ł, Ziemba M., Piersa-Siłkowska M., Vitulova K., Korgul A., Jolivet R. B., Prokopowicz R., Köster U., Kowalska M. "Production of ^{129m}Xe and ^{131m}Xe via neutron activation of ^{128}Xe and ^{130}Xe at the ILL-RHF and NCJB-MARIA high-flux reactors". Submitted to the *Applied Radiation and Isotopes* journal, September 2023.

Publication 3

Kulesz K., Engel R. Y., Jolivet R. B., Kowalska M. "A numerical study of the anisotropic distribution of γ-ray emission from oriented ^{129m,131m,133m}Xe". Submitted to the *Measurement Science and Technology* journal, May 2023.

List of Figures

List of Tables

Chapter 1

Preface

1.1 Motivation and goal

The concept of medical imaging began in 1895 with the invention of the X-ray by a German professor of physics, Wilhelm Rontgen. Since then, a range of medical imaging techniques was developed that can be classified with variable criteria, e.g. spatial resolution, temporal resolution, sensitivity, and hazards for the patient (presence of ionizing radiation or high magnetic field). Table 1.1 presents a comparison of the conventionally used techniques in function of their image quality parameters and effective dose received by the patient. These are some of the parameters considered in evaluating the appropriateness of examinations. Due to their specificity and high sensitivity, Positron Emission Tomography (PET) and Single Photon Emission Computed Tomography (SPECT) methods are applied by the clinician to assess the perfusion and functionality of specific tissues, frequently used in detailed assessments of cancer progression, and of neurological and cardiovascular diseases. While SPECT and PET have the highest sensitivity, Computed Tomography (CT) and Magnetic Resonance Imaging (MRI) have the best spatial resolution. While CT is an affordable go-to diagnostic tool for traumatic injuries necessitating immediate intervention and for specific conditions (osteoarthritis, fractures or cancer staging), MRI is better at very detailed imaging of soft tissues and connective tissue [1].

MRI and its spin-off, functional MRI (fMRI), have become so widely established over the past 50 years mostly due to their advantages relative to other imaging techniques — the absence of ionizing radiation, the fine soft-tissue contrast resolution, the high resolution of images, and the multiplanar imaging capabilities. MRI relies on the same physical principles as the spectroscopic technique of Nuclear Magnetic Resonance (NMR), i.e. on the spin orientation of a nucleus with a non-zero magnetic moment in an external magnetic field [1] and spin manipulation with selective radio frequency (rf) packets. MRI signals are in most cases recorded on ^{1}H nuclei (i.e. protons),

Table 1.1: Comparison of medical imaging techniques. a: Spatial resolution is the minimum distance between two objects or features which the imaging technique can differentiate; b: time of examination is the time needed to acquire enough events to form an image of a dynamic process; c: sensitivity, expressed in molar concentration (mole per liter) refers to the minimum concentration of a molecular probe (e.i. tracer) than can be distinguished from the background using a given technique [2]; d, effective dose, refers to an approximate indicator of a potential detriment from ionizing radiation [3–7].

Technique	^{a}Spatial resolution	^{b}Time of examination	^{c}Sensitivity [M/L]	^{d}Effective dose [mSv]
CT	50–200 μm	minutes	10^{-6}	1–10
PET	1–2 mm	seconds–minutes	10^{-11}–10^{-12}	1–10
SPECT	1–2 mm	minutes	10^{-10}–10^{-11}	1–10
MRI	25–100 μm	minutes	10^{-6}–10^{-9}	0
Ultrasound	50–500 μm	seconds–minutes	10^{-13} if with microbubbles	0

which make up a high fraction of the elements constituting living organisms and which have a nuclear spin different from 0. The relatively large magnetic moment of the proton combined with high gradients of the magnetic field lead to a high spatial resolution of MRI. At the same time, MRI has low sensitivity when compared to other most advanced techniques such as PET or CT, which originates in the semi-equal distribution of higher and lower energy spin states at body temperature, as predicted by Boltzmann equation [1] and with the signal detection via inductive pick-up. The magnetic resonance (MR) signal is greater for substances with high spin density, at low temperatures, and at high magnetic fields [1]. Since it's impossible to change the temperature nor spin density in the context of patient examination, the MRI approach necessitates expensive coils providing a strong high-uniformity main static magnetic field $\vec{B_0}$ to improve the quality of MRI scans. The use of very high magnetic fields requires time-consuming image processing to redress larger image artifacts and raises safety concerns for the subjects [8–10]. There is, thus, a need for an alternative approach to increase MRI sensitivity.

On the other hand, PET and SPECT techniques have high sensitivity and specificity since their signal is based on radiation detection (γ-ray radiation instead of a change of magnetization) and the use of targeted radiopharmaceuticals with high specificity for their target site [11], However, PET and SPECT do not have as high spatial resolution as MRI. In the SPECT technique, both system sensitivity and spatial resolution are primarily determined by the collimators and scintillators used. The spatial resolution of the PET system is determined by a combination of the physical effects of blurring caused by a combination of the physics of the positron emission and annihilation process, the detector response function, and the image reconstruction algorithm [11].

As it is becoming increasingly interesting in clinical applications to accurately localize radiopharmaceutical biodistribution relative to known anatomical structures while also providing detailed anatomical information, recent commercial systems present dual- or trimodality imagining combinations including PET/CT, SPECT/CT, PET/MR and SPECT/MR.

In the scope of the project called GAMMA-MRI (for gamma-detected MRI), an alternative approach was proposed which instead of putting together scans from two modalities, combines the elements of physics behind these modalities. The proposed hybrid technique relies on the hyperpolarization of radionuclei, manipulation of the spins with rf, and observation of resulting change in the asymmetric gamma emission, all in the presence of the gradient magnetic field.

The goal of this thesis is to investigate the feasibility of the GAMMA-MRI technique. Two routes for the production and purification of radionuclides of interest were studied experimentally, an experimental setup was built and used for the first spin orientation experiments, and the relation between their spin orientation and γ-ray asymmetry was addressed theoretically.

1.2 Thesis outline

The next chapter (Ch. 2) describes the key topics brought together to answer the question of the feasiblity of the GAMMA-MRI technique. The overview and the literature review of these key elements is presented in four parts: (1) characteristics of radioisotope of choice (biocompatibility, polarizability, production, feasibility of radiation detection, and of molecular caging), (2) nuclear research facilities of choice, (3) hyperpolarization and detection techniques, (4) review of nuclear orientation advancements. Each of these parts sets the context for the theoretical and experimental framework for Chapters 3–6.

Chapters 3–5 represent the goals of the thesis in the form of 3 publications (each formulated as *Introduction, Materials and Methods, Discussion and Conclusions*). They are presented in the order logical to the steps of the GAMMA-MRI technique:

Publication 1: " A Thermal Sublimation Generator of ^{131m}Xe" focuses on the production of $^{131\mathrm{m}}$Xe from ^{131}I as a possible xenon production route for GAMMA-MRI.

Publication 2: "Production of ^{129m}Xe and ^{131m}Xe via neutron activation of ^{128}Xe and ^{130}Xe at the ILL-RHF and NCJB-MARIA high-flux reactors" demonstrates the production of $^{129\mathrm{m}}$Xe and $^{131\mathrm{m}}$Xe in two research reactors as a possible xenon production route for GAMMA-MRI.

Publication 3: "A numerical study of the anisotropic distribution of γ-ray emission from oriented ^{129m,131m,133m}Xe" compares the predictions of the polarization simulations with the results of the proof-of-principle polarization and detection tests.

The publications are followed by a chapter presenting the proof-of-principle experiments and an annex summarizing a feasibility of the mXe production at CERN-ISOLDE.

This thesis ends with a discussion of the results, a summary of conclusions, and a future outlook in Chapter 7.

Chapter 2

GAMMA-MRI introduction

GAMMA-MRI project aims to develop a hybrid technique combining the advantages of MRI and SPECT/PET in order to provide an imaging modality with the sensitivity of SPECT/PET and spatial resolution of MRI. The goal of the project is structured into a research road map presented in Figure 2.1. Firstly, a fully functional prototype device would be developed, and secondly, the preclinical studies could be conducted with animal or human subjects in the future. The project consists of the following steps:

1. production of metastable xenon radioisotopes (mXe);
2. external spin orientation of mXe, specifically using Spin Exchange Optical Pumping (SEOP);
3. mXe administration into a phantom or subject placed inside a magnetic field;
4. application of MRI sequences to manipulate the spins of the administered nuclei for image construction.
5. acquisition of the change in the angular distribution of emitted γ radiation;

In this chapter, the technical aspects of the GAMMA-MRI technique are detailed by a literature review and presentation of already existing modalities organised in four parts: (1) characteristics of a radioisotope of choice (biocompatibility, polarizability, production, feasibility of radiation detection, and of molecular caging), (2) selected production methods for unstable Xe tracers, (3) Xe hyperpolarization (HP) and detection, (4) nuclear orientation formalism, (5) GAMMA-MRI 3D imaging.

2.1 Xenon properties and applications

Discovered in 1898 by Travers and Ramsay, xenon with the atomic number 54 and symbol Xe, belongs to the noble gas group and was named after the Greek word $\xi\epsilon\nu o\nu$ xénon, meaning *foreign(er)*, *strange(r)*, or *guest* [12]. Xenon possesses distinctive physical and chemical properties that contribute to its diverse applications. With an atomic number of 54 and the symbol Xe, it is a colorless, odorless gas at room temperature. It has a relatively high atomic mass of 131.29 g/mol, a boiling point of -108° C, and a melting point of -111.9° C [13, 14]. Although xenon is renowned for its inertness and low reactivity due to its full valence shell, it can form compounds in specific circumstances, particularly with strongly electronegative elements like fluorine and oxygen.

Xenon itself found applications in various industrial domains. Research literature shows there was particularly intense interest in those industrial applications between the years 2005–2017 driven by the lamps market and by NASA's Evolutionary Xenon Thruster (NEXT) project [15–17]. Xenon lamps are one of high-intensity discharge light sources that take only a few seconds to reach their

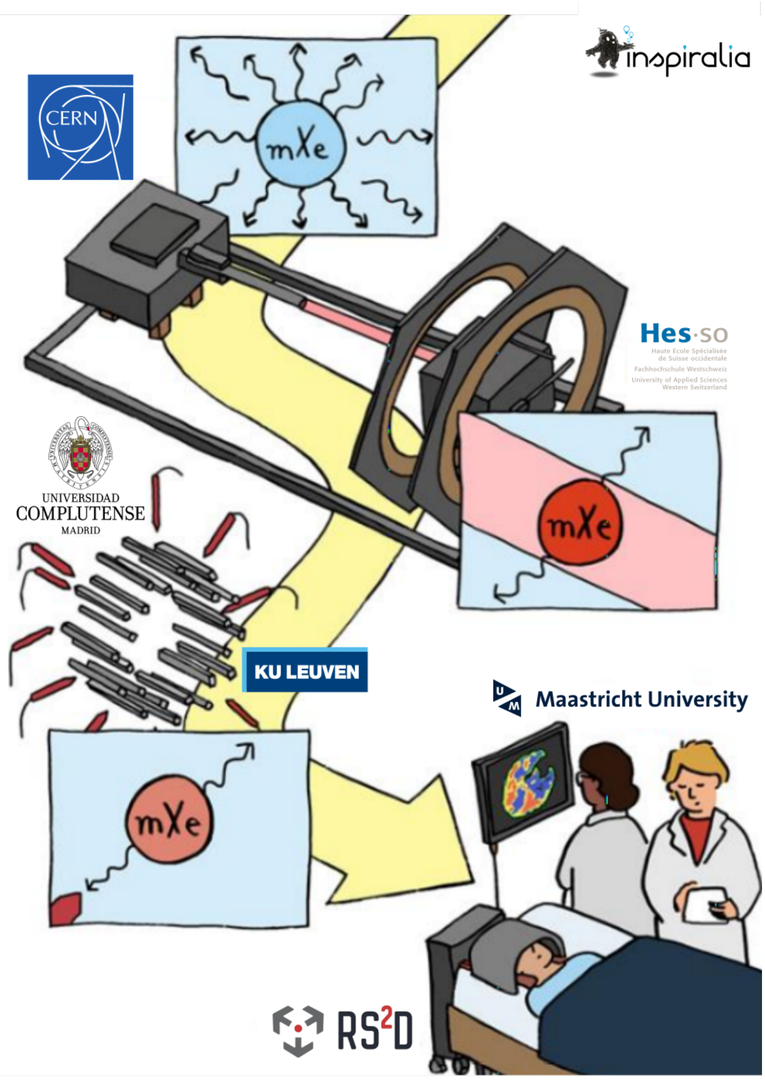

Figure 2.1: The overview of GAMMA-MRI project. Since major funding was received from the European Union’s Horizon 2020 Research and Innovation Program in 2021 under grant agreement No. 964644 (GAMMA-MRI), the GAMMA-MRI project is driven by several academic or research contributors from: CERN-ISOLDE, Haute Ecole Spécialisée de Suisse occidentale, KU Leuven, Universidad Complutense Madrid, and University of Maastricht. Two companies are also involved in the project, RS2D and Inspiralia. Figure courtesy: Inspiralia.

full brightness and offer superior energy efficiency compared to traditional lighting sources as, by not having tungsten filaments, they run at lower temperatures and use less electrical energy [13, 15]. However, due to the global development tendencies towards green growth and low carbon, light sources such as halogen and xenon lamps have been gradually replaced by the light emitting diodes LEDs [15]. In ion thrusters used for spacecraft propulsion, xenon serves as an excellent propellent. Due to its properties such as low ionization potential, high storage density, and chemical inertness, it generates a desirable level of thrust when Xe ions are accelerated and it is well suited for storing on spacecraft [16–18]. One of the newest applications of xenon is in fundamental research as a scintillator in dual-phase xenon time projection chambers (TPC) dedicated to the direct detection of dark matter particles [19].

Next to applications in the automotive industry, xenon is most commonly used in medical imaging by a variety of diagnostic techniques, in anesthesia, and in neuroprotection practices.

Studies have shown that xenon is well-tolerated by biological systems and does not exhibit toxic effects at therapeutic doses [20]. In 1996, Ebert *et al.* [21] and MacFall *et al.* [22] presented the *in vivo* magnetic resonance (MR) images of human lungs through the utilization of hyperpolarized ^{3}He. The subsequent year, Mugler *et al.* extended these investigations by employing ^{129}Xe and further included ^{129}Xe spectra of both the chest and head regions [23]. The isotopes ^{3}He and ^{129}Xe possess a nuclear spin of 1/2, resulting in a two-state nuclear energy level structure when subjected to a magnetic field. Notably, their nuclear polarizations can be significantly increased using Spin Exchange Optical Pumping (SEOP), leading to MR signal enhancements by up to four to five orders of magnitude. The gyromagnetic ratios of ^{3}He and ^{129}Xe, which determine the available MR signal, are approximately 75% and 25% that of 1H, respectively [24]. However, due to its tightly bound electron cloud, helium exhibits negligible solubility in lung parenchyma [25] and blood [26], with an Ostwald solubility coefficient of less than 0.01. In contrast, xenon, with its large and polarizable electron cloud, can dissolve in parenchymal tissue, blood plasma, and red blood cells, as evidenced by Ostwald solubility coefficients of approximately 0.1 [26], 0.09, and 0.2, respectively[27]. In 2013 Mugler *et al.* outlined in [28] a comparison of market pricing of ^{3}He and ^{129}Xe, both used in medical imaging and industry. The natural abundance of ^{129}Xe is 26%, while naturally occurring ^{3}He is almost negligible. At the moment of this estimation, isotopically enriched xenon gas (80% ^{129}Xe) could be purchased for 100 USD per liter. In comparison, ^{3}He could be purchased for a price higher by about an order of magnitude, while a few years earlier it would have been a similar cost. A the same time, the demand for helium is growing due to expanding cryogenics applications.

Stable isotope ^{129}Xe is the most popularly used in hyperpolarized MRI (HP ^{129}Xe MRI) imaging because of its spin ½ and no quadrupolar moment, as detailed in the next paragraph. Patented by Albert, Cates, Happer et al. in 1998 [29] and standardized thereafter, the hyperpolarised MRI using ^{129}Xe can provide detailed structural and functional information about the ventilated lung airspaces [30–32] and is, thus, used in longitudinal studies of disease progression and therapy response. The capacity of ^{129}Xe to dissolve in the bloodstream and its sensitive chemical shift response to its local environment make it possible to observe the exchange of gases in the lungs, the blood flow (perfusion) in the brain and kidneys, and the oxygenation levels in the blood. Most recent applications in lung ventilation examinations include studies of patients with COVID-19 [33, 34].

Xenon gas is also an approved anesthetic drug [35–37]. Li et al. demonstrated in [38] that xenon isotopes with non-zero nuclear spins (^{129}Xe and ^{131}Xe) are less potent to cause unconsciousness than those without (^{132}Xe and ^{134}Xe). It was subsequently shown that the nuclear spin of xenon isotopes is the only factor that dictates the anesthetic properties of these isotopes. After xenon emerged as a neuroprotective agent, the interest to study other inert gases, especially argon, grew. Unlike xenon, argon is more abundant and cheaper to manufacture, and it is not a sedative. However, at the moment, argon's mechanism of action for neuroprotection is not yet well-understood [20]. Through the use of protein crystallography, Xe-protein interactions are studied in the hope to provide further insight into the mechanism of Xe anesthesia and potentially other general anesthetic agents [39, 40].

Stable xenon is also used in Xe-enhanced computed tomography (Xe\CT) for pulmonary ventilation mapping and cerebral perfusion studies [41, 42]. Owing to its radiopacity, xenon attenuates X-rays stronger than air and therefore alters the CT results [43].

Whereas there are seven stable isotopes of xenon (^{126}Xe, ^{128}Xe, ^{129}Xe, ^{130}Xe, ^{131}Xe, ^{132}Xe, and ^{134}Xe) and two very long-lived ones (^{124}Xe and ^{136}Xe), xenon also has a number of unstable isotopes mostly decaying through β and γ-ray transitions. Among them the most frequently utilized is ^{133}Xe, whose first application in pulmonary ventilation and perfusion was described by J.K. Goodrich [44] in 1972. Being an emitter of 80.9 keV γ-rays with a half-life of 5.27 days, ^{133}Xe is used as an inhalation diagnostic agent in SPECT for lung imaging, imaging cerebral blood flow in the brain, and assessing pulmonary function. However, due to its poor spatial resolution, Xe\CT is preferred whenever possible to apply [45].

2.2 Xenon hyperpolarization

The aforementioned noble gases ^{3}He and ^{129}Xe are particularly suitable as inhaled contrast agents for MR imaging. The ^{3}He and ^{129}Xe isotopes have a nuclear spin of 1/2, yielding a two-state nuclear energy level structure in the presence of a magnetic field. Importantly, their nuclear polarisations can be significantly increased using SEOP, facilitating MR signal gains of up to 4–5 orders of magnitude. [24]. MR signal is acquired as a consequence of the changes of the net magnetization vector M of a sample of N protons [46]:

$$\mathbf{M} = \mu(N_{\uparrow} - N_{\downarrow}) \,, \tag{2.1}$$

where $N_{\uparrow}/N_{\downarrow} = e^{2\mu B_0/kT} \approx 1 + \frac{2\mu B_0}{kT}$, thus $(N_{\uparrow} - N_{\downarrow}) = \frac{2\mu B_0}{kT} N_{\downarrow} \approx \frac{\mu B_0}{kT} N$.
B_0 is the externally applied magnetic field, μ is the proton's nuclear magnetic moment, k is the Boltzmann constant, and T is the sample's temperature. The MR signal can be thus enhanced by increasing the externally applied magnetic field or changing the properties of the sample: decreasing temperature, varying the isotopes, and increasing the concentration of atoms of interest. Increasing the signal-to-noise ratio of human body MRI is limited to changing the externally applied field and to introducing contrast agents.

Spin-oriented nuclei are produced using a variety of techniques: optical pumping (and atomic collisions), the capture of polarised neutrons, production mechanism, low-temperature nuclear orientation, and chemical methods from conventional NMR (e.g. DNP). Although HP ^{129}Xe can be produced by dynamic nuclear polarisation (DNP) [47–49], the technique most commonly used to hyperpolarize ^{129}Xe (and other noble gases') nuclei for MR applications is spin-exchange optical pumping (SEOP) [50] with alkali metals (rubidium, cesium or sodium) as the spin-exchange medium.

In SEOP, the nuclei of noble gases become hyperpolarised through spin exchange with alkali metal atoms, which are, in turn, polarised via the absorption of circularly polarised light. The approach has been thoroughly described by Happer and Walker in [50] for stable isotopes of noble gases and by Kitano *et al.* in [51] for radioactive isotopes. Hyperpolarization in GAMMA-MRI relies on the same principles as conventional SEOP with rubidium vapor and stable xenon isotopes undermentioned in this subchapter. The difference is that metastable isomers of xenon are used instead.

The first step in the SEOP process is the polarization of rubidium atoms using circularly-polarised $\sigma+$ (or $\sigma-$) laser light. The units of angular momentum carried by photons of $\lambda = 795$ nm get transferred to the outer-shell electrons of rubidium ^{87}Rb (or ^{85}Rb) [50]. In the D$_1$ transition the electrons are excited from the ^{2}S$_{1/2}$ ground-state, into the ^{2}P$_{1/2}$ excited state. Using a narrow-band diode laser array for the natural isotope mixture of rubidium in gas phase in the presence of magnetic field, allows to generate a number of permissible transitions between the Zeeman levels of the ${}^2\mathrm{S}_{1/2}$ and ${}^2\mathrm{P}_{1/2}$. These excited states decay spontaneously to the ground state in accordance with the $\Delta m_F = 0$ or $\Delta m_F = 1$ selection principle. Through the repetitive pumping cycles, all ground-state sublevels are depopulated by D_1-line absorption, except for the $m_F = +1/2$ level where the population builds up — thereby creating a large population difference - atomic hyperpolarization - in the ground-state Zeeman sublevels [50, 52].

Nitrogen is commonly added into the SEOP mixture as a quenching gas, since rubidium collisions with nitrogen molecules repopulate both ground-state sublevels and prevent fluorescent Rb de-excitation [50] into *dark states* where atoms do not "see" or absorb any light.

Once polarised, the Rb valence electrons can pass on their spin angular momentum to xenon nuclear spins via the spin exchange interaction [52–54] resulting in the nuclear spin orientation of Xe. That spin exchange is possible due to Rb-Xe binary collisions or via the formation of short-lived van der Waals molecules [53] (see Figure 2.2) and can be written as a Hamiltonian including both cited terms [55].

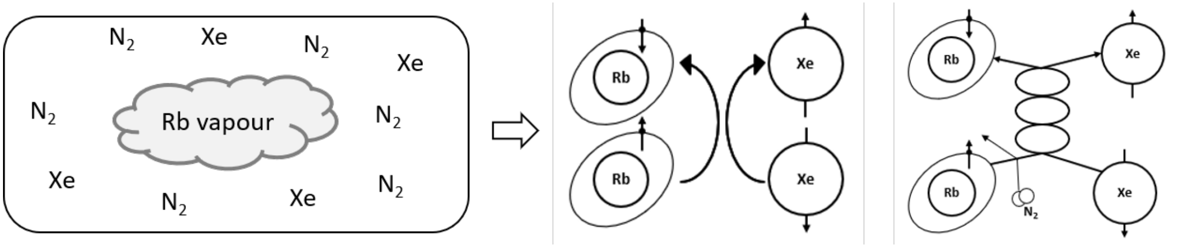

Figure 2.2: Spin-Exchange Optical Pumping diagram. Hyperpolarisation of Xe in a glass container (pumping cell), with a mixture of N_2 and Rb (**left**). Spin exchange occurs via binary collisions (**middle**), or via formation of van der Waals molecules (**right**).

2.2.1 Xenon relaxation time and host molecules

Hyperpolarized MRI presents multiple advantages over traditional MRI methodologies providing greater sensitivity but does come with certain limitations. One of them is the relatively short time over which the hyperpolarization can be maintained. The reason for this is that aside from Rb-Xe binary collisions and van der Waals molecules formation, there exists a number of unwanted collisions, which contribute to the destruction of the spin orientation (i.e. longitudinal relaxation). They can be intrinsic and caused by collisions with other atoms and by formation of Xe dimers, or extrinsic and induced by static magnetic field inhomogeneities and collisions with paramagnetic impurities in the glass walls of the pumping cell. Among these, the latter has the biggest contribution. The relaxation depends on the surface-to-volume ratio of the cell, while Xe dimer formation is pressure-dependent [56, 57]. Therefore, SEOP is most efficient at low molar concentrations of xenon (1-2% of the total gas mixture) and with an appropriate coating of the cell [58–61]. The achieved degree of Xe nuclear polarisation depends on the above-mentioned effects and on the magnetic properties (nuclear spin, magnetic and quadrupole moments) of the Xe nuclei.

The longitudinal relaxation time T_1, also called the spin-lattice relaxation time, is a measure of how quickly the net magnetization vector returns to thermal equilibrium in the direction of B_0 due to the interactions with the surrounding nuclei (lattice). The transverse relaxation time T_2, also called the spin-spin relaxation time is the measure of the spin decoherance in the x-y plane (perpendicular to the vector $\vec{B}$ and caused by the spin-spin interactions). For stable ^{129}Xe, the longest T_1 is for its solid state and ranges from 60 h to 500 h, depending on the level of ^{129}Xe enrichment and the pressure of the gas mixture, i.e. the SEOP conditions of gas prior to freezing [62–64].

In the liquid state, T_1 of ^{129}Xe values typically range from a few to tens of minutes. In [65] Sauer and colleagues showed that T_1 ranged from 12.8±0.2 to 20.5±0.4 minutes in the magnetic field of 0.5 Gauss and from 21.4±0.3 to 25.1±0.3 minutes in the magnetic field of 14 kG. The distribution of values corresponds to different cell surface preparation protocols: longest for clean Pyrex surface and shortest for Pyrex surface treated with gadolinium ions Gd 3^+ possessing large effective magnetic moment of 8.0 μ_B couples strongly to the nucleus of the polarized ^{129}Xe and accelerates relaxation process. In [66] Romalis *et al.* experimentally showed that for low concentrations of stable xenon (mixture in natural abundances) in a mixture with He and N_2 T_1 is about 30 min in the magnetic field of 1.5 kG and T_2 ranges from 20 to 23 min. In the gas state, T_1 values are even shorter and depend on the gas mixture and density. When measured at a Xe density of 0.15 amagat, the intrinsic gaseous $T_1(^{129}\mathrm{Xe})$ is of the order of hours at ambient temperature [57]. The presence of paramagnetic oxygen is primarily responsible for the orders of magnitude faster decay of the hyperpolarized ^{129}Xe signal in the lungs or laboratory system (typically $T_1(^{129}\mathrm{Xe})$ of about 20 s [28]).

For isotopes with an electric quadrupole moment ($I > 1/2$), including ^{131}Xe, ^{129m}Xe, ^{131m}Xe, and ^{133m}Xe (see Table 2.2.1 for nuclear properties [67]), maintaining hyperpolarisation is challenging.

In [68] Stupic *et al.* present a review of relaxation data for ^{131}Xe. In natural abundance xenon mixture, solid ^{131}Xe at temperatures close to the melting point (161 K) has a short longitudinal relaxation time of $T_1 = 200$ ms. With decreasing temperature, the T_1 increases monotonically by three orders of magnitude, up to $T_1 = 390$ s at 9 K [69]. In liquid xenon, the T_1 increases from 40 ms at 161 K to $T_1 = 80$ ms at 250 K and 3 MPa, and to $T_1 = 110$ ms just below the critical point (i.e. 298 K and 5.8 MPa).

In non-polar solvents, the T_1 of ^{131}Xe is typically below 50 ms and it is even shorter ($T_1 < 10$ ms) in polar solvents due to the electric field gradient fluctuations induced by the solvent molecule dipoles.

Table 2.1: Nuclear properties of selected xenon isomers with $I > 1/2$.

Isomer	Nuclear spin I	Magnetic dipole moment $\mu\ [\mu_N]$	Electric quadrupole moment Q $[b]$
^{129m}Xe	$11/2^-$	$-0.8906(12)$	$+0.63(2)$
^{131}Xe	$3/2^+$	$-0.6915(2)$	$-0.114(1)$
^{131m}Xe	$11/2^-$	$-0.994(2)$	$+0.72(3)$
^{133m}Xe	$11/2^-$	$-1.0825(13)$	$+0.76(5)$

The limited hyperpolarization lifetimes of gas phase Xe restrict the time window available for conducting experiments and acquiring data. A promising solution for the prolongation of hyperpolarized state seems to be the use of host molecules. Cryptophanes, a class of cage-like host molecules, exhibit high affinity and selectivity towards xenon atoms solely based on van der Waals forces [70]. It makes them good candidates for encapsulating xenon gas atoms and for maintaining their spin polarization, as numerous studies exploring cryptophanes' design, synthesis, and characterization showed [37, 70].

2.3 GAMMA-MRI's isotope selection and production

The three isomers (i.e. long-lived excited nuclear states) chosen for GAMMA-MRI project shown in Fig. 5.1 with their decay schemes [71–73]. These are: $^{129\mathrm{m}}$Xe, $^{131\mathrm{m}}$Xe, and $^{133\mathrm{m}}$Xe, and we further refer to them as mXe.

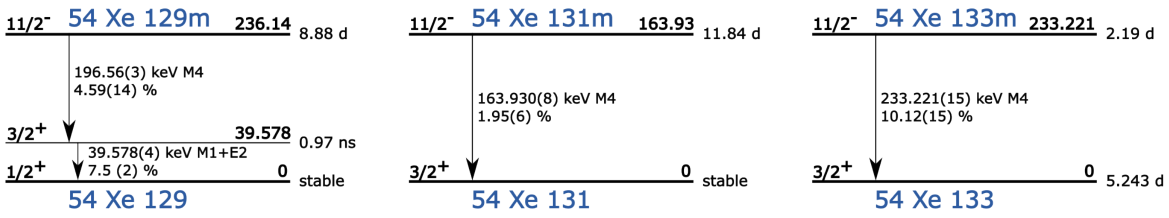

Figure 2.3: Radioactive decay schemes of the isomers $^{129\mathrm{m}}$Xe, $^{131\mathrm{m}}$Xe and $^{133\mathrm{m}}$Xe drawn using [71–73].

They have the nuclear spins of $I = {}^{11}/_{2}$ and decay via a pure $M4$ γ-ray transition to $I = {}^{3}/_{2}$ state, which is either the ground state or the first excited state. Their lifetimes are long enough ($t_{\mathrm{Xe-129m}} = 8.88\,\mathrm{d}$, $t_{\mathrm{Xe-131m}} = 11.84\,\mathrm{d}$, $t_{\mathrm{Xe-133m}} = 2.19\,\mathrm{d}$) that for the potential clinical studies, they would not require the availability of a cyclotron facility near the hospital. They decay with the production of single γ-rays ($\mathrm{E}_{\mathrm{Xe-129m}} = 196.56(3)\,\mathrm{keV}$, $\mathrm{E}_{\mathrm{Xe-131m}} = 163.930(8)\,\mathrm{keV}$, $\mathrm{E}_{\mathrm{Xe-133m}} = 233.221(15)\,\mathrm{keV}$) that are well detected by a range of standard γ-rays scintillators (HPGe, NaI, GAGG(Ce), $\mathrm{La_3Br(Ce)}$).

mXe can be produced by several methods either intentionally or as a by-product. These addressed in the present thesis are:

- As mass-separated beams at Radioactive Ion Beam (RIB) facilities like ISOLDE (**I**sotope **S**eparation **O**nline **De**vice) at CERN, Geneva Switzerland) and at ISOLDE's medical spin-off MEDICIS. Other examples of facilities include: GSI/FAIR (Darmstadt, Germany), GANIL (Caen, France), FRIB at MSU (East Lancing, USA), ISAC at TRIUMF (Vancouver, Canada), or RIBF at RIKEN (Wako, Japan). Annex A provides more details of mXe collections performed at ISOLDE as the feasibility tests.

- As a product of neutron activation of enriched xenon samples at nuclear reactors in laboratories such as Institut Laue-Langevin (ILL, Grenoble, France) or National Centre for Nuclear Research (NCBJ, Swierk, Poland). Chapter 4 presents published findings on the production of metastable isomers of Xe at HRF (High Flux Reactor, ILL) and MARIA (NCBJ) nuclear reactors.

- For $^{131\mathrm{m}}$Xe - via decay of a commercially available radioisotope ^{131}I used in thyroid cancer treatment. Chapter 3 presents for published findings on this method of production of $^{131\mathrm{m}}$Xe.

The feasibility to produce mXe using various nuclear techniques contributes to the accessibility of mXe and thus to the feasibility of GAMMA-MRI. The following section will introduce the nuclear facilities which hosted these production techniques.

2.4 Nuclear techniques for mXe production

The ISOLDE facility is a part of the accelerator complex at CERN where different particles get accelerated to the energies from the vast range of 160 MeV–6.5 TeV. A pulsed proton beam with an energy of 2 GeV and an average intensity up to 2 μA [74] is delivered to ISOLDE from a 4-ring circular accelerator Proton Synchrotron Booster (PS-Booster), as seen in Fig 2.4. Adjacent to the ISOLDE complex and sharing the target area is the MEDICIS facility dedicated to the production of radioisotopes for medical purposes [75].

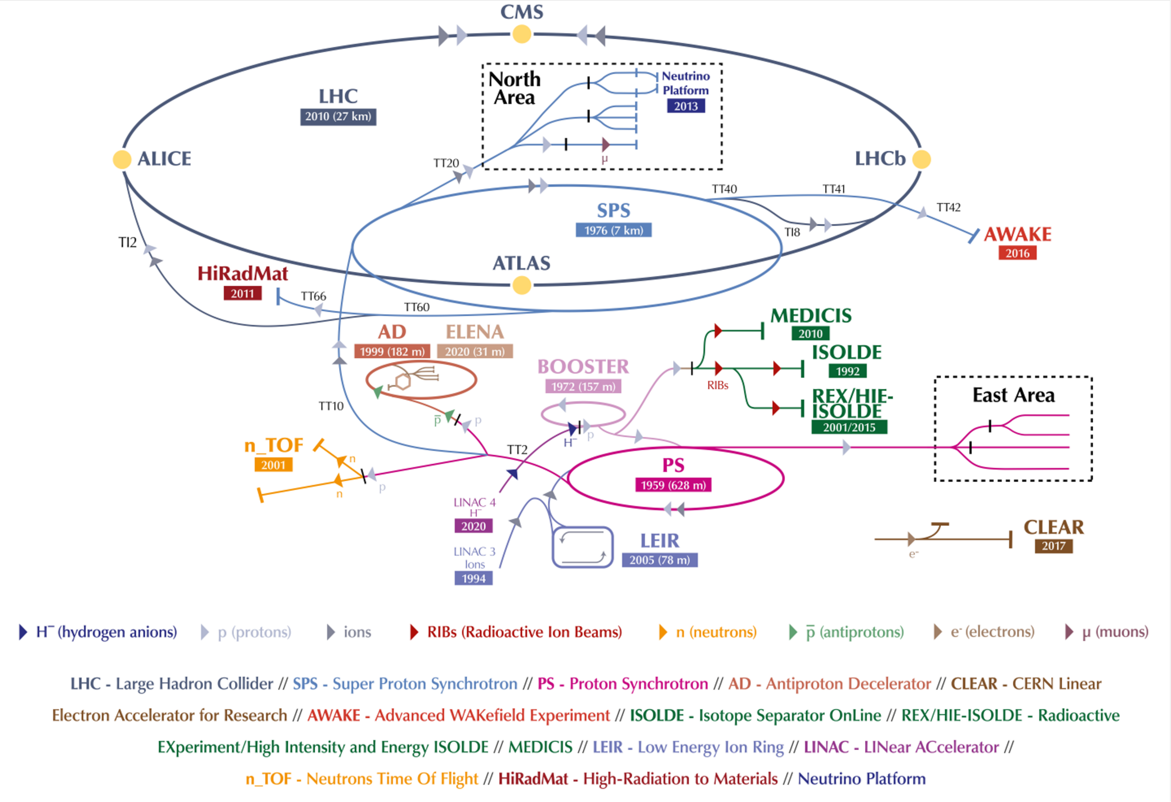

Figure 2.4: CERN accelerator complex. ISOLDE, HIE-ISOLDE, and MEDICIS (labeled green) receive the pulsed proton beam of up to 2 GeV energy from Proton Synchrotron Booster (labeled pink). Figure source: [74].

ISOLDE is a radioactive beam (RIB) facility, where these beams are produced, accelerated, separated, and used in experiments. The facility consists of low-energy ISOLDE (RIBs up to 60 keV) and high-intensity and high-energy ISOLDE (HIE-ISOLDE, RIBs up to 10 MeV/u) (Fig. 2.5).

MEDICIS, ISOLDE, and HIE-ISOLDE share the target area with 2 individual target stations available, known as Frontends. The proton beam impinges onto the target material whose pre-selection depends on the RIB of interest. A wide range of isotopes is produced as a result of fission, spallation, and fragmentation occurring in the target. These reactors are detailed in e.g.[76]. Next, the

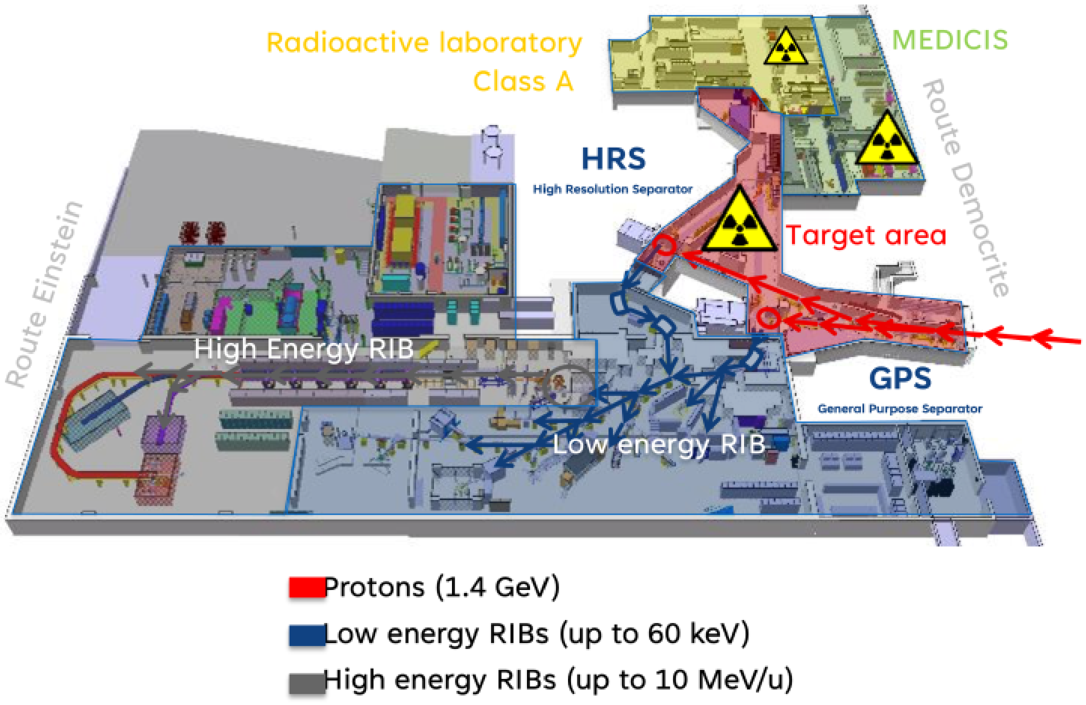

Figure 2.5: MEDICIS, ISOLDE, and HIE-ISOLDE — three facilities taking the proton beam from Proton Synchrotron Booster to target area to experimental installations. Figure source: [75]

target material is heated to about 2000 C, the products are extracted and ionized. From then onward the ion beam is accelerated and mass-separated using magnets at the general purpose separator (GPS) or at the high-resolution separator (HRS), where it can be in addition bunched to minimize beam losses. Certain beams would then travel to the superconducting (SC) linac where they would be further accelerated to be suitable for the HIE-ISOLDE experiments. Others would travel to the installations in low-energy ISOLDE, which is also the case for mXe isotopes for GAMMA-MRI. mXe isotopes, produced from UC$_x$ or ThC$_x$ targets are sent to the General Low Mass beamline (GLM, first to the right in Fig. 2.5) that has convenient infrastructure for implantation of the beams into materials mounted onto a mobile sample holder in the dedicated chamber.

Institute Laue-Langevin is the research facility operating a continuous high-flux (i.e. 1.5 x 10^{15} neutrons per second and per cm^2) reactor. A single highly-enriched (97%) uranium ^{235}U fuel element (10 kg) is used as the reactor's core, controlled by means of neutron-absorbing rods. The rods are gradually withdrawn from the core as the uranium is burned up in the 50-day-long non-stop cycle [77]. Each year ILL runs 3 to 4 cycles i.e. 150–200 days per year of the continuous neutron-beam experiments.

The neutrons produced in the HFR by the fission of uranium are very high-energy neutrons (speed: 20 000 km/s) [77]. They are slowed down by the heavy water acting as the moderator and the fuel element cooling, and by the light water present in the reactor pool. Other elements participating in the energy moderation are 5 safety rods (with the primary function to shut down the reactor in case of an emergency), a hot source (containing a graphite sphere maintained at a temperature of 2600° C), and two cold sources (the largest one containing 20 litres of liquid deuterium). These elaborate components allow facilitate production of neutron energies in the wide range: from hot

(10 km/s) through thermal neutrons (2200 m/s and used for Xe activation) to ultra-cold (10 m/s) neutrons. While slowed-down neutron beams can be guided to a suite of around 40 instruments installed in experimental halls, mXe production via the neutron activation of stable xenon samples (see Chapter 4 for details) happens within the infrastructure illustrated in Figure 2.6.

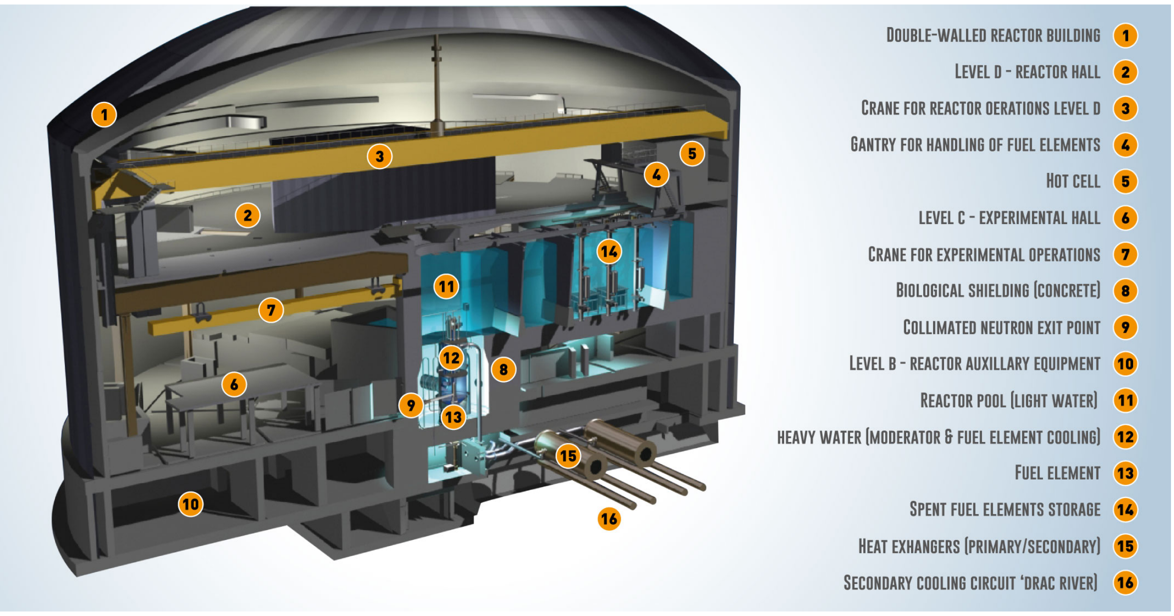

Figure 2.6: HRF infrastructure. Figure source: [77].

Samples, such as xenon ampoules for mXe production, may be lowered into the core from above via thin-walled high-purity-aluminum horizontal tubes (called *shafts*) from above the tank. After several-day-long neutron activation, the samples are lifted from the reactor’s pool, and aluminium capsules in which they were contained are cut open in the hot cell. Retrieved samples are then packaged according to the radioactive material transport regulations and shipped to the recipients, e.g. CERN-MEDICIS or CERN-ISOLDE, where the subsequent handling of activated samples occurs. The cross-section on the reaction of thermal neutrons with Xe "target", the details of samples preparation and activated material handling are presented in Chapter 4.

Third of the discussed methods comprised importing to CERN the mXe generator via the purchase of a commercially available source of ^{131}I routinely delivered to hospitals. The potential of this method is further discussed in Chapter 3 and Chapter 7. ^{131}I and other radioisotopes with medical applications are produced ion the decay chain reactions as highly-enriched ^{235}U, bombarded with neutrons for 100–120 h, fissions into unstable elements with weaker masses that further generate other radioisotopes [78]. This is how ^{99}Mo, ^{99}Tc, ^{113}I, and ^{133}Xe are mass-produced. The irradiated targets are dissolved and the isotopes of interest are chemically separated into separated containers, referred to as cells. The client purchasing a given pharmaceutic is not involved in any of the described procedures.

2.5 Nuclear orientation formalism

When the oriented ensemble doesn't have axial symmetry, the density matrix formalism is used. Elements $\langle I_0 m|\rho|I_0 m'\rangle$ of the density matrix ρ describe of the oriented ensemble. They are found from the Hamiltonian $\mathscr{H}$ describing the interaction of the nucleus with the environment. In thermal equilibrium, the density matrix ρ is:

$$\rho = \frac{e^{-\mathscr{H}/kT}}{\mathrm{Tr}(e^{-\mathscr{H}/kT})} ,$$

where Tr is the trace of the matrix.

The diagonal elements $\rho_{mm'}$ describe the population of the different spin projections on a chosen Z-axis (e.g. external magnetic field) and the non-diagonal elements describe the coupling between the different nuclear substates *m* (i.e. the interaction energies between states).

If $\mathscr{H}$ is diagonal, the orientation is entirely described with the mentioned diagonal elements $\langle I_0 m|\rho|I_0 m'\rangle = p(m)\delta_{mm'}$, where $p(m)$ are the population parameters giving a probability of occupying a substate m. Population parameters are characterised by the Boltzmann distribution [79] and, therefore (for a system out of thermal equilibrium), can be described with spin temperature T_s, which is equivalent to a 'real' temperature in a system in thermal equilibrium. β is a dimensionless parameter related to spin temperature T_s: $\beta = -{}^1\!/_{kT_s}$, where k is the Boltzmann constant. Therefore, the spin orientation can be expressed by means of a dimensionless parameter spin temperature β:

$$p(m) \propto e^{\beta m} .$$

The relative population of m-substate is:

$$p(m) = \frac{e^{-E(m)/kT}}{\sum_m e^{-E(m)/kT}} .$$

In an unoriented nuclear system, for all m: $p(m) = (2I_0 + 1)^{-1}$. Any deviation from that uniform population is nuclear orientation. Polarization f_1 and alignment f_2, detailed in Chapter 5, are two main subcategories of nuclear orientation. The nuclear ensemble is highly-polarized when for any *m*, $p(m) \neq p(-m)$The nuclear ensemble is highly-aligned when for all *m*, $p(m) = p(-m)$ [80].

As described in Chapter 5, polarization and alignment can be expressed as the functions of orientation parameters B_λ, describing the initial oriented state I_0. In the most general form, the $B_\lambda(I)$ are calculated using statistical tensors in the density matrix formalism [81]:

$$B^q_\lambda = \sqrt{2I_0+1}\rho^\lambda_q , \tag{2.2}$$

where q describes the symmetries in the nuclear system, $B^q_\lambda(I_0)$ can be calculated up to the maximum allowed λ:$\{\lambda \in \langle 0, 1, 2.., 2L\rangle\}$, L being the multipolarity of the transition, and $\rho^\lambda_q(I_0)$ – statistical tensors obtained from the density matrix ρ of I_0:

$$\rho^\lambda_q = \sqrt{2\lambda+1}\sum_m (-1)^{I_0+m} \begin{pmatrix} I_0 & I_0 & \lambda \\ -m' & m & q \end{pmatrix} \langle I_0 m|\rho|I_0 m'\rangle .$$

The case of Eq. 2.2 with the presence of the axial symmetry of the nuclear orientation discussed in this manuscript is detailed further in Chapter 5. The general expression for the angular distribution of radiation emitted in a particular direction θ:

$$W(\theta) = \sqrt{2I+1} \sum_{\lambda,q,q'} \rho_q^\lambda \, A_{\lambda,q} \, D_{q,q'}^\lambda(\mathbf{S'} \to \mathbf{S}) \ ,$$

where $D_{q,q'}^\lambda(\mathbf{S'} \to \mathbf{S})$ transforms the reference frame from the one of laboratory system to the one of radiation.

The equation for $W(\theta)$ takes a particular form for the angular distribution of γ-radiation and of β decay. Their $W(\theta)$ functions are illustrated in Figure 2.5. β particles are emitted from the spin-polarized $\left(f_1(I) = -B_1(I)\sqrt{\frac{I+1}{3\,I}}\right)$ nuclei with $I > 0$ in the direction of $\vec{\mathbf{B}}$. γ-rays are emitted from the spin-aligned $\left(f_2(I) = B_2(I)\sqrt{\frac{(2I+3)\,(I+1)\,(2I-1)}{45\,I^3}}\right)$ nuclei with $I > 1/2$ in the plane perpendicular to $\vec{\mathbf{B}}$ ($\vec{\mathbf{B}}$ is normal to the plane of $W(\theta)$).

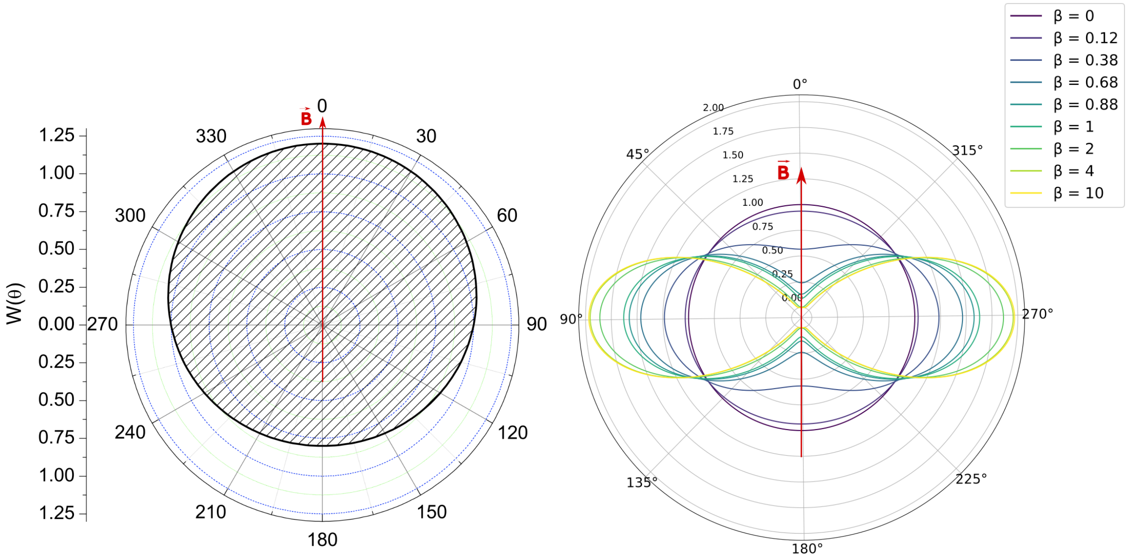

Figure 2.7: $W(\theta)$ for the angular distribution of β decay (left, Figure source: [82]) and γ-radiation (right).

Thus, the angular distribution of $\beta^\pm$ in allowed $\beta^\pm$-decay from an oriented nuclear spin system with $I_0 > 0$ has only the terms with $\lambda = 0$ and 1 which contribute to the observed decay asymmetry:

$$W(\theta) = 1 + \sqrt{2I+1} \, \rho_0^1 \, A_1(\beta^\pm) \, \cos\,\theta \ .$$

The angular distribution of γ-radiation emitted from an oriented nuclear spin system with $I_0 > 1/2$ has only terms with even λ ($\lambda = 0, 2, 4, ...2L$), as further described in Chapter 5.2.2:

$$W(\theta) = 1 + \sum_{\lambda\ even} U_\lambda \, G_\lambda \, A_\lambda \, B_\lambda(I_0) \, Q_\lambda \, P_\lambda(\cos\,\theta) \ , \tag{2.3}$$

where perturbation coefficient G_λ, deorientation coefficients U_λ, and orientation parameters $B_\lambda(I_0)$ are determined from ρ_q^λ, and the function $D_{q,q'}^\lambda(\mathbf{S'} \to \mathbf{S})$ simplifies to the solid angle correction factor Q_λ and to spherical harmonics functions $P_\lambda(\theta)$ — Legendre polynomials $P_\lambda(\theta)$ present in Eq. 2.3 can be derived as a special case of spherical harmonic.

Q_λ compensates for the finite solid angles between the source and detector(s). G_λ accounts for the intermediate state perturbations, thus for the change of the observed initial state I_i. G_λ is present if state I_i has a lifetime τ and the perturbation (interaction of nuclear moments with the electromagnetic fields of the environment) a frequency of at least τ^{-1}. Deorientation coefficient U_λ accounts for an effect of the unobserved intermediate radiation for $I_0 \rightarrow I_i$ transition. Angular distribution coefficient A_λ describes the observed radiation and depends on the (multipole) character of the observed radiation. $P_\lambda(\theta)$ is the Legendre polynomial of order λ, and θ is the angle between radiation and z-axis.

2.6 GAMMA-MRI 3D imaging

In the following text, the concept of envisaged 3D imaging in GAMMA-MRI is laid out using the same MATLAB simulation reference as shown in Chapter 5 in Fig.5.3. The simulation parameters — the size and the distance of the detectors, the activity of the oriented source, etc. — are referenced in Chapter 5 and in Fig. 2.8.

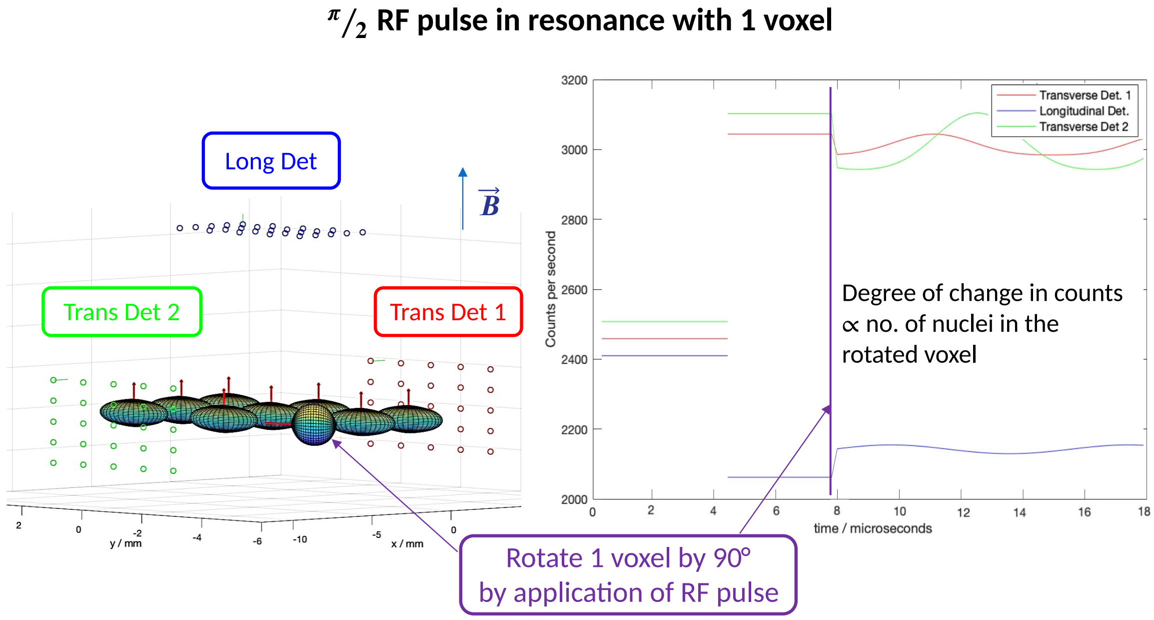

Figure 2.8: MATLAB simulations: three γ-ray detectors distributed in two planes (blue in x-y plane; red and green in y-z) around an ensemble of γ-ray emitting xenon nuclei in nine voxels. This configuration of detector placement is ideal to register the asymmetry of the radiation. The size of the detector was set to 9x9x1 mm^3 and the detection probability to 10%. The time of static state recording is 32 μs with 160 steps of 0.2 μs each. The activity of the sample set to 30 MBq. The spherical and elliptical shapes of non-zero dimensions are the 3D reconstructions of angular distribution γ-ray emission from the point-like source that is in its center and is contained in one voxel. $^{\pi}/_{2}$ rf pulse in resonance with 1 voxel of highly aligned mXe atoms is applied.

Like in a conventional MRI, a slice selection of the examined volume (voxel) is done with the presence of gradient magnets. A magnetic field gradient causes the center frequency f_c of each slice to vary by position. At the same time, an RF pulse whose frequency components match the narrow range of frequencies contained in the desired slice is applied, which assures that only nuclei within the chosen slice are excited. A dedicated sequence called the Cates-Miller-Zheng (CMZ) sequence [83] was designed by Zheng *et al.* for the fast-relaxing mXe, where standard sequences might not be optimal. This pulse sequence can be applied by GAMMA-MRI to already aligned mXe nuclei. Figure 2.8 represents the basics of GAMMA-MRI imaging from nine voxels. For simplicity $\pi/2$ instead of CMZ was shown in the diagram. Given an equidistant placement of the γ-ray detectors from the source with no nuclear alignment, the recorded count rate would be equal for three detectors. In the case of nuclear alignment, the γ-ray count rate increases in the detector placed transversely to $\vec{\mathbf{B}}$ (i.e. red and green in y-z plane) and decreases in the detector longitudinal to $\vec{\mathbf{B}}$, i.e blue in x-y plane. This is observed as a change in the count rate corresponding to the red and green detectors versus the blue detector. A $\pi/2$ pulse applied to one voxel rotates the spin of the ensemble by $\pi/2$.

The degree of change in the count rate corresponds to the number of nuclei in the rotated voxel. In addition, due to the spins' rotation, the Larmor precession (and in the presence of a transverse rf field $\vec{B_1}$, also the Rabi oscillations) present in the oriented system can be observed.

The Larmor precession is visible in the transverse detectors as the rotated spins in the voxel precess around the holding field $\vec{\mathbf{B}}$ at the Larmor frequency.

Publications

Chapter 3

A Thermal Sublimation Generator of ^{131m}Xe

Karolina Kulesz [1,2], Nikolay Azaryan [1], Mikołaj Baranowski [3], Mateusz Jerzy Chojnacki [1,2], Ulli Köster [4], Razvan Lica [1,5], Sorin Gabriel Pascu [1,5], Renaud Blaise Jolivet [6], Magdalena Kowalska [1]

Published in the Special Issue of *Instruments. Medical Applications of Particle Physics*, November 2022, volume 6, issue 4, article no. 76. DOI: 10.3390/instruments6040076.

Abstract

Stable and unstable isotopes of the heavy noble gas xenon find use in various medical applications. However, apart from ^{133}Xe, used for Single Photon Emission Computed Tomography, radioactive isotopes of xenon are currently complicated to obtain in small quantities. With the GAMMA-MRI project in mind, we investigated a thermal sublimation generator of the long-lived excited state (isomer) $^{131\mathrm{m}}$Xe. This production method utilized the decay of ^{131}I, obtained commercially from a hospital supplier in the form of Na^{131}I powder. Heat treatments of the Na^{131}I powder and cryogenic trapping of released $^{131\mathrm{m}}$Xe allowed us to collect up to 88% of the produced xenon. Our method provides an isomeric mixture of $^{131\mathrm{m}}$Xe and ^{131}Xe. With improvements in scalability and chemical purification, this method could be a cost-effective source of $^{131\mathrm{m}}$Xe for small-scale experiments.

3.1 Introduction

Stable and radioactive isotopes of xenon are used in large quantities in medical imaging and Nuclear Magnetic Resonance (NMR) applications [84–88]. Xenon has several important qualities [84]. First, it is inert, and does not interact chemically with the research subject, or sample [84]. Second, the amplitude of the NMR signal acquired from xenon can be increased by several orders of magnitude if xenon is hyperpolarized by colliding it with optically pumped alkali atoms using Spin Exchange Optical Pumping (SEOP) [89]. In addition, xenon passively crosses the blood brain barrier, and can serve as a contrast agent to image the uptake of the inhaled gas into brain tissue. This can be used effectively for stroke diagnosis for instance [90]. The most widely used stable isotopes of xenon are

---

[1] CERN, Espl. des Particules 1, 1211 Meyrin, Switzerland
[2] Faculty of Science, University of Geneva, Quai Ernest-Ansermet 24, 1211 Geneva, Switzerland
[3] Faculty of Physics, Adam Mickiewicz University, Umultowska 85, 61-614 Poznan, Poland
[4] Institut Laue-Langevin (ILL), 71 Avenue des Martyrs, 38000 Grenoble, France
[5] Horia Hulubei National Institute of Physics and Nuclear Engineering (IFIN-HH), Reactorului 30 St., 077125 Bucharest-Magurele, Romania
[6] Maastricht Centre for Systems Biology (MaCSBio), Maastricht University, Paul-Henri Spaaklaan 1, 6229 EN Maastricht, The Netherlands

the nuclear ground states of ^{129}Xe and ^{131}Xe. They are typically used in NMR studies of materials, and for Magnetic Resonance Imaging (MRI) of the lungs [68, 91–93]. Unstable ^{133}Xe is used in Single Photon Emission Computed Tomography (SPECT) for the diagnosis of pulmonary diseases [94, 95]. The physical half-life of ^{133}Xe (5.3 d) makes it easy for radiopharmaceutical suppliers to manufacture and deliver it [95].

In the GAMMA-MRI project [96], we aim at developing a new imaging technique based on the MRI response from polarized unstable, SPECT-compatible nuclei. Our first test cases are radioactive xenon isomers, in particular the long-lived $^{129\mathrm{m}}$Xe, $^{131\mathrm{m}}$Xe, and $^{133\mathrm{m}}$Xe isomers. Optimising SEOP polarization of these isomers is one of the key components of the GAMMA-MRI project. For this purpose, it is advantageous to use the isomer that has the longest half-life, and that can be produced in an affordable way.

Here, we explore a generator of $^{131\mathrm{m}}$Xe ($t_{1/2} = 11.84$ d), via decay of a ^{131}I source ($t_{1/2} = 8.02$ d) obtained commercially from a hospital supplier. ^{131}I, like ^{133}Xe in its ground state, is in high demand by hospitals and thus can be procured from radiopharmaceutical companies [97, 98]. Both ^{131}I and ^{133}Xe can be produced from ^{235}U fission, upon ^{235}U irradiation with neutrons in nuclear reactor facilities: $^{235}\mathrm{U(n,f)}^{133}\mathrm{Xe}$ and $^{235}\mathrm{U(n,f)}^{131}\mathrm{I}$ [99]. To isolate and collect these isotopes, the ^{235}U target is dissolved, and the solution is separated into cells containing specific chemically active elements [78]. This approach offers several benefits: a flexible delivery schedule (medical ^{131}I is available > 350 d/yr), established supply routes (to hospitals), and a relatively low cost for samples at the delivery point.

$^{131\mathrm{m}}$Xe generators based on ^{131}I have been investigated before. For instance, P. Bedrossian [100] used a palladium metal surface to adsorb ^{131}I from a solution. That generator was then connected to a vacuum-tight setup placed vertically: with generator atop and a set of glass spheres underneath. Produced $^{131\mathrm{m}}$Xe was collected in the bottom-most glass sphere immersed in the liquefied air, and the sphere was separated by sealing it off with a flame torch. In [101], a $^{131\mathrm{m}}$Xe generator is described, where a ^{131}I solution was precipitated onto a fibreglass filter as palladium(II) iodide $\mathrm{PdI_2}$, inside a commercially available syringe filter. The syringe was connected to a carrier gas which, after the desired quantity of $^{131\mathrm{m}}$Xe was produced, would sweep the $^{131\mathrm{m}}$Xe from the syringe filter into another apparatus for γ-ray spectroscopy. Both of these generators reported near unity $^{131\mathrm{m}}$Xe production efficiency. Finally, in a more recent publication [102], the production of $^{131\mathrm{m}}$Xe from ^{131}I is mentioned but no details are given. However, to the best of our knowledge, $^{131\mathrm{m}}$Xe production from Na^{131}I powder has not been reported yet.

Here, we fill this gap and report on $^{131\mathrm{m}}$Xe production from a Na^{131}I powder. A solid state sample is preferred for the GAMMA-MRI project. Specifically, it should introduce less water into the SEOP cell than a Na^{131}I solution. It is important for successful polarization to eliminate all sources of water that could oxidize rubidium used in the SEOP process. The objective of the present work was thus to establish the most suitable conditions to extract $^{131\mathrm{m}}$Xe from a Na^{131}I salt, and to optimize the collection efficiency.

3.2 Materials and Methods

Production of $^{131\text{m}}$Xe from ^{131}I decay involved the following procedure: (i) procurement of the ^{131}I source in the form of powder encapsulated in a gelatin shell, (ii) γ-ray spectroscopy of the ^{131}I source upon arrival at CERN, (iii) Na^{131}I powder transfer from its gelatin shell in a quartz tube and γ-ray spectroscopy of both constituents, (iv) placement of the powder in the experimental installation for decay, (v) collection of $^{131\text{m}}$Xe from the Na^{131}I powder at ambient temperature, or after heating, and finally (vi) $^{131\text{m}}$Xe γ-ray spectroscopy. Three $50(5)$ MBq Na^{131}I samples were purchased from Curium Pharma (Curium Pharma, Paris, France)—a supplier who could regularly deliver Na^{131}I source at high radionuclidic purity (see subsection 3.2.2). The samples were processed according to the procedure described above.

3.2.1 Characteristics of the Parent Source

The parent nucleus for the $^{131\text{m}}$Xe generator is ^{131}I. The following characteristics were considered: the half-life $t_{1/2}$ and the branching ratio BR_m for the transition to $^{131\text{m}}$Xe, the isotopic and chemical purity of ^{131}I, the state of ^{131}I (solid or liquid), its availability, the associated radiological risks, and finally the cost of the ^{131}I source and of its delivery.

^{131}I ($t_{1/2} = 8.02\,\text{d}$) is a beta-gamma (β^-, γ) ray emitter, which decays to the isomer $^{131\text{m}}$Xe ($t_{1/2} = 11.84\,\text{d}$), and to the ground state ^{131}Xe (stable). While the dominant part of β^- decays of ^{131}I feeds the ground state $^{131\text{g}}$Xe, a small fraction of BR_m = 1.09(9)% feeds the isomer $^{131\text{m}}$Xe [72].

The amount of collected $^{131\text{m}}$Xe nuclei is, thus, the result of two competing processes, a source term from the decay of ^{131}I, and a sink term due to $^{131\text{m}}$Xe decay. The mathematical model describing isotopes in the decay chain ($^{131}\text{I}>^{131\text{m}}\text{Xe}>^{131}\text{Xe}$) as a function of time is Bateman's equation [103], which for ^{131}I gives:

$$A_{\text{mXe}}(t) = \lambda_{\text{mXe}} N_{\text{mXe}}(t) = BR_m N_{\text{I}_0} \frac{\lambda_\text{I}\lambda_{\text{mXe}}}{\lambda_{\text{mXe}} - \lambda_\text{I}} (e^{-\lambda_\text{I} t} - e^{-\lambda_{\text{mXe}} t}) + \lambda_{\text{mXe}} N_{\text{mXe}}(0) e^{-\lambda_{\text{mXe}} t} \tag{3.1}$$

with A_{mXe}(t) activity of $^{131\text{m}}$Xe at time t, N_{I_0} the number of ^{131}I nuclei at t_0, decaying into N_{mXe}(t) $^{131\text{m}}$Xe nuclei at the rate λ_I over a period t and with the branching ratio BR_m. Additionally, $^{131\text{m}}$Xe decays into stable ^{131}Xe at the rate λ_{mXe} in time *t*. $\lambda_{\text{mXe}} N_{\text{mXe}}(0) e^{-\lambda_{\text{mXe}} t}$ describes the decay of $^{131\text{m}}$Xe present in the system at $t = 0$.

Figure 3.1 illustrates Eq. 3.1 assuming $N_{\text{mXe}}(0) = 0$ and the initial activity of ^{131}I $A_I(0)$ = 1 MBq. The figure presents the activity in function of time: the decay of ^{131}I (activity in black, uncertainty in grey) in MBq, and the production and decay of $^{131\text{m}}$Xe (activity in red, uncertainty in yellow) in kBq. The error bars comprise the errors of the decay constant and branching ratio. The optimum waiting time, when the daughter activity is maximal, can be calculated analytically by finding the maximum t_{opt} of function in Eq.3.1. After transformation, the equation reads:

$$t_{opt} = \frac{ln \frac{\lambda_\text{I}}{\lambda_{\text{mXe}}}}{\lambda_\text{I} - \lambda_{\text{mXe}}} \tag{3.2}$$

and t_{opt} = 14.0 days. The maximum $^{131\text{m}}$Xe activity is 3.23(1) kBq and it corresponds to 0.324(1)% of the initial activity of the ^{131}I source placed in the experimental setup.

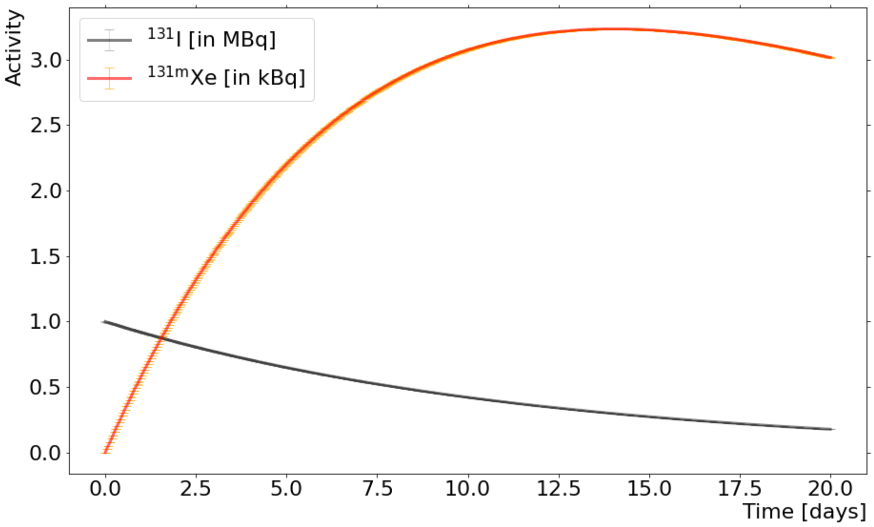

Figure 3.1: Calculated $^{131\mathrm{m}}$Xe activity (red) vs time. A source of ^{131}I (activity in black, uncertainty in grey) decays into $^{131\mathrm{m}}$Xe (activity in red, uncertainty in yellow), which itself decays into ^{131}Xe (stable, not shown). The error bars comprise the errors of the decay constant and branching ratio. The maximum activity plateau for $^{131\mathrm{m}}$Xe is at day 14 (Eq. 3.2).

3.2.2 ^{131}I Source Manufacturing

Radiopharmaceutical preparation standards are defined in European Pharmacopoeia [104], and implemented by all manufacturers in Europe. They define the quality of ^{131}I medication, including the chemical and radionuclidic purity, and define accepted physical forms and dosage. The radionuclidic purity of ^{131}I is $\geq 99.9\%$ with ^{133}I, ^{135}I and other impurities $\leq 0.01\%$.

The ^{131}I bulk solution is delivered on a regular basis to our supplier Curium Pharma by the processors of reactor-irradiated targets, which extract the ^{131}I from targets. The solution already includes excipients, added to prevent the escape of significant amounts of dissolved volatile iodine [105]. In addition, those excipients are necessary to adjust the pH of the ^{131}I bulk solution, and to flavour the medicine for patients. For our application however, the additional ingredients can indirectly affect the purity of the collected $^{131\mathrm{m}}$Xe, as detailed in Section 3.3.

Curium Pharma provides ^{131}I directly to hospitals and other partners (e.g. CERN) in a liquid NaI solution (shipped in a glass vial), or in the solid state (NaI powder in a gelatin capsule, to be swallowed by patients). Na^{131}I in the capsule format used in this work is prepared by adding a small volume of the solution to a NaI powder placed in a gelatin shell. Figure 3.2 shows one such capsule and the powder, in scale.

3.2.3 Purchase of ^{131}I and Radioactive Decay

For every experiment, a single capsule containing Na^{131}I was delivered to CERN in a lead pot in a type-A package (Figure 3.2). The manufacturer specifies the activity to 10%, i.e. $50(5)$ MBq. Upon arrival, the actual ^{131}I activity in the capsule was determined with a n-type calibrated Extended Range (XtRa) Coaxial Ge detector (model GX6020, CANBERRA, Montigny-Le-Bretonneux, France) with a thin carbon window (Table 3.2). As an acquisition system, we used a multichannel analyzer model ASPEC-927 and Maestro-32 software (AMETEK ORTEC, Oak Ridge, USA). Remote manipulators with

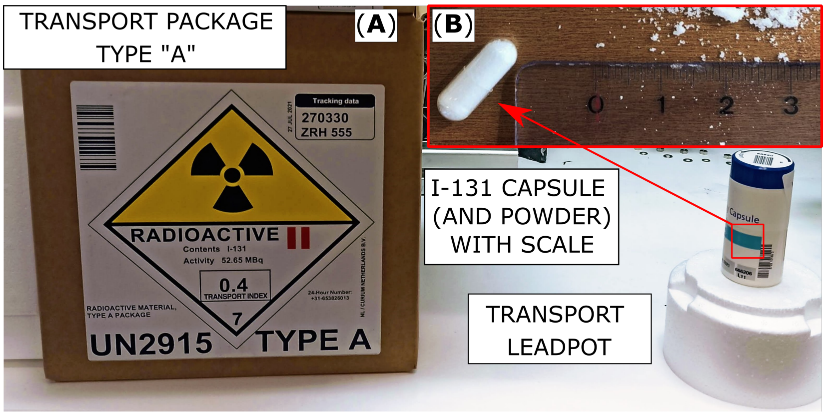

Figure 3.2: Standard elements of the transport packaging of the radiopharmaceutical ^{131}I. (**A**) Type-A package. The lead container, held securely in polystyrene foam inside a cardboard box. (**B**) Gelatin capsule and Na^{131}I powder.

machined grooves were used to open the gelatin shell, and to transport its content into a dedicated borosilicate glass tube. Figure 3.3 presents the tools used for the safe handling of the capsule. These were necessary to avoid exposure to a large radiation dose received directly to the operator's fingers.

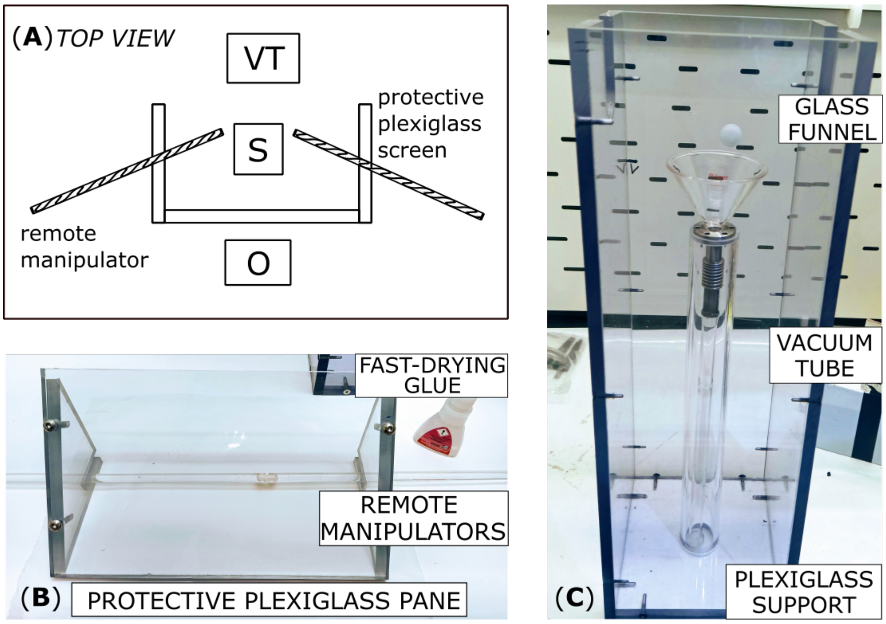

Figure 3.3: (**A**) Schematic of the opening setup. Operator (O) stands behind the protective panel and manipulates the source (S) with remote manipulators. The source is transferred to a glass tube that is then installed in the vacuum-tight experimental setup (labelled vacuum tube or VT in the schematic). (**B**) The tools for safe handling of the source included: the acrylic remote manipulators with grooves machined to the size of the gelatin shell, the acrylic shielding panel (thickness 1 cm) stopping beta particles from the ^{131}I source, and the fast-drying glue necessary for the rapid attachment of the gelatin shell to the grooves in the acrylic manipulators. (**C**) The acrylic support for the vacuum tube: a borosilicate glass annealing tube with a CF 16 flange. A glass funnel aids powder transfer and minimizes transfer losses.

Using the acrylic manipulators with a drop of fast drying glue *UHU Flextube Colle sans solvant* to attach the gelatin shell, the capsule was open into two halves. With the acrylic manipulators, the Na^{131}I powder was then transferred from the gelatin capsule via a glass funnel into the borosilicate glass annealing tube (labelled VT or vacuum tube in Figure 3.3). γ-ray spectroscopy on the annealing vial (Figure 3.6) containing the powder provided a measurement of the activity of the transferred powder, and of the potential losses due to capsule manipulations (Table 3.2). Next, the tube was installed in the experimental setup for xenon production (Figure 3.4).

3.2.4 ^{131}I Extraction and $^{131\mathrm{m}}$Xe Collection

The setup for $^{131\mathrm{m}}$Xe collection (Figure 3.4) consisted of ultrahigh vacuum (UHV) elements (CF flanges, needle valves and gate valves). In addition, the setup contained the annealing tube with Na^{131}I and a collection vial for $^{131\mathrm{m}}$Xe, both made of borosilicate glass.

An UHV valve was mounted between the annealing tube and rest of the setup. The tip of the tube which contained the transferred Na^{131}I powder was inserted into a furnace equipped with temperature stability controls (measured temperature drift $\leq 2\,^{\circ}$K). The Na^{131}I powder was heated to up to $400\,^{\circ}$C to allow for xenon to diffuse out of the powder. Each heating treatment lasted one hour, with increasing temperatures for consecutive treatments. The collection vial was mounted vertically in the setup. The free space below it was used to place a container with liquid nitrogen—a cryotrap—for $^{131\mathrm{m}}$Xe collection. Collections were performed after every one-hour-long heat treatment.

The experimental setup was evacuated to 10^{-6} mbar with a turbomolecular pump, and an oil-free scroll pump. Two pressure gauges were integrated into the system to cover the pressure range from UHV to atmospheric pressure. A full-range vacuum gauge (labelled G1 in the bottom of Figure 3.4) housing two sensors—a Pirani gauge and a cold-cathode ionization gauge—was installed between the pumping system and the chamber in contact with xenon. This location was optimal for a wide range of vacuum regimes, but it was not used in the presence of xenon, due to the ionic pumping effect. A capacitance diaphragm vacuum gauge (labelled G2 in the bottom of Figure 3.4) was installed at the interface between the gas diffusing from the annealing vial and the collection vial. That gauge measured the direct force on the diaphragm, and could consequently measure the pressure independently of gas type and concentration. In addition, it did not pump xenon like an ionization gauge would.

After each collection, the valve to the collection vial was closed and the cryotrap was removed to allow *in situ* γ-ray spectroscopy to characterize how collections depended on the temperature of the heating cycles. We used two γ-ray detectors. The first one was a 2x2 inch LaBr$_3$(Ce) crystal encapsulated in aluminium. Thin aluminium housing and a glass light guide allowed for acquisition of 29.8 keV X-rays from decay of $^{131\mathrm{m}}$Xe to the ground state (branching ratio 29.3%). The latter was a n-type Standard Electrode Coaxial Ge (SEGe) detector, model GC7020 (CANBERRA), with an aluminum window blocking X-ray radiation (including at 29.3 keV), but sensitive to higher energy radiation ($^{131\mathrm{m}}$Xe: 163.9 keV and ^{131}I: 364.5 keV). We used the CAEN DT5730 (8 Channel 14 bit 500 MS/s Digitizer) with the PHA firmware and Compass software [106]. The distance between the center axis of the collection vial and the detectors was 55 mm and 80 mm, respectively, for the LaBr$_3$(Ce) and the HPGe detector. A 10-cm-thick lead shielding was placed between the Na^{131}I source and the detectors to reduce the ^{131}I background, and to prevent saturating the HPGe preamplifier due to

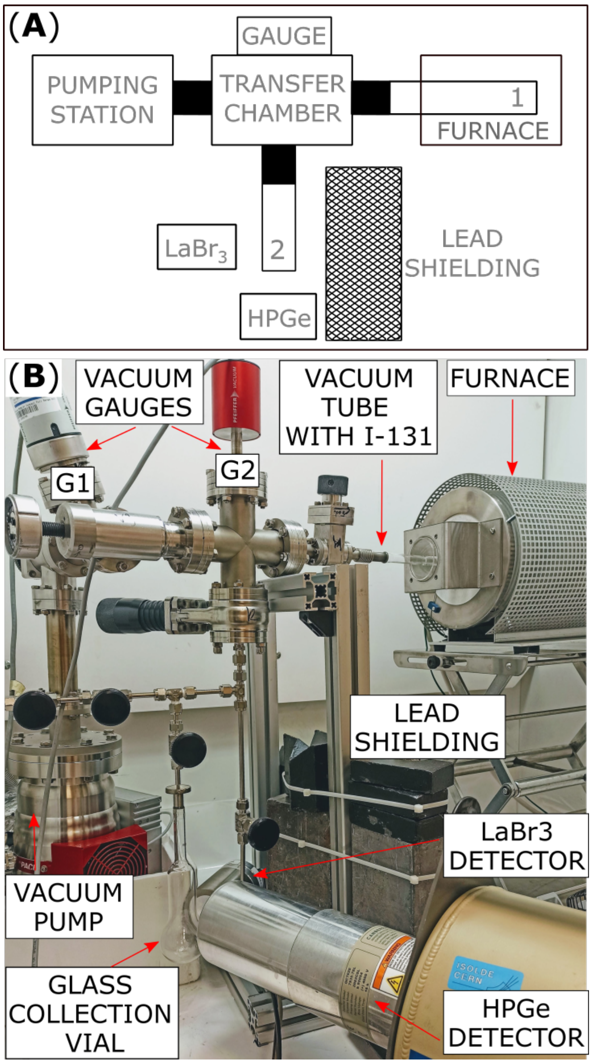

Figure 3.4: (**A**) Schematic of the extraction setup. The Na^{131}I source (labelled 1), is in the glass annealing tube inside the furnace. The collection vial for $^{131\mathrm{m}}$Xe is labelled 2. Black rectangles denote valves dividing the installation into separate cells. (**B**) A photograph of the experimental installation for xenon extraction and collection.

high count rates from the iodine source. The Na^{131}I source was at the distance of about 60 cm from the detectors.

After completion of the heat treatment cycles, the collection vial with xenon was detached from the experimental setup, and transported to a second γ-ray spectroscopy station, with the CANBERRA n-type XtRa Ge detector, model GX6020, for *a posteriori* precise determination of activity, without the ^{131}I background (see Figure 3.7). The sources of ^{152}Eu and ^{133}Ba with known absolute activities were used for the energy calibration and for the determination of the absolute detection efficiency at energies $E_\gamma < 1.5$ MeV. These calibrated sources were measured at the source-detector distance d equal 50 cm (used for γ-ray spectroscopy of $^{131\mathrm{m}}$Xe collection vial) and 154 cm (used for γ-ray spectroscopy of high-activity Na^{131}I powder). See Figure 3.5 for the absolute efficiency plotted in function of the energy for $d = 50\,cm$.

The coefficient of determination R^2 for the fitted 3rd degree polynomial was 0.996. The absolute efficiency curve in Figure 3.5 presents a well-known knee around 100 keV. This effect was accounted for by fitting to the dataset that included 4 γ rays in the 40–130 keV energy range. The accuracy determined as $a(E) = \left|\frac{\varepsilon_{exp}(E) - \varepsilon_{calc}(E)}{\varepsilon_{exp}(E)}\right| \cdot 100$ was calculated for the energy range near γ radiation characteristic for $^{131\mathrm{m}}$Xe (163.9 keV) and ^{131}I (364.5 keV). That accuracy for selected ^{152}Eu and ^{133}Ba γ-ray peaks equaled $a(81.0) = 0.39\%$, $a(121.8) = 0.78\%$, $a(244.7) = 0.38\%$, and $a(356.0) = 1.09\%$. It confirmed good accuracy of the fit in the energy region characteristic for γ-radiation from ^{131}I and $^{131\mathrm{m}}$Xe decay. The absolute efficiencies for 163.9 keV from $^{131\mathrm{m}}$Xe and for 364.5 keV ^{131}I were listed in Table 3.1.

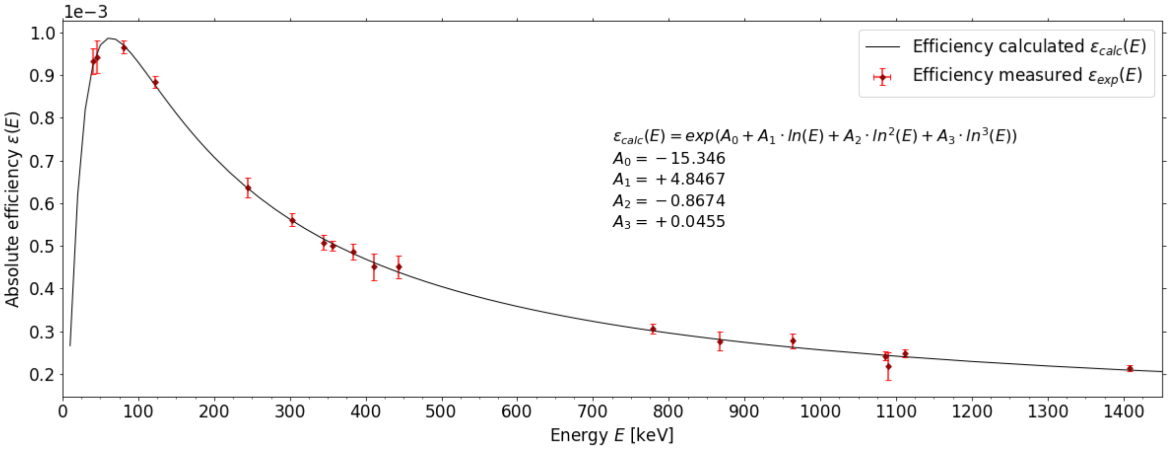

Figure 3.5: Absolute efficiency for n-type Extended Range Coaxial Ge detector (XtRa), model GX6020 at the distance of 50 cm from the source. Measured efficiency $\varepsilon_{exp(E)}$ (in red) was plotted based on ^{152}Eu and ^{133}Ba measurements. A polynomial of 3rd degree $\varepsilon_{calc(E)}$ (in black) was fitted to the experimental data. The equation and fit parameters are enclosed in Figure.

Table 3.1: Absolute efficiencies for 163.9 keV and 364.5 keV (CANBERRA XtRa detector, model GX6020).

Source	**Distance d: source – detector [cm]**	**Energy [keV]**	**Detection efficiency**
$^{131\mathrm{m}}$Xe vial	50	163.9	7.79(15)E-4
		364.5	4.98(12)E-4
Na^{131}I powder	154	364.5	5.65(13)E-5

In activity calculations, transmission through glass and air were taken into account. Attenuation of 364.5 keV γ-ray in the Na^{131}I powder was neglected due to the high porosity of the powder and inhomogeneous spread of ^{131}I onto NaI matrix (from the drop casting technique used for bulk ^{131}I solution). This attenuation coefficient was determined to be, at most 2% given the NaI grain size of 0.4 mm radius (path of X-ray).

3.3 Results

3.3.1 Efficiency of $^{131\mathrm{m}}$Xe Generator

Three types of γ-ray spectroscopy measurements (see Section 3.2) were taken and used for the calculations shown in Table 3.2: activity of the Na^{131}I capsule, activity of the Na^{131}I powder transferred to the vial, and activity of the collected $^{131\mathrm{m}}$Xe. Analyzed spectra consisted of background counts and counts in the area of interest. To derive the activity of samples, the number of counts in the peak areas was calculated using ORTEC-MAESTRO Multichannel Analyzer [107]. Linear background subtraction and Gaussian fitting were applied in regions of interest (ROIs).

A typical spectrum is shown in Figure 3.6 for the transferred ^{131}I powder and in Figure 3.7 for the collected $^{131\mathrm{m}}$Xe. In Figure 3.6, the main γ-ray transitions for ^{131}I are marked and labelled: 364.5 keV (branching ratio 81.5%), 637.0 keV (7.16%), 284.3 keV (6.12%), 80.2 keV (2.6%), and 722.9 keV (1.8%) [72]. The γ-ray decay branch—at 364.5 keV—was used for the determination of the ^{131}I activity. The sample was also verified for presence of impurities (mostly ^{133}I and ^{135}I), and no impurities were found. The γ-ray lines of the background in Figure 3.6 belong to the natural background gamma-radiation (starred in the spectrum: ^{137}Cs (661.66 keV), ^{208}Tl (277.4 keV, 510.8 keV, 583.2 keV), ^{212}Bi (727.3 keV), ^{212}Pb (238.6 keV, 300.1 keV), ^{214}Bi (609.3 keV, 665.5 keV), ^{214}Pb (74.8 keV, 77.1 keV, 242.0 keV, 295.2 keV, 351.9 keV), ^{228}Ac (209.3 keV, 270.2 keV, 327.5 keV, 328.0 keV, 338.3 keV, 463.0 keV, 509.0 keV, 726.9 keV), electron–positron annihilation peak at 511 keV), mainly due to concrete in any building and due to minerals' concentration in a geographical location [108].

For $^{131\mathrm{m}}$Xe activity determination in the spectrum of the collection vial, the γ-ray transition of 163.9 keV (1.95% branching) was used. The transition to the ground state proceeds mostly via emission of conversion electrons (29.8 keV (29.3%), 29.5 keV (15.8%), 33.6–34.5 keV (10.5%), 33.6–33.9 keV (8.5%)) [72]. The measurement for Figure 3.7 was taken in a low-background environment, free of ^{131}I source. This low background baseline allowed for the precise determination of the radionuclidic purity of $^{131\mathrm{m}}$Xe (see Table 3.3).

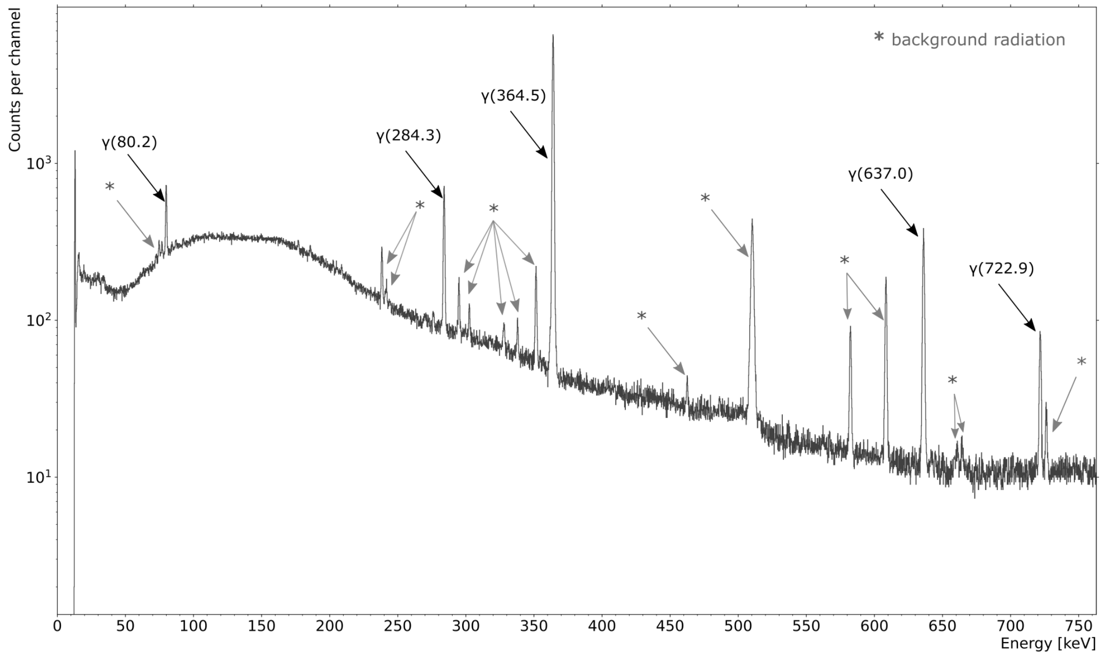

Figure 3.6: γ-ray spectroscopy of the ^{131}I powder after the transfer into the annealing vial, recorded in the ISOLDE experimental hall. The γ radiation characteristic of ^{131}I are labelled in black. These are lines at: 364.5 keV (81.5%), 637.0 keV (7.16%), 284.3 keV (6.12%), 80.2 keV (2.6%), and 722.9 keV (1.8%). The γ radiation of the background [108] is marked with grey stars in the plot.

Table 3.2 summarizes the results of experiments with three batches of Na^{131}I and collected $^{131\mathrm{m}}$Xe. Row 2 is the measured activity of Na^{131}I capsule in MBq upon delivery of the sample to

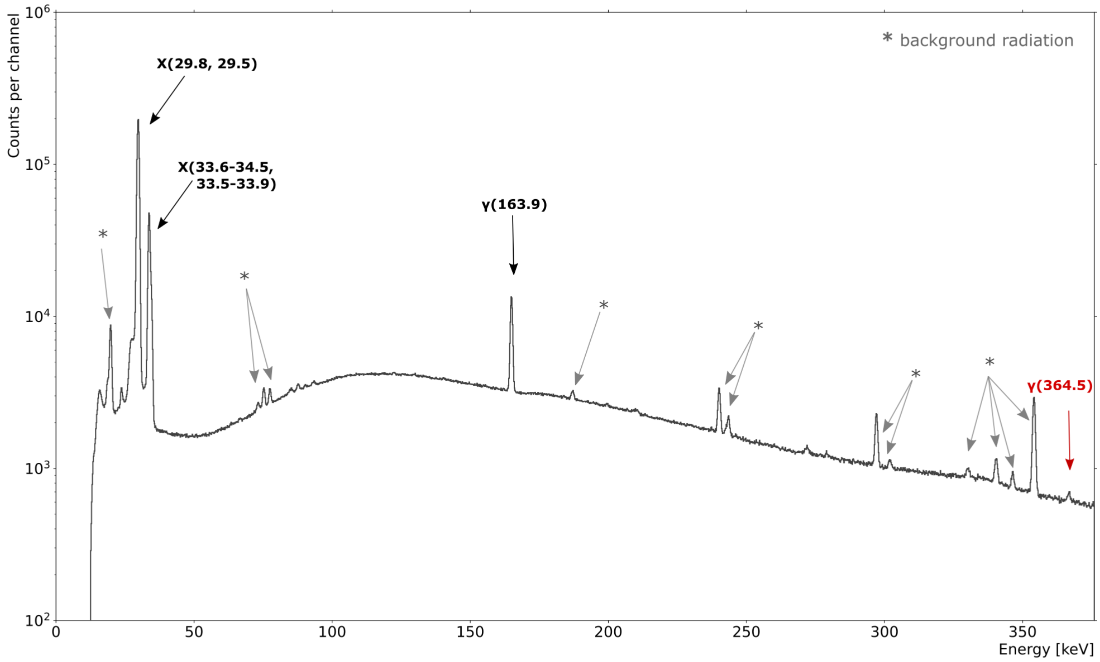

Figure 3.7: γ-ray spectrum of the collected $^{131\mathrm{m}}$Xe sample, recorded in the ISOLDE experimental hall. The decay radiation characteristic of $^{131\mathrm{m}}$Xe is labelled in black. The γ-ray transition is at 163.9 keV (1.95%). The X-rays are at: 29.8 keV (29.3%), 29.5 keV (15.8%), 33.6-34.5 keV (10.5%), 33.6-33.9 keV (8.5%). The main γ-ray peak of ^{131}I decay (364.5 keV) is labelled and marked in red. The γ radiation of the background [108] is marked with grey stars.

CERN-ISOLDE. The value for each experiment is in line with the ordered activity (50(5) MBq). Row 3 is the time between the end of manufacturing (EOM) of the Na^{131}I capsule, reported by Curium Pharma, and the γ-ray spectroscopy of Na^{131}I capsule at CERN-ISOLDE. It allowed us to determine the initial activity of Na^{131}I in the capsule, and the production of $^{131\mathrm{m}}$Xe prior to placing the powder in the experimental setup. Row 4 (transfer rate ρ) is the percentage of delivered ^{131}I activity that got transferred to the annealing tube. It was calculated based on two γ-ray spectroscopy measurements: of the ^{131}I capsule, and of the transferred ^{131}I powder. The value of ρ varies, as it depends on the Na^{131}I saturation of the NaI powder and gelatin shell with the ^{131}I bulk solution during the capsule's preparation process. For instance, for experiment ID 1, a significant percentage of ^{131}I (about 36%) was in the gelatin shell, which was cast aside.

Rows 5–7 relate to $^{131\mathrm{m}}$Xe activity. Row 5 details the activity of $^{131\mathrm{m}}$Xe expected at the end of collection (EOC). The value of $^{131\mathrm{m}}$Xe activity at the EOC depends on $^{131\mathrm{m}}$Xe production rate from mother nucleus ^{131}I, rate of $^{131\mathrm{m}}$Xe decay and on the losses of $^{131\mathrm{m}}$Xe due to the room-temperature diffusion out of powder in the time T between EOM and delivery (Row 3). The value in Row 5 was each time calculated in two steps using Eq.3.1. Firstly, to calculate $N_{0\mathrm{mXe}}$ – the number of $^{131\mathrm{m}}$Xe nuclei produced in Na^{131}I powder in the time window from EOM to placing in the experimental system ($N_{\mathrm{mXe}}(0) = 0$). Secondly, to calculate $^{131\mathrm{m}}$Xe activity at EOC (Row 5) using $t = 0$ as the moment of placing Na^{131}I in the experimental setup, $N_I(0) = \frac{A_I(0)}{\lambda_I}$, where $A_I(0)$ equals the value in Row 2, and $N_{\mathrm{mXe}}(0) = \rho\alpha N_{0\mathrm{mXe}}$.

α describes the room-temperature diffusion (loss) of $^{131\mathrm{m}}$Xe from Na^{131}I powder prior to placement in the experimental setup (in time T). The value α could not be measured directly, because

Table 3.2: Efficiency of $^{131\mathrm{m}}$Xe production and collection from decay of ^{131}I.

ID	1	2	3
Measured ^{131}I activity at delivery [MBq] *	49.0(5)	51.1(6)	47.5(4)
Time T between EOM and delivery [days]	6	2	22
^{131}I transfer rate ρ	64(1) %	85(2) %	96(2) %
Determined $^{131\mathrm{m}}$Xe activity at EOC (given ρ and α) [kBq]	119(4)	149(5)	240(7)
Measured $^{131\mathrm{m}}$Xe activity at EOC [kBq] *	99(2)	131(4)	204(1)
Efficiency of $^{131\mathrm{m}}$Xe collection	83(3) %	88(3) %	85(3) %

* — measured with CANBERRA n-type XtRa detector, model GX6020
EOM — end of manufacturing of ^{131}I capsule
EOC – end of collection of $^{131\mathrm{m}}$Xe
ρ — the transfer rate of ^{131}I from the capsule to the vial
α — the determined release rate of $^{131\mathrm{m}}$Xe at ambient conditions

upon delivery the saturation of powder with $^{131\mathrm{m}}$Xe was unknown (and impossible to measure *in situ*, due to high ^{131}I activity). Therefore, the value of α was determined at the end of three experiments as the one providing the best agreement between the calculated and measured activity of collected $^{131\mathrm{m}}$Xe for all 3 samples (defined by the residuals between calculated and measured values listed in Table 3.2, Rows 5 and 6). Precisely, we iterated over values of α to find a minimal value of standard deviation function applied to the dataset of efficiency values for all three experiments. The minimum of that function (and the smallest residuals) was obtained for $\alpha = 62\%$. The value $\alpha = 62\%$ was in agreement with the γ-ray spectroscopy measurement of the room-temperature $^{131\mathrm{m}}$Xe collection—the first collection prior to the series of the high-temperature extractions and successive collections. Like other *in situ* collection measurements, this γ-ray spectroscopy measurement was performed with the n-type SEGe detector, model GC7020 (CANBERRA).

Row 6 presents the measured $^{131\mathrm{m}}$Xe activity at EOC. The measurements were taken without the iodine background, and after a complete cycle of heat treatments (see Figure 3.7). Finally, Row 7 specifies the collection efficiency as a ratio between the measured $^{131\mathrm{m}}$Xe (Row 6) and the determined $^{131\mathrm{m}}$Xe activity at EOC (Row 5). The collection efficiency was 85% on average.

3.3.2 Collection Efficiency as a Function of Temperature

One of the objectives of this work was to establish the most suitable conditions to extract $^{131\mathrm{m}}$Xe from a Na^{131}I salt and, as a result, to minimize the workload and time needed to achieve an optimized collection. For this purpose, the collection efficiency as a function of the heating temperature was studied. ^{131}I was heated up to 400 °C in several steps. The measurements of sample no. 1 were done in a more conservative range of temperatures (up to 300 °C) than for the consecutive samples (up to 400 °C).

Samples 1 and 2 were heated multiple times to temperatures between 40 °C and 100 °C over a course of 14 days. For sample 3, the experiment's protocol was improved and all collections were executed successively on day 14 with each temperature threshold reached only once. Since the setup was not evacuated in between collections, we were not concerned with the loss of xenon outside the measurement system (parameter α) during the experiment.

Figure 3.8 presents — for each Na^{131}I sample and as a function of the extraction temperature (x-axis)— the cumulative percentages of Xe-131m extracted up until a given temperature T with respect to the total collected activity of $^{131\mathrm{m}}$Xe (y-axis). For samples 1 and 2, the value at each point in the plot is the sum of the multiple activity increments (with the activity value adapted using the decay law) contributing to the collection up to a given temperature, divided by the measured end-product $^{131\mathrm{m}}$Xe activity and expressed as a percentage. For sample 3, it is the cumulative activity of $^{131\mathrm{m}}$Xe obtained from single collections up to a given temperature, divided by the end-product measured $^{131\mathrm{m}}$Xe activity and expressed as a percentage.

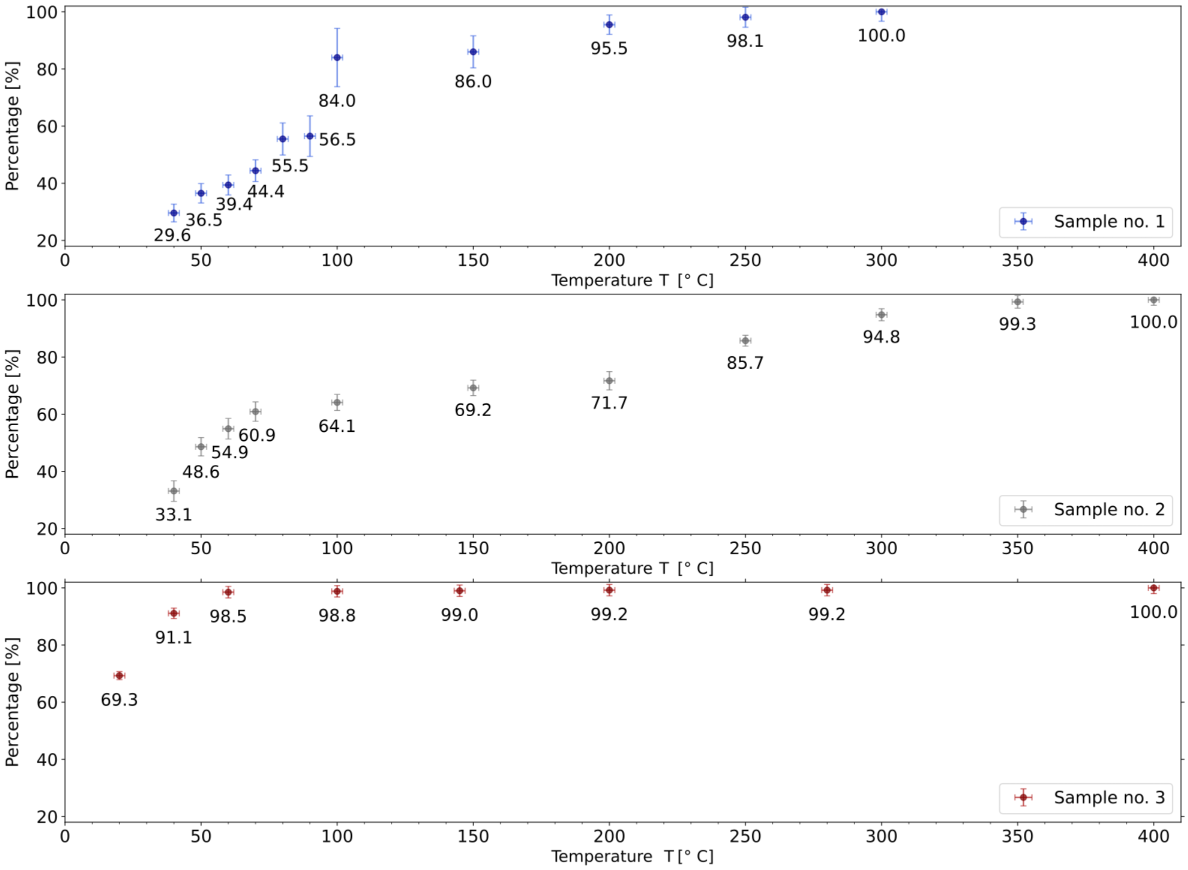

Figure 3.8: Percentage of $^{131\mathrm{m}}$Xe activity collected up until temperature T normalized to the total collected $^{131\mathrm{m}}$Xe activity.

For practical reasons, the sample was not replaced between heating cycles at different temperatures. Therefore, the thermal diffusion coefficient could not be derived. However, the collected data allowed to establish that the temperature threshold for $^{131\mathrm{m}}$Xe diffusion out of Na^{131}I powder is below or at room temperature. For heat treatments up to 100 °C: 84%, 64%, and 99% of all collected $^{131\mathrm{m}}$Xe was measured for samples 1–3, respectively. In addition, in the first collection—at room temperature—for sample 3, 69% of total collected $^{131\mathrm{m}}$Xe activity was measured. Consequently, for a time-saving $^{131\mathrm{m}}$Xe collection operation with relatively minimal losses it would be sufficient to heat the Na^{131}I sample to 200 °C.

3.3.3 Radionuclidic Purity of Generated $^{131\mathrm{m}}$Xe

Before utilizing the collected $^{131\mathrm{m}}$Xe it has to be assured that the potential residues of ^{131}I, i.e. the "breakthrough" of this sublimation generator, remains below an acceptable value. Internal exposure to ^{131}I comprises of the uptake of ^{131}I by thyroid gland and an increased risk of thyroid disease, including thyroid cancer [109].

A useful quantity to characterise the possible ^{131}I contamination of $^{131\mathrm{m}}$Xe sample is the minimum detectable activity (MDA), here expressed in Bq, at a specified confidence level. It is usually calculated at the 95% confidence level, which means there's a 95% certainty that the activity above MDA threshold would be detected. Calculations of MDA are based on Currie's derivation for single measurements [110]. With 95% level of confidence, the simplified formula for 364.5 keV emission from ^{131}I reads as follows [111]:

$$MDA = \frac{k_1^2 + 2\sqrt{2}k_1\,\sigma}{t \cdot d_{eff} \cdot y} \;, \tag{3.3}$$

where k_1 is the one-sided confidence factor at 95% confidence ($k_1 = 1.645$), t is the time of acquisition, σ is the standard deviation of the background collected at time t, d_{eff} is the detection efficiency for the γ-ray peak at 364.5 keV, and y is the γ-ray intensity per decay for the γ-ray peak at 364.5 keV.

Table 3.3 presents, for each of the 3 experiments (Column 1: ID): MDA of ^{131}I (Column 2), the ^{131}I activity determined from the area under the peak at 364.5 keV (Column 3), the detected presence or absence of radiation from ^{131}I in the spectrum (Column 4) based on the comparison of Columns 2 and 3, and the ratio of ^{131}I residual activity to $^{131\mathrm{m}}$Xe activity, expressed in % (Column 5).

As shown in Table 3.3, for all experiments the counts in the peak area at 364.5 keV were above the MDA limit. Thus, with 95% confidence, ^{131}I was present in $^{131\mathrm{m}}$Xe sample and equal 186(50) Bq, 37(13) Bq and 56(9) Bq, for ID 1, 2 and, 3 respectively. The ratio of ^{131}I activity to $^{131\mathrm{m}}$Xe activity for three experiments was: 0.19%, 0.03%, and 0.03%. The elevated ratio for the first experiment might come from the residual activity of iodine that remained in the setup from earlier preparatory experiments.

Table 3.3: Minimum detectable activity of ^{131}I in the $^{131\mathrm{m}}$Xe collection sample.

ID	**MDA [Bq]**	**Determined ^{131}I activity [Bq]**	**Radiation from ^{131}I**	**Ratio ^{131}I : $^{131\mathrm{m}}$Xe**
1	28.6	186(50)	Present	0.2%
2	4.1	37(13)	Present	0.03%
3	7.4	56(9)	Present	0.03%

With respect to chemical purity of the collection, some of the stable excipients initially present in Na^{131}I sample would decompose in the high temperature and would be introduced to the collection vial with the end product. These comprise oxides of carbon (0.8 mmol), phosphorus (0.6 mmol), and sulphur (0.15 mmol). The quantities of stable excipients present after thermal decomposition were determined analytically based on the list—provided by Curium Pharma [105]—of ingredients of the supplied source.

3.4 Discussion

The purpose of this research was to study the generation of the long-lived excited state $^{131\mathrm{m}}$Xe by thermal sublimation, from the decay of a commercially obtained ^{131}I solid-state source.

γ-ray spectroscopy showed that with consecutive heat treatments between 40 °C and 400 °C, up to 88% of the determined produced $^{131\mathrm{m}}$Xe can be routinely collected. The remaining $^{131\mathrm{m}}$Xe is possibly trapped in the Na^{131}I powder, which starts to sinter at $\approx$ 200 °C. This hypothesis could not be verified with γ-ray spectroscopy because of the high background from the Na^{131}I. In addition, up to 69% of the total $^{131\mathrm{m}}$Xe can already be collected at room temperature.

The presented sublimation generator represents a possible way to obtain low activity batches of $^{131\mathrm{m}}$Xe with high radionuclidic purity throughout the year, piggybacking on the well-established distribution network of ^{131}I capsules. The analysis of radionuclidic purity in Subsection 3.3.3 shows that in the end-product vial with $^{131\mathrm{m}}$Xe, the ratio of ^{131}I residual activity to collected $^{131\mathrm{m}}$Xe activity was 0.03% for two samples and 0.19% for one sample—from the first experiment that was possibly contaminated by the earlier preparatory experiments. The generally accepted activity range employed for the inhalation of another xenon gas agent —^{133}Xe— by an average patient (70 kg) is 74–1110 MBq for the pulmonary function imaging and 370–1110 MBq for cerebral blood flow imagining [112–114]. Tolerable residual level of ^{131}I present in the gas cylinder with ^{133}Xe radiopharmaceutical is 0.01% of total activity present in the sample [112–114], thus the maximum value would be 111 kBq. The necessary $^{131\mathrm{m}}$Xe activity in GAMMA-MRI project is: 50–100 MBq and 10–30 MBq, respectively for the polarization optimization and for proof-of-principle experiments in a preclinical MRI device built within the GAMMA-MRI project [115]. Given the experimentally derived ratio ^{131}I to $^{131\mathrm{m}}$Xe equal to 0.03% (see Table 3.3), the residual activity of ^{131}I would be at maximum 30 kBq for the polarization optimization and 9 kBq for proof-of-principle experiments in a preclinical MRI device. In the scope of next experiments taking place in Switzerland, an additional consideration is to follow the authorization limits (LA) listed in the Swiss Radiological Protection Ordinance [116], which are: 9 GBq for $^{131\mathrm{m}}$Xe and 0.5 MBq for ^{131}I.

However, despite high radionuclidic purity, some of the stable excipients added to samples are present in the collection vial with the end product (Subsection 3.3.3). Thus, purification methods of the end product might have to be implemented prior to deployment for the GAMMA-MRI project. A practical limitation is that collection of $^{131\mathrm{m}}$Xe would have to be planned 13–15 days in advance of a subsequent experiment to allow for ^{131}I decay and production of sufficient amounts of $^{131\mathrm{m}}$Xe. Thus, an experimental setup needs to be dedicated solely to this goal for a whole period of approximately two weeks.

Finally, several fundamental limitations of the detailed method have to be kept in mind that *de facto* preclude a significant upscaling of this method. First, the maximum recovered activity of $^{131\mathrm{m}}$Xe is about 300 times smaller than the ^{131}I activity of the generator, even assuming lossless transfer of Na^{131}I powder to the experimental setup. Further, one has to consider that the ^{131}I mother has fivefold higher γ-ray dose rate per Bq than the $^{131\mathrm{m}}$Xe daughter, and several orders of magnitude higher radiotoxicity per Bq than $^{131\mathrm{m}}$Xe. Consequently, upscaling this method to large-scale generators without process automation is undesirable from ALARA considerations, and could run into licensing issues.

3.5 Conclusions and Outlook

An affordable and accessible production method of small activities of the long-lived ^{131m}Xe isomer via radioactive decay of commercially available ^{131}I was investigated. Our thermal sublimation generator is dedicated to supplying the long-lived ^{131m}Xe for optimization tests of laser polarization in the GAMMA-MRI project. Once larger activity batches of ^{131m}Xe are required for a regular clinical use, the preferred option would be a centralized production in dedicated facilities with centralized quality control. ^{131m}Xe can also be produced by thermal neutron capture on enriched ^{130}Xe samples and the activities and radionuclidic purity achievable in reactor irradiations will be discussed in a forthcoming article.

Author contributions. Conceptualization: R.B.J., M.K., U.K., K.K.; methodology: K.K.; software: K.K., R.L., S.G.P.; validation: M.K., U.K., K.K., R.L., S.G.P.; formal analysis: K.K., R.L., S.G.P.; investigation: M.J.C., K.K., R.L., S.G.P.; resources: N.A., M.B., M.K., K.K., R.L., S.G.P.; data curation: K.K., R.L., S.G.P.; writing—original draft preparation: K.K.; writing—review and editing: R.B.J., M.K., U.K., K.K., R.L., S.G.P.; visualization: K.K.; supervision: R.B.J., M.K.; project administration: R.B.J., M.K.; funding acquisition: R.B.J., M.K. All authors have read and agreed to the published version of the manuscript.

Funding. The GAMMA-MRI project has received funding from the European Union's Horizon 2020 research and innovation programme under grant agreement No. 964644 (GAMMA-MRI). The authors also wish to acknowledge support via the Swiss Excellence Government Scholarship, the CERN Medical Application Fund (GAMMA-MRI), and the Romanian IFA grant CERN/ISOLDE.

Institutional Review Board Statement. Not applicable.

Informed Consent Statement. Not applicable.

Data Availability Statement. Data supporting the reported results can be found at: https://cernbox.cern.ch/index.php/s/Eo9CTu5LOo5bx8O. Accessed on 20 September 2022. The detailed study is available on request from the corresponding author.

Acknowledgements. We thank B. Karg, S. Warren, and members of SY-STI-RBS, in particular B. Crepieux, E. Barbero, J. Ballof, and S. Rothe, for discussions, assistance in designing the initial prototype and manufactured parts of the setup, M. Wuillemin for his input on iodine production, J.A. Ferreira Somoza for discussion on Xe cryogenic trapping, J. Schell for assistance in scheduling the experiments. We thank A. Dorsival, E. Aubert, P. Bertreix, N. Menaa, A.L. Boscher, and other members of HSE-RP for their support during project execution.

Conflicts of interest. The authors declare no conflict of interest.

Chapter 4

Production of ^{129m}Xe and ^{131m}Xe via neutron activation of ^{128}Xe and ^{130}Xe at the ILL-RHF and NCJB-MARIA high-flux reactors

Mateusz Chojnacki (contributed equally) [1,2], Karolina Kulesz (contributed equally) [1,2], Ilaria Michelon [1,3], Nikolay Azaryan [4], Bernard Crepieux [1], Agnieszka Korgul [5], Razvan Lica [1,6], Łukasz Murawski [7], Monika Piersa-Siłkowska [1], Renaud Blaise Jolivet [8], Rafal Prokopowicz [7], Ulli Köster [9], Magdalena Kowalska [1,2]

Submitted to Applied Radiation and Isotopes, September 2023.

Abstract

The long-lived xenon isomers $^{129\mathrm{m}}$Xe and $^{131\mathrm{m}}$Xe are of interest for the GAMMA-MRI project, which aims at developing a novel imaging modality based on magnetic resonance of polarised unstable tracers. Here, we present the steps leading to and following the production of these two isomers via neutron irradiation of highly-enriched ^{128}Xe and ^{130}Xe gas samples at two high-flux reactors, the High-Flux Reactor (*Réacteur à haut flux*, RHF) at the Institut Laue-Langevin (ILL) and the MARIA reactor at the National Centre for Nuclear Research (NCBJ). We describe the experimental setups and procedures used to prepare the stable xenon samples, to open the irradiated samples, and to transfer xenon isomers into reusable transport vials. The activity of $^{129\mathrm{m}}$Xe and $^{131\mathrm{m}}$Xe was measured to be in the range of tens of MBq per sample of 0.8(1) mg, and was proportional to thermal neutron flux density. A small activity of unstable contaminants was also visible in the samples, but their level is not limiting for the GAMMA-MRI project's objectives. In addition, the minimum thermal neutron flux density required to produce $^{129\mathrm{m}}$Xe and $^{131\mathrm{m}}$Xe sufficient for the project could be also determined.

---

[1] CERN, Espl. des Particules 1, 1211 Meyrin, Switzerland
[2] Faculty of Science, University of Geneva, Quai Ernest-Ansermet 24, 1211 Geneva, Switzerland
[3] University of Padova, Via 8 Febbraio 2, 35122 Padova, Italy
[4] Adam Mickiewicz University, ul. Uniwersytetu Poznanskiego 2, 61-614 Poznan, Poland
[5] University of Warsaw, Krakowskie Przedmiescie 26/28, 00-927, Warsaw, Poland
[6] Horia Hulubei National Institute of Physics and Nuclear Engineering (IFIN-HH), Reactorului 30 St., 077125 Bucharest-Magurele, Romania
[7] National Center for Nuclear Research (NCBJ), Andrzeja Sołtana 7, 05-400, Otwock-Swierk, Poland
[8] Maastricht Centre for Systems Biology (MaCSBio), Maastricht University, Paul-Henri Spaaklaan 1, 6229 EN Maastricht, The Netherlands
[9] Institut Laue-Langevin (ILL), 71 Avenue des Martyrs, 38000 Grenoble, France

4.1 Introduction

Neutron activation in nuclear reactors is a well-known approach to large-scale production of long-lived isotopes for medical diagnostics and treatment. The best-known examples of such isotopes are ^{99m}Tc for Single Photon Emission Computed Tomography (SPECT) imaging, ^{131}I for thyroid cancer treatment, and ^{177}Lu for treatment of various types of cancer [117]. However, nuclear reactors can be also used for small-scale production of new isotopes for basic research or pre-clinical studies. Here, we present the production of two such isotopes, long-lived $^{129\mathrm{m}}$Xe ($T_{1/2} = 8.88$ days) and $^{131\mathrm{m}}$Xe ($T_{1/2} = 11.84$ days) isomers, using neutron activation of enriched ^{128}Xe and ^{130}Xe at two high-flux reactors, with pre- and post-irradiation handling at the ISOLDE facility at CERN. This study is part of the GAMMA-MRI project [118], whose aim is to develop a new imaging technique based on magnetic resonance imaging (MRI) using polarized unstable tracers [115].

4.2 Experimental setups and procedures

The production of $^{129\mathrm{m}}$Xe and $^{131\mathrm{m}}$Xe isomers (further referred to as mXe) at the High-Flux Reactor (RHF) at the Institute Laue-Langevin [119], and at the MARIA reactor at the National Centre for Nuclear Research [120] and their preparation for further use for the GAMMA-MRI project consisted of several steps spread over several weeks. (a) First, the highly enriched stable ^{128}Xe or ^{130}Xe gases were closed and flame-sealed in quartz vials at CERN. (b) The vials with stable xenon were activated with neutrons for 3–13 days at the RHF or MARIA reactor. A few days after the end of irradiation the activated samples were shipped back to CERN, where: (c) the vials were cleaned from external contamination; (d) γ-ray spectroscopy measurement was performed on the vials; (e) the vials were opened and xenon was transferred to a reusable leak-tight transport vial; (f) γ-ray spectroscopy was performed on the transport vial. In this way, 2–5 days after reception, mXe samples were ready for the next steps in the GAMMA-MRI project. In the following, we detail the essential steps and experimental setups.

4.2.1 Preparation of stable xenon samples for activation

In the first step, highly-enriched ^{128}Xe or ^{130}Xe was closed in quartz vials that were flame-sealed by a glass blower. Both, the enrichment and the use of quartz aimed at minimizing the activity of isotopes different than mXe of interest. The molar content of other Xe isotopes and other gases in the containers with stable Xe was below 0.1%, as shown in Tables 4.1 and 4.2.

Table 4.1: Relative molar concentration (in %) of Xe isotopes in natural and enriched ^{128,130}Xe samples used in irradiations (according to supplier: Isoflex, San Francisco, USA, https://isoflex.com).

Xe sample	^{124}Xe	^{126}Xe	^{128}Xe	^{129}Xe	^{130}Xe	^{131}Xe	^{132}Xe	^{134}Xe	^{136}Xe
Xe natural abundance	0.1	0.1	1.9	26.4	4.1	21.2	26.9	10.4	8.9
enriched ^{128}Xe	0.001	0.010	99.931	0.052	0.001	0.001	0.002	0.001	0.001
enriched ^{130}Xe	0.003	0.003	0.003	0.023	99.947	0.012	0.003	0.003	0.003

Table 4.2: Relative molar concentration (in %) of other gases in enriched ^{128,130}Xe samples used in irradiations (according to supplier: Isoflex, San Francisco, USA, https://isoflex.com).

Xe sample	CO+N_2	CO_2	Ar	CH_4	H_2O	O_2	Kr	C_7H_8
enriched ^{128}Xe	0.004	0.008	<0.002	<0.001	<0.001	0.002	<0.004	<0.002
enriched ^{130}Xe	0.003	0.011	<0.006	<0.001	<0.009	<0.005	<0.006	<0.005

The Xe samples were prepared for irradiation using a vacuum-tight gas setup (able to reach $1 \cdot 10^{-5}$ mbar pressure on the pump side, equivalent to $1 \cdot 10^{-3}$ mbar on the Xe bottle side) shown in Figure 4.1. The system is made of stainless steel tubing and metal seals (Swagelok, OH, USA) to connect different elements, which guarantees low leak rates and small inner volume, and thus leads to small losses of enriched xenon in 'dead' volumes or outside the system.

The Xe filling procedure in the referenced system included the following steps: (a) Two quartz vials (labeled 4. in Figure 4.1, 120 mm in length and closed at one end) were attached via Swagelok-type glass-metal teflon seal to needle valves and through these to the filling setup. (b) All valves in the setup (except the gas-bottle valve) were opened and the whole setup was pumped down with a turbomolecular pump for 48 h. At this point, the pressure measured next to valve number (3.) was $1 \cdot 10^{-5}$ mbar, i.e. about $1 \cdot 10^{-3}$ mbar between the Xe cylinder and the recovery loop (measured offline). (c) The system was purged several times with argon gas at 1000 mbar pressure. (d) The valve to the vacuum pumps (3.) was closed, and (e) the valve at the gas cylinder (1.) was opened to introduce Xe until the gauge 2 (5.) showed 300 mbar (the readout of this gauge was independent of the gas type), and thus the whole setup was filled with ^{128}Xe or ^{130}Xe to that pressure. (f) The needle valves above the quartz vials (4.) were closed to trap inside the vials the quantity of the enriched xenon required for the irradiation. (g) The u-shaped tubing (2.) was placed in a liquid nitrogen bath (LN_2). The remaining Xe was collected in this 'recovery loop', since Xe condenses below 165 K. (h) The valve between the recovery loop (2.) and the quartz vials (4.) was closed and the LN_2 trap was removed. (i) The quartz vials with enclosed stable Xe were detached from the setup (j) and sealed with a glass-blowing torch, creating a pair of two 50-mm-long quartz ampoules with about 0.5(1) cm^3 of highly enriched ^{128}Xe or ^{130}Xe at 300 mbar inside (Figure 4.2). Finally, xenon trapped in the volume of the u-shape could be used to fill the next two vials, once steps (a) to (i) (except bottle opening at step (e)) were repeated.

After the vials were sealed, the created ampoules were individually cleaned in an ultrasonic bath using consecutively nitric acid, water, and ethyl alcohol. Additionally, ampoules were tested for leaks and fractures by submerging them in water and by heating them in a furnace. The pressure at which Xe was enclosed was chosen to avoid over-pressurization of the ampoules in the reactor core. The external dimensions of the ampoules, on the other hand, were driven by the size of an enclosure in which the ampoules were placed for the irradiations. Finally, the pressure of stable Xe inside the ampoules of 300(10) mbar and their volume of 0.5(1) cm^3 corresponded to 0.8(1) mg or 6.1(8) μmol of Xe inside one ampoule.

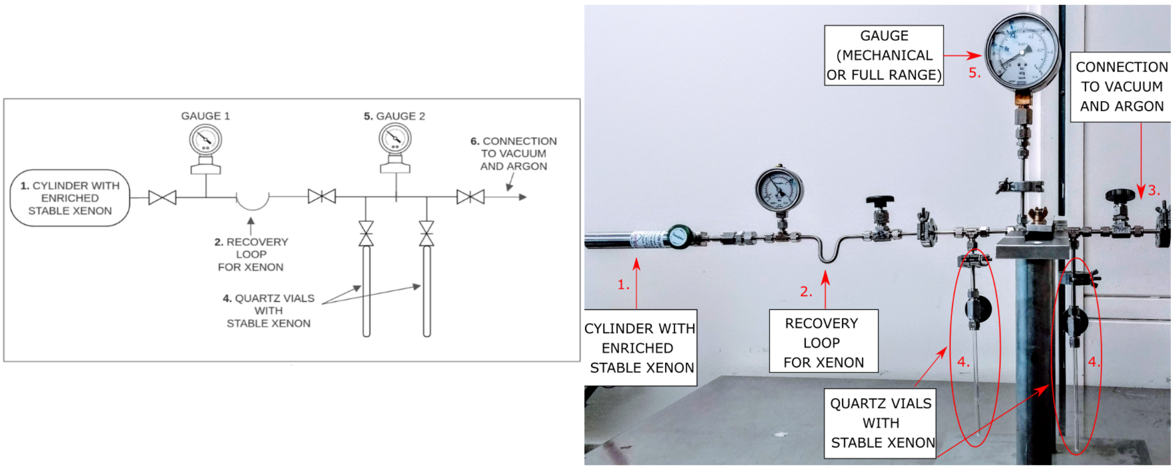

Figure 4.1: A schematic drawing (left) and an image (right) of the vacuum-tight gas system used to fill vials with stable xenon. The valves divide the setup into separate volumes.

4.2.2 Neutron activation at high-flux reactors

The xenon ampoules were irradiated at two high-flux European reactors, RHF and MARIA, both of which are used for fundamental studies, nuclear physics investigations, as well as production of ’standard’ and new medical isotopes.

The High-Flux Reactor (RHF) at the Institute Laue-Langevin (ILL) located in Grenoble, France, is one of the most intense sources of thermal neutrons [119]. To reach thermal conditions (E_{th}=25 meV, $v_{th} = 2200\,\mathrm{ms^{-1}}$), the energy spectrum of fission neutrons is moderated by heavy water, D_2O, which is also used as a reactor coolant and neutron reflector [121]. At RHF, the stable xenon samples were irradiated at several positions with the most intense neutron flux density in the reactor, namely $0.7 - 1.1 \cdot 10^{15}\,\mathrm{cm^{-2}s^{-1}}$.

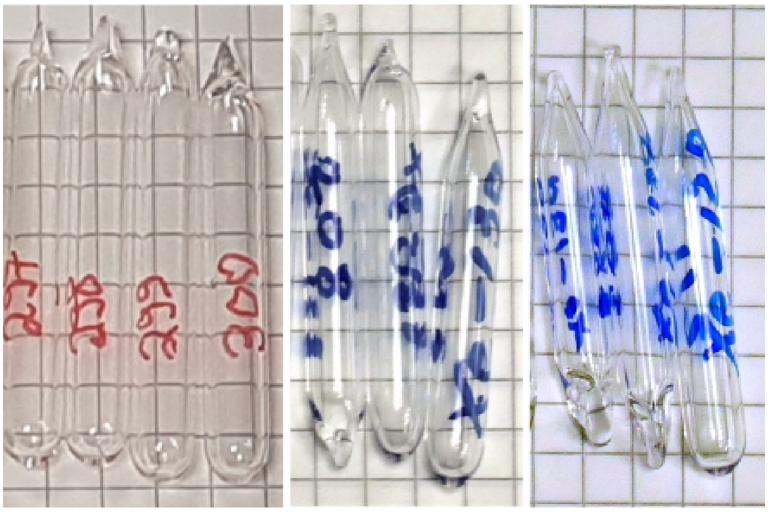

Figure 4.2: Several sets of flame-sealed quartz ampoules containing enriched stable xenon. Their outer diameter was 6 mm, inner diameter was 4 mm, while their length was around 50 mm (the spacing between background lines was 5 mm).

The high-flux reactor MARIA [120] is located at the National Centre for Nuclear Research (NCBJ) in Świerk, Poland. MARIA reactor neutron spectrum is moderated by beryllium blocks and light water, H_2O, that is also used as a reactor coolant [121]. This configuration gives $0.5 - 2.4 \cdot 10^{14}\,\mathrm{cm}^{-2}\mathrm{s}^{-1}$ thermal-neutron flux density, which was used to irradiate our Xe samples.

The procedures and irradiation times were similar at both reactors. After reception, the stable xenon ampoules were closed inside aluminium capsule, and placed at the irradiation position, where they were irradiated. At the end of the irradiation cycle the capsules were retrieved from the irradiation point and opened. The mXe ampoules were removed from the capsules and shipped to CERN-ISOLDE Class A laboratories. A Posisafe KL-30 type "A" package (Lemer Pax Inc., France) was used, which is a tungsten-shielded hermetic container for the secure transport of all radioactive substances, including gases.

Given the relative molar concentration of enriched xenon (^{128,130}Xe, see Table 4.1) that is above 99.9%, cross section database [122] and based on the neutron spectrum for both reactors [119, 120], the following nuclear reactions: ^{128}Xe(n,γ)$^{129\mathrm{m}}$Xe or ^{130}Xe(n,γ)$^{131\mathrm{m}}$Xe, should dominate the samples activation. Their cross-sections for thermal neutron energy are presented in Table 4.3. In addition, other reactions occurring with the nuclei present in the vials with stable xenon or with the nuclei produced during the irradiation should be taken into account as a source of radioactive (Xe radioactive isotopes: ^{125,127,133,135,137}Xe, Xe isomers: $^{125\mathrm{m},127\mathrm{m},133\mathrm{m},135\mathrm{m}}$Xe, ^{125,126}I) and stable contaminants (Xe stable isotopes: $^{124,126,128-132,134,136}$Xe) in activated samples. These potential reactions with the corresponding cross-sections are listed in Table 4.3.

Table 4.3: Average cross sections of thermal-neutron reactions on isotopes present or produced in irradiated samples with enriched ^{128,130}Xe [122].

Reaction	$T_{1/2}$	Cross section (b)	Reaction	$T_{1/2}$	Cross section (b)
^{128}Xe(n,γ)$^{129\mathrm{m}}$Xe	8.88 d	0.48(10)	^{128}Xe(n,γ)^{129}Xe	stable	3.0(7)
^{130}Xe(n,γ)$^{131\mathrm{m}}$Xe	11.84 d	0.45(10)	^{130}Xe(n,γ)^{131}Xe	stable	3.1(7)
^{124}Xe(n,γ)$^{125\mathrm{m}}$Xe	57 s	28(5)	^{124}Xe(n,γ)^{125}Xe	16.9 h	122(21)
^{125}Xe(n,γ)^{126}Xe	stable	<5600	^{126}Xe(n,γ)$^{127\mathrm{m}}$Xe	69.2 s	0.25(13)
^{126}Xe(n,γ)^{127}Xe	36.4 d	2.2(3)	^{129}Xe(n,γ)^{130}Xe	stable	21(3)
^{131}Xe(n,γ)^{132}Xe	stable	93(9)	^{132}Xe(n,γ)$^{133\mathrm{m}}$Xe	2.2 d	0.005(1)
^{132}Xe(n,γ)^{133}Xe	5.2 d	0.40(6)	^{133}Xe(n,γ)^{134}Xe	stable	190(90)
^{134}Xe(n,γ)$^{135\mathrm{m}}$Xe	9.1 h	0.003(1)	^{134}Xe(n,γ)$^{135\mathrm{m}}$Xe	15.6 min	0.003(1)
^{134}Xe(n,γ)^{135}Xe	9.14 h	0.26(3)	^{135}Xe(n,γ)^{136}Xe	stable	2.65(11)
^{136}Xe(n,γ)^{137}Xe	3.8 min	0.26(2)			

4.2.3 Cleaning and opening of quartz ampoules, and collection of Xe isomers in transport vials

Upon arrival at CERN, activated ampoules were cleaned from contaminants introduced during handling in the reactor hot cells. The cleaning allowed recording of low-background γ-ray spectra of the gases inside the vials, avoiding further contamination, and facilitating radioactive waste management. A standard procedure of decontamination was used: the ampoules were rinsed four times in an ultrasonic bath using sequentially the following solvents: nitric acid 67% solution, demineralized water, ethanol 99% solution, and again demineralized water.

Next, γ-ray spectra were recorded with a calibrated High-Purity Germanium (HPGe) P-type extended range detector (model GX6020 by CANBERRA, Montigny-Le-Bretonneux, France), with a thin carbon window [123] for each cleaned ampoule in order to establish the produced activity of $^{129\mathrm{m}}$Xe or $^{131\mathrm{m}}$Xe, as well as of other possible unstable contaminants. Finally, the gases inside every quartz ampoule were transferred into a reusable stainless-steel transport vial. For this purpose, the ampoules were crushed and the released Xe isotopes were collected in the transport vial immersed in a LN$_2$ bath. Other produced isotopes, such as iodine and cesium are solid at room temperature and thus remained in the opening setup.

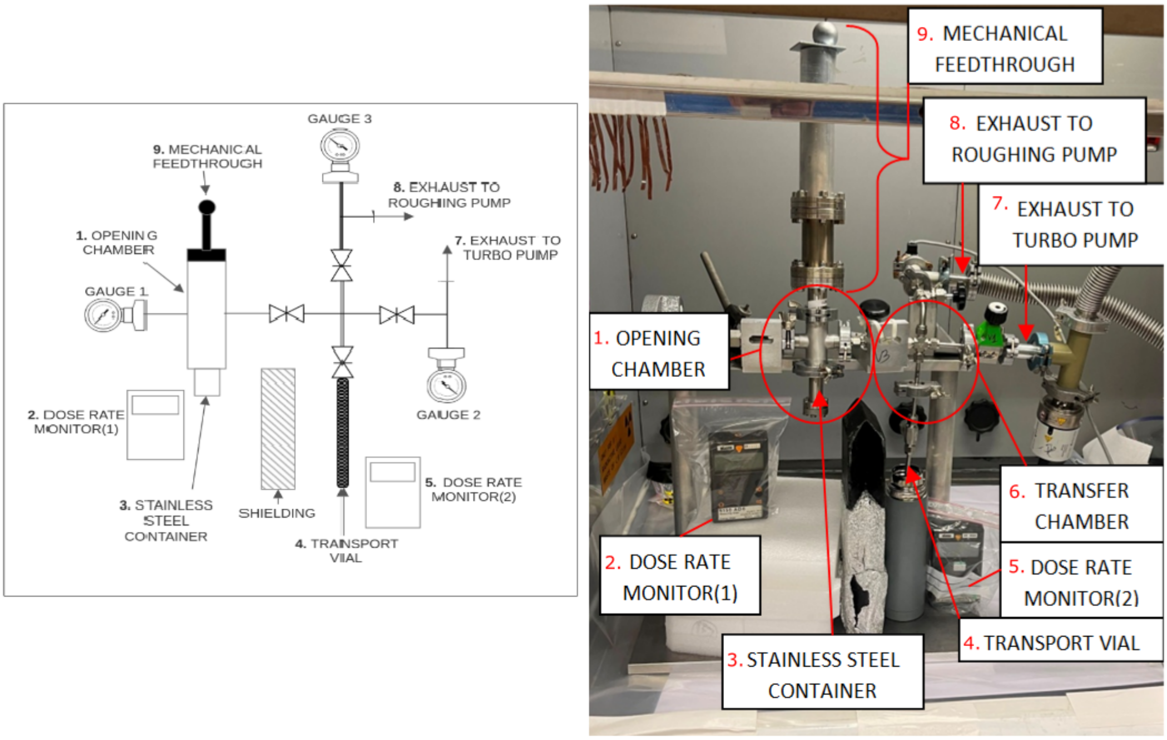

Figure 4.3: Schematic drawing (left) and photograph (right) of the setup used for opening quartz ampoules.

To avoid contaminating the samples with gaseous air components (N$_2$, O$_2$, etc.) the opening was carried out using a dedicated vacuum setup (Figure 4.3) at low pressure ($5 \cdot 10^{-6}$ mbar, measured with gauge G2). After the vacuum valves between the setup and the pumps were closed (8.), the quartz ampoule was crushed by pushing down onto it with the tip of a mechanical feedthrough (9.). The fact that the quartz ampoule got opened was indicated by a drop in the dose rate measured on the dose monitor 1 (2.). This meant that Xe isomers spread inside the opening chamber. Next, a reusable stainless-steel transport vial equipped with a valve (4.) was cooled in a LN$_2$ trap for 5 minutes to perform an efficient xenon transfer from (1.) and collection in (4.). The collection was performed until the dose rate shown by the dose rate monitor 2 (5.) was close to that observed originally at the dose rate monitor 1 (2.) and did not change further. At that point, the needle valve on the transport vial was closed. Next, the rest of the system was pumped and the transport vial was detached from the setup.

After the opening procedure, the filled transport vials were moved to the γ-ray spectroscopy station for activity measurements of the trapped gases. Based on those measurements and the measurements performed earlier on the decontaminated quartz ampoules, a collection efficiency (ϵ_{col}) was established for each sample.

4.3 Results

4.3.1 Cross sections for $^{129\mathrm{m}}$Xe and $^{131\mathrm{m}}$Xe production

The γ-ray spectroscopy measurements performed on decontaminated quartz tubes showed activities above 40 MBq per sample for $^{129\mathrm{m}}$Xe and $^{131\mathrm{m}}$Xe produced in both reactors. These activities exceeded the requirement of the GAMMA-MRI project for the minimum total activity of 10 MBq measured 10 days after the end of irradiation (EOI) [115]. Figures 4.4 and 4.5 show the experimental results from a dozen ampoules irradiated at RHF and MARIA reactors. The measured activities are determined for the end of irradiation and normalized to the number of moles of stable xenon ($\mathrm{MBq} \cdot \mu\mathrm{mol}^{-1}$). The activity uncertainties include vial volume uncertainty (10%) of the enclosed stable xenon gas, as well as a smaller contribution from the uncertainty of gamma spectroscopy measurement. The neutron flux densities are extracted from calculations made in Monte Carlo N-Particle Transport Code (MCNP) with uncertainty based on the fluctuation of the reactor exploitation parameters (about 10-15%).

Figure 4.4 shows experimental data for $^{129\mathrm{m}}$Xe (blue dots with error bars). Based on measured activities and linear activation law [124], the cross-section for radiative neutron capture reaction on ^{128}Xe in a Maxwellian thermal neutron flux was fitted (solid orange line with orange uncertainty area), $\sigma_\gamma(^{128}$Xe)=0.29(1) b. Fitted cross-section is 40% lower than the recommended literature value [122]. Finally, considering neutron capture on $^{129\mathrm{m}}$Xe, the simultaneous contributions of neutron captures on ^{128}Xe and $^{129\mathrm{m}}$Xe ("destroying" $^{129\mathrm{m}}$Xe) [125] were fitted. This approach gave unchanged value for $\sigma_\gamma(^{128}$Xe) with respect to the linear activation law and allowed to set an upper limit for radiative cross-section on $^{129\mathrm{m}}$Xe, $\sigma_\gamma(^{129\mathrm{m}}$Xe) $<$150 b (dotted green line).

Data for ^{131m}Xe, presented in Figure 4.5, shows a good agreement between molar activities at the end of irradiation expected from literature cross-section value (dashed red line with pink uncertainty area) [122] and experimental data (blue dots with error bars). Fitted experimental cross-section for radiative neutron capture on ^{130}Xe in Maxwellian thermal flux (solid orange line) is $\sigma_\gamma(^{130}$Xe)=0.41(2) b. Taking into account radiative cross-section on $^{131\mathrm{m}}$Xe [125] gives the similar result for radiative neutron capture on stable ^{130}Xe and allows to estimate the upper limit for radiative cross-section on $^{131\mathrm{m}}$Xe, $\sigma_\gamma(^{131\mathrm{m}}$Xe) $<$200 b (dotted green line).

4.3.2 Radionuclide purity

The γ-ray spectroscopy measurements allowed also to determine the radionuclide purity of $^{129\mathrm{m}}$Xe and $^{131\mathrm{m}}$Xe samples, expressed as a percentage of the radioactivity of the desired radionuclide to the total radioactivity of the source. Radionuclide purity is important for isotopes that are planned to be used in medical applications as the present impurities may increase the effective dose rate received

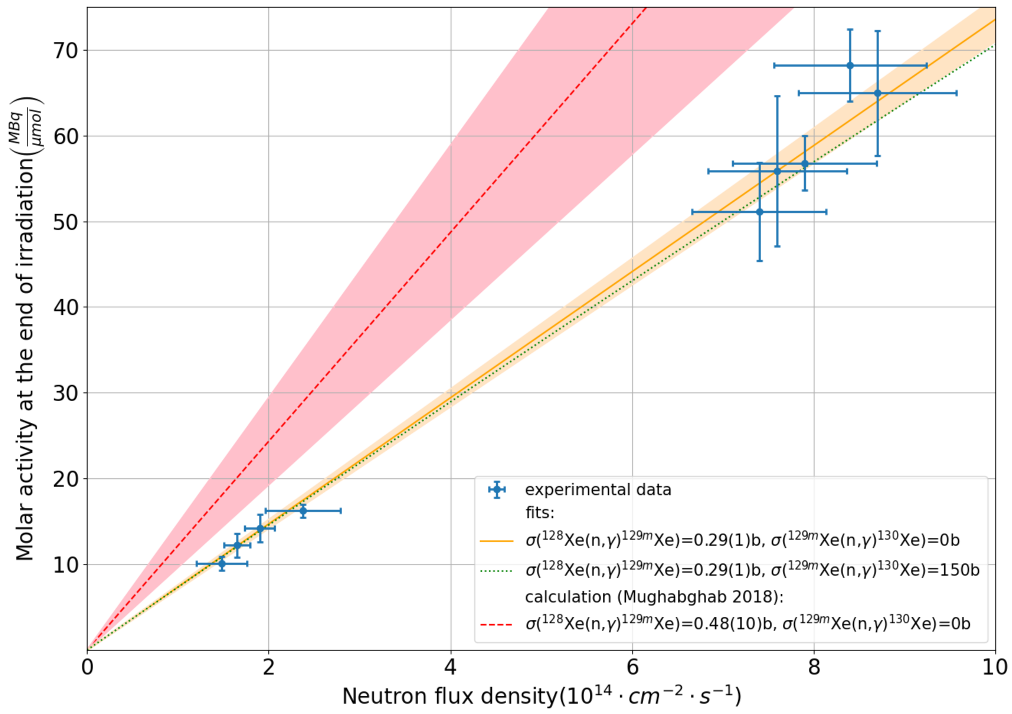

Figure 4.4: $^{129\mathrm{m}}$Xe production rates (molar activities at the end of irradiation) for samples irradiated in different neutron flux densities in the RHF and MARIA reactors (blue points with uncertainties - see text for details about uncertainties). Fitted cross-section for radiative neutron capture reactions on ^{128}Xe (solid orange curve) with uncertainty range (orange area). Fitted upper limits for radiative neutron capture reaction on $^{129\mathrm{m}}$Xe (dotted green curve). Calculated activities (dashed red curve) with uncertainty range (pink area) based on Mughabghab 2018 [122].

by the patient, thus degrading the quality of any imaging procedure performed [126]. The limits set for $^{129\mathrm{m}}$Xe and $^{131\mathrm{m}}$Xe samples are presented in Table 4.4.

Table 4.4: Radionuclide purity, expressed in percent [%], of $^{129\mathrm{m}}$Xe and $^{131\mathrm{m}}$Xe samples produced in high-flux nuclear reactors, 5 days and 10 days after the end of irradiation (EOI). Isotopes other than Xe (e.g I and Cs) remained in the glass ampoules so were no visible in transport vials. Values with a star (*) were estimated based on Minimum Detectable Activity (MDA) calculated for given isotope otherwise the activity has been measured.

date	sample	$^{129\mathrm{m}}$Xe	$^{131\mathrm{m}}$Xe	^{125}Xe	^{127}Xe	^{133}Xe	$^{133\mathrm{m}}$Xe	^{135}Xe
EOI+5 days	$^{129\mathrm{m}}$Xe	>99.72	<0.21*	<0.005	<0.03	<0.01*	<0.02*	<6E-04*
EOI+10 days	$^{129\mathrm{m}}$Xe	>99.72	<0.23*	<5E-05	<0.04	<0.008*	<0.006*	<1E-07*
EOI+5 days	$^{131\mathrm{m}}$Xe	<0.05*	>99.91	<0.005*	<0.004*	<0.007*	<0.02*	<0.005*
EOI+10 days	$^{131\mathrm{m}}$Xe	<0.05*	>99.94	<5E-05*	<0.004*	<0.005*	<0.006*	<7E-08*

4.3.3 Xenon collection efficiency

The main parameter that can characterize the setup used to open the irradiated ampoules and to enclose xenon in reusable metallic transport vials (Figure 4.3), is the xenon collection efficiency (ϵ_{col}).

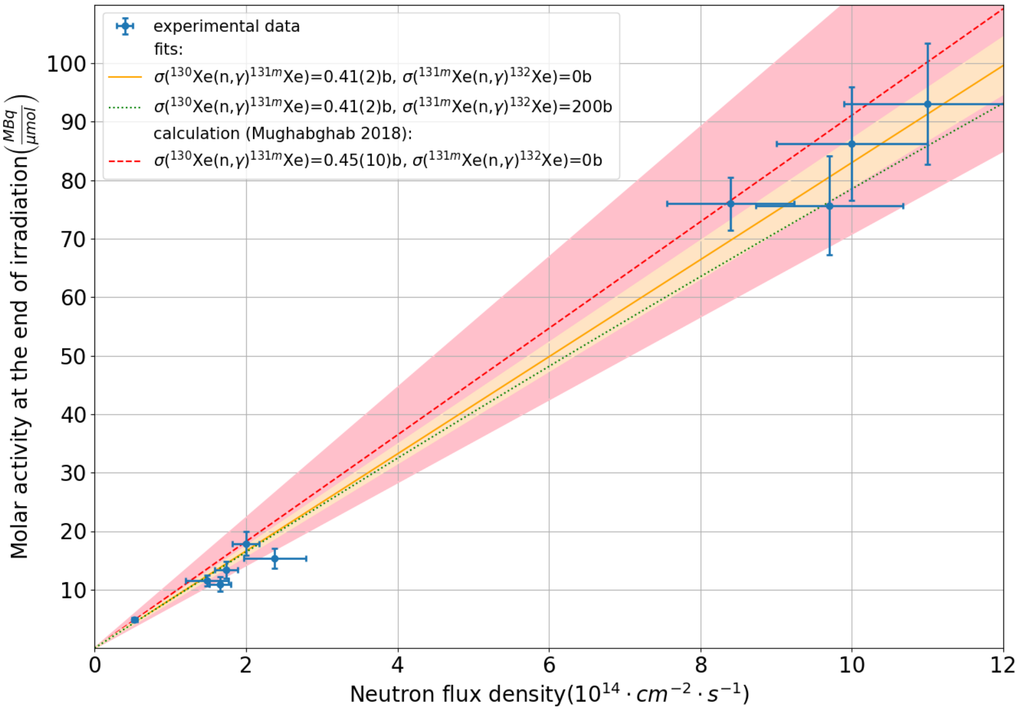

Figure 4.5: $^{131\text{m}}$Xe production rates (molar activities at the end of irradiation) for samples irradiated in different neutron flux densities in the RHF and MARIA reactors (blue points with uncertainties - see text for details about uncertainties). Fitted cross-section for radiative neutron capture reactions on ^{130}Xe (solid orange curve) with uncertainty range (orange area). Fitted upper limits for radiative neutron capture reaction on $^{131\text{m}}$Xe (dotted green curve). Calculated activities (dashed red curve) with uncertainty range (pink area) based on Mughabghab 2018 [122].

The parameter ϵ_{col} was determined based on γ-ray spectroscopy measurements performed on sealed quartz ampoules with activated mXe and then on corresponding transport vials with transferred xenon. For that, it is required to have a good estimation of γ-ray efficiency of the relevant γ-ray lines of $^{129\text{m}}$Xe and $^{131\text{m}}$Xe for both geometries (i.e. quartz ampoules and metal container). Our estimates are based on the Nucleonica package, followed by a more precise determination using Geant4 simulations. The value of ϵ_{col} is relevant for the GAMMA-MRI project since its high value allows to maintain a high level of mXe activity received from the reactors to make it available for further use within the project. Based on a dozen collections, the average value of ϵ_{col} was around 75(4)%.

4.3.4 Minimum thermal neutron flux density requirements

Based on GAMMA-MRI project requirements (mentioned in Subsection 4.3.1) the minimum Xe isomers activity required for the project is 10 MBq (A_{min}) 10 days after the end of irradiation (t_d). Following this requirement and neutron activation principles, the minimum required thermal neutron

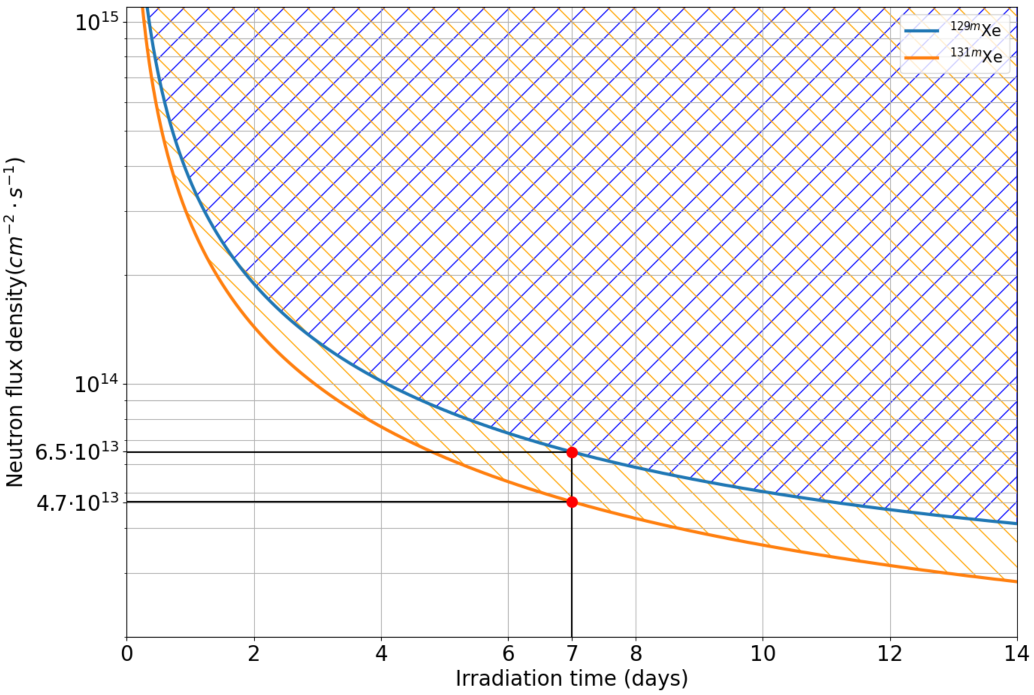

Figure 4.6: Minimum thermal neutron flux density in function of continuous irradiation time necessary to reach the GAMMA-MRI objective of 10 MBq of Xe isomer in the transport container 10 days after end of irradiation: flux requirement for $^{129\mathrm{m}}$Xe (blue dashed are) and $^{131\mathrm{m}}$Xe (orange dashed area). As an example flux requirement for 7 days irradiation for $^{129\mathrm{m}}$Xe (red point on the blue curve) and $^{131\mathrm{m}}$Xe (red point on the orange curve).

flux density (ϕ_{th}) for continuous irradiation is described by the equation [124]:

$$\phi_{th} \geq \frac{A_{min}}{\epsilon_{col} \cdot \sigma_{\gamma,i} \cdot n \cdot N_A \cdot (1 - exp(-\lambda_j \cdot t_{irr})) \cdot exp(-\lambda_j \cdot t_d)},$$

where $\sigma_{\gamma,i}$ — cross section for radiative neutron capture reaction on isotope i (^{128}Xe or ^{130}Xe) obtained from experimental data (Subsection 4.3.1), n – number of moles of isotope i present in irradiated sample, N$_A$ — Avogadro number, t$_{irr}$ — irradiation time, λ_j — decay constant of produced isomer j ($^{129\mathrm{m}}$Xe or $^{131\mathrm{m}}$Xe), ϵ_{col} — Xe collection efficiency (Subsection 4.3.3). The graphical representation of minimum thermal neutron flux density required for GAMMA-MRI project, calculated for 6.1 μmol (average irradiated quantity of stable xenon - Subsection 4.2.1), is presented in Figure 4.6.

4.4 Conclusions and outlook

In the above manuscript, we have described the experimental setups and procedures (Subsection 4.2.1) which allowed to obtain samples of $^{129\mathrm{m}}$Xe and $^{131\mathrm{m}}$Xe for the GAMMA-MRI project via irradiation of enriched ^{128}Xe and ^{130}Xe at high-flux reactors (Subsections 4.2.2 and 4.2.3). The setups use commercial vacuum elements and Swagelok-type tube connectors, which allow achieving 10^{-5} mbar pressure on the side of the vacuum pumps and 10^{-3} mbar on the other extreme (see Figures 4.1

and 4.3). Liquid nitrogen traps were used to collect stable and unstable xenon gases in the desired volumes.

We have also shown the production rates, i.e. activities normalised to the number of moles of stable xenon inside samples at the end of irradiation, for ^{129m}Xe and ^{131m}Xe. These results allowed to calculate cross-section for radiative neutron capture on ^{128}Xe (0.29(1) b) and ^{130}Xe (0.41(2) b). Additionally, upper limits for cross sections for radiative neutron capture on ^{129m}Xe ($<$150 b) and ^{131m}Xe ($<$200 b) were established (Subsection 4.3.1).

The radionuclide purity of ^{129m}Xe and ^{131m}Xe produced in nuclear reactor have been defined (Subsection 4.3.2, Table 4.4). Furthermore, the minimum thermal neutron density required to produce intense ^{129m}Xe and ^{131m}Xe samples for the future of GAMMA-MRI project have been established (Subsection 4.3.4, Figure 4.6).

An efficient production method of ^{129m}Xe and ^{131m}Xe in high-flux neutron reactors was established for the GAMMA-MRI project. This approach already provides high-activity and relatively high-purity samples of mXe. To characterize the samples in more detail and to maximize the available activity, the next steps in the project are analysis of sample composition before irradiation, longer γ-ray measurement for irradiated ampoules, upgrading the experimental setups allowing to reach better vacuum and higher efficiency of xenon transfer. Also, thermal neutron cross-section studies should be performed to better understand the sources of unstable contaminants and the ways to minimize them. These studies can allow the prediction of the composition of ^{129m,131m}Xe samples at different reactor facilities and, subsequently, the irradiation optimization.

Acknowledgements

This project received funding from the Swiss Excellence Government Scholarship (to KK), the CERN Medical Application Fund (gamma-MRI; to RBJ and MK), the European Union's Horizon 2020 research and innovation programme under grant agreement No 964644 (GAMMA-MRI). AK and RP, ŁM, MZ acknowledge funding from the Polish Ministry of Education and Science. RL acknowledges the Romanian IFA grant CERN/ISOLDE and Nucleu project No. PN 23 21 01 02.

Chapter 5

A numerical study of the anisotropic distribution of γ-ray emission from oriented ^{129m,131m,133m}Xe

Karolina Kulesz [1,2], Robin Yoël Engel [1,3], Renaud Blaise Jolivet [4], Magdalena Kowalska [1]

Submitted to the *Measurement Science and Technology* IOP journal, May 2023.

Abstract

Spin-polarized radioactive nuclei emit radioactive decay products in an anisotropic manner that is characteristic of their degree of nuclear orientation. This property can be utilized for nuclear magnetic resonance spectroscopy and imaging. In this manuscript, we present Python and MATLAB numerical simulations that investigate the angular distribution and measurable asymmetry of γ-ray emission from spin-oriented nuclei of the metastable isotopes $^{129\mathrm{m},131\mathrm{m},133\mathrm{m}}$Xe. We examine several cases that represent different degrees of spin alignment and detection geometries. The results of our simulations provide a benchmark for experiments that use γ-decay anisotropy, such as the GAMMA-MRI project, which aims to develop a novel medical-imaging technique combining the strengths of magnetic resonance and nuclear medicine imaging.

5.1 Introduction

Over the past few decades, several authors have presented detailed discussions on the topic of nuclear spin orientation [1] and the resulting angular correlations and angular distribution of nuclear radiation [128–133]. Some of these studies were specifically focused on γ-emitting nuclei. In nuclear-structure research, γ-emitting nuclei were utilized to determine the spins and parities of excited states in nuclei [128, 129], or to measure magnetic moments of unstable nuclei through γ-detected nuclear magnetic resonance (gamma-NMR) [134, 135]. More recently, γ-ray-detected magnetic resonance imaging (gamma-MRI) has even been proposed as a potential medical diagnostic application [136], which is now the focus of the European GAMMA-MRI project, as described at https://gamma-mri.eu.

The GAMMA-MRI project aims to combine the principles of nuclear spin manipulation used in Magnetic Resonance Imaging (MRI), with the highly efficient detection of γ-rays used in Single Photon

---

[1] CERN, Espl. des Particules 1, Meyrin, 1211, Switzerland
[2] University of Geneva, Quai Ernest-Ansermet 24, Geneva, 1205, Switzerland
[3] Carl von Ossietzky Universität Oldenburg, Ammerländer Heerstr. 114-118, 26129 Oldenburg, Germany
[4] Maastricht Centre for Systems Biology (MaCSBio), Maastricht University, Paul-Henri Spaaklaan 1, Maastricht, 6229 EN, Netherlands

[1] Note that we use the term 'orientation' as the most general form of uneven distribution of spin population, encompassing polarization (or vector polarization) and alignment (tensor polarization) [127]. In other communities the terms are interchanged, namely polarization is more general than orientation and alignment.

Emission Tomography (SPECT). Specifically, the project relies on: (1) external spin orientation of unstable γ-emitting nuclei inside a magnetic field; (2) measurement of the asymmetry in the angular distribution of the emitted γ radiation, which depends on the degree of orientation; and (3) application of MRI sequences to manipulate the spins in a selected volume of space and thus to modify the angular distribution of radiation for image reconstruction [137].

Here, we present analytical calculations and numerical simulations of the anisotropic distribution of γ-rays emitted by metastable xenon isotopes $^{129\mathrm{m},131\mathrm{m},133\mathrm{m}}$Xe, which are feasible candidates for the GAMMA-MRI technique. The calculations are based on the additional assumption that the spin orientation can be described by the so-called *spin temperature*. Our results aim to support the optimization of spin orientation and detector asymmetry in the GAMMA-MRI project.

Conventional MRI works by manipulating the net magnetization of protons, i.e. the population difference between the spin-up and spin-down levels. The Boltzmann distribution predicts that in the static magnetic field of a typical MRI scanner with a field strength of $\mathbf{B_0} = 1.4\,\mathrm{T}$ the relative difference in these two populations is small, on the order of 10^{-5}. Therefore, conventional MRI is heavily dependent on the abundance of hydrogen atoms in biological tissues to achieve feasible signals, and necessitates strong magnetic fields.

However, it is possible to engineer *ex-situ* a larger difference between spin populations, by means other than increasing the magnetic field. These approaches are known as hyperpolarization (HP). One such technique is Spin-Exchange Optical Pumping (SEOP), which has been extensively described for non-radioactive noble gases by Happer and Walker [50], and others [68, 138]. SEOP uses circularly-polarized light from a laser to polarize alkali atoms in a gas phase (rubidium or cesium), within a glass cell placed in a weak magnetic field (several mT). A pair of Helmholtz coils generates a homogeneous magnetic field in the cell's region, providing an orientation axis for the polarized atoms. During binary collisions and three-body interactions in the formation of Van der Waals molecules with nitrogen, the hyperfine interaction between the alkali-metal electron and the noble-gas nucleus cause them to partially exchange angular momentum. Repeated interactions lead to a build-up of nuclear spin orientation of mXe to several tens of percent. The build-up of nuclear orientation can be monitored conveniently by continuous or pulsed nuclear magnetic resonance (NMR) excitations.

In comparison to stable He and Xe, SEOP of radioactive noble gases (namely Xe) was performed only by Calaprice *et al.* [134], and much more recently by Zheng and collaborators [136]. In the above cases, the SEOP process was followed by NMR or MRI rf pulse sequences, respectively.

In the GAMMA-MRI approach, in addition to exploiting HP, one utilizes a different detection scheme compared to conventional MRI. Instead of detecting the weak electromagnetic signal induced by rotating spins using inductive pickup coils, one measures the anisotropic emission of γ-rays, as demonstrated in [134, 136]. This method offers an advantage over conventional MRI as, unlike radio-frequency (rf) photons, even individual γ-ray photons can be easily discerned and detected with high probability. In principle, this detection scheme allows reaching excellent sensitivity to small amounts of tracer nuclei in the sample volume.

The paper is organized as follows: in the following Section 5.2, we summarize the mathematical description of nuclear orientation and γ decay characteristics, and lay out the idealized measurement geometry that was used for the computations presented in the Section 5.3, and discussed in Section 5.4. Here, a number of test cases are introduced to illustrate the effect of various parameters on the detected asymmetry. Specifically, we consider the impact of polarization and alignment, the relevance of higher-order multipolar emission contributions, and differences in the experimental geometry of the sample and detector. We conclude our findings with respect to the GAMMA-MRI project in Section 5.4.

5.2 Model assumptions

5.2.1 Description of the model

In the simulations presented here, we consider the instantaneous nuclear alignment of radioactive xenon nuclei and the resulting angular distribution of the emitted γ radiation. Notably, we do not include considerations on the process of SEOP, such as the achievable degree of Rb atom polarization, the rates of spin orientation transfer from rubidium atoms to xenon nuclei, as well as losses of xenon orientation over time. This has been treated in detail elsewhere [50, 139].

Spin temperature T_s and spin temperature parameter β are useful parameters to describe an ensemble of identical interacting spins that have been brought out of thermal equilibrium and have not yet returned back to it (e.g. mXe after orientation via spin exchange optical pumping) [79]. In that case, the population p_m of the magnetic sublevels of the spins is characterized by a Boltzmann distribution [79] with $p_m \propto e^{-m/(kT_s)}$ (k is the Boltzmann constant) and therefore can be described with only one parameter T_s, analogous to a 'real' temperature for a system in thermal equilibrium. The dimensionless β which we use in the manuscript is defined as $\beta = -1/(kT_s)$.

Three isomers (i.e. long-lived excited nuclear states) are of interest for the GAMMA-MRI project: $^{129\mathrm{m}}$Xe, $^{131\mathrm{m}}$Xe, and $^{133\mathrm{m}}$Xe, to which we refer further as mXe. All three have spins $I = {}^{11}\!/_{2}$ and decay via a pure $M4$ γ-ray transition to $I = {}^{3}\!/_{2}$ state, which is either the ground state or first excited state. Their decay schemes are shown in Fig. 5.1 [71–73].

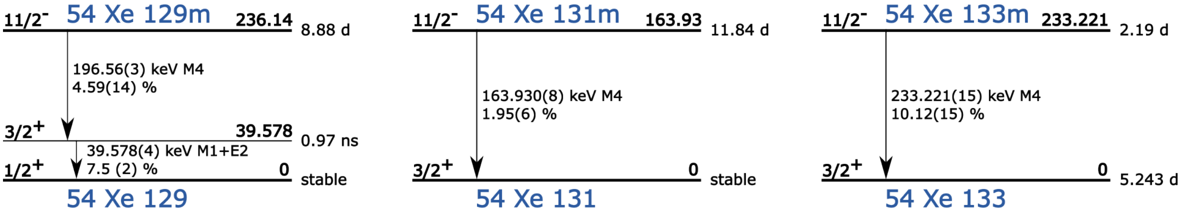

Figure 5.1: Radioactive decay schemes of the isomers $^{129\mathrm{m}}$Xe, $^{131\mathrm{m}}$Xe and $^{133\mathrm{m}}$Xe drawn using ref. [71–73].

In the following, we describe the angular distribution of γ radiation for these nuclear spins and the type of γ radiation.

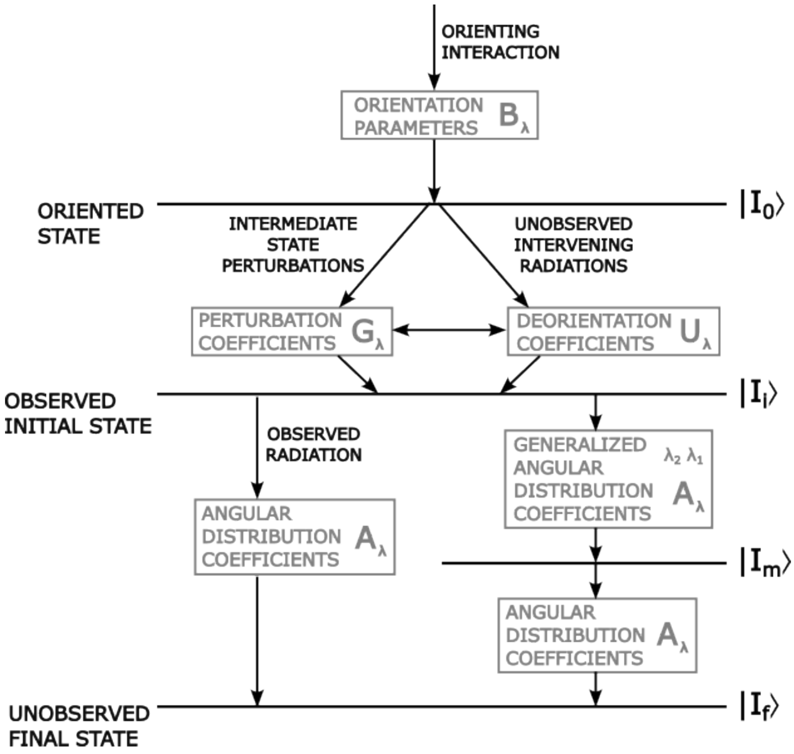

Figure 5.2: Schematic diagram showing the nuclear states and parameters involved in the parametrization of angular distribution measurements from oriented nuclei. Drawing based on ref. [128], Chapter 2: *Nuclear Orientation Formalism*.

5.2.2 Anisotropic distribution of γ radiation from oriented nuclei

In order to describe the angular distribution $W(\theta)$ for a certain type of decay radiation emitted by an ensemble of oriented nuclei (at angle θ) to the quantization axis), several coefficients have to be known. Fig. 5.2 illustrates the nature of these coefficients.

I_0 is the spin of the original oriented state, the parent state of the radioactive decay, or the initial state of a nuclear reaction. I_f is the final state, and I_m the intermediate state, for cases with two or more intermediate radiations. B_λ are the nuclear orientation parameters describing the initial oriented state. λ is connected to the type of radiation and the multipolarity L of the radiation emitted between the oriented I_0 state and the final state I_f. For example, for β emission only odd λ's are relevant, compared to even λ's for γ-ray emission. The maximum λ is given by the multipolarity L of the emitted radiation $\lambda_{max} = 2L$ (with $L = 2$ for dipole transitions, $L = 4$ for quadrupole transitions, etc). For $M4$ γ-ray transitions studied here, $L = 4$ and thus $\lambda \in \{2, 4, 6, 8\}$.

In the most general case, the $B_\lambda(I)$ are calculated using statistical tensors in the density matrix formalism [81]. In the particular case when the orienting interaction has an axis of symmetry (such as is the case in here), the diagonal elements of the density matrix are used as population parameters p_m, with $m' = m$, and the equation for $B_\lambda(I = I_0)$ simplifies to:

$$B_\lambda(I_0) = \sqrt{(2\lambda+1)(2I_0+1)} \sum_m (-1)^{I_0+m} \begin{pmatrix} I_i & \lambda & I_i \\ -m & 0 & m \end{pmatrix} p_m \,, \tag{5.1}$$

where the weights are given by the Wigner 3-j symbol.

U_λ are the orientation coefficients that depend on the properties of the intervening intermediate radiations. U_λ determine the orientation of I_i by modifying the orientation of I_0. If there is no intervening radiation, I_i is identical to I_0, and U_λ are equal to 1. This is the case for the $^{11}/_{2}$ state of metastable xenon.

G_λ are the perturbation coefficients describing the direct interaction of the electromagnetic moments of a long-lived intermediate state I_i with the nuclear environment (if such long-lived states exist). Coefficients G_λ refer to the same phenomenon as relaxation in magnetic resonance terms. In the numerical simulations, they were assumed to be 1, and thus the initial state was the same as the originally oriented state, and there were no time-varying relaxation processes. Finally, A_λ are the angular distribution coefficients that depend on the radiation type and transition multipolarity for the observed radiation. In case of multiple radiations, where it might be advantageous to measure two emissions in coincidence, we would differentiate between A_{λ_1} and A_{λ_2} (generalized angular distribution coefficients in Fig. 5.2). In our case, where we have a single transition, i.e. for $I_i \rightarrow I_f$ transition, A_λ is:

$$A_\lambda = \frac{1}{1+\sigma^2}[F_\lambda(L, L', I_f, I_i) + 2\sigma F_\lambda(L, L', I_f, I_i) + \sigma^2 F_\lambda(L, L', I_f, I_i)] \,, \tag{5.2}$$

where L and L' are the previously-mentioned angular momenta of the γ radiation and $L' = 0$, as the mixing ratio $\sigma = 0$ for the pure multipole transitions. $F_\lambda(L, L', I_f, I_i)$ are multipole functions with Wigner 3-j symbol and 6-j symbol. $F_\lambda(L, L', I_f, I_i)$ are tabulated, e.g. in [128, 140]:

$$\begin{aligned} F_\lambda(L, L', I_f, I_i) = (-1)^{I_f+I_i+1}\sqrt{(2\lambda+1)(2L+1)(2L'+1)(2I_i+1)} \\ \cdot \begin{pmatrix} L & L' & \lambda \\ 1 & -1 & 0 \end{pmatrix} \begin{Bmatrix} L & L' & \lambda \\ I_i & I_i & I_f \end{Bmatrix} \,. \end{aligned} \tag{5.3}$$

For the case studied here ($\sigma = 0$), coefficients $A_\lambda = F_\lambda(L = 4, L' = 0, I_f, I_0)$.

For the axially symmetric oriented states we discuss here, the general expression for the normalized directional distribution of γ-ray transition given in [128] (Chapter 2.6) can be simplified to a form of a multiple expansion:

$$W(\theta) = 1 + \sum_{\lambda\ even} B_\lambda\, U_\lambda\, G_\lambda\, A_\lambda\, Q_\lambda\, P_\lambda(\cos\, \theta) \tag{5.4}$$

with the solid angle correction factor Q_λ that compensates for the finite solid angles subtended by the source and the detector. If we assume that the source and the detector are each geometrical points, and thus that the direction of the radiation emission can be uniquely specified, then Q_λ = 1. Finally, $P_\lambda(\theta)$ is the Legendre polynomial of order λ, and θ is the azimuthal angle between radiation and z-axis, around which the radiation is axially symmetric. Rodrigues' formula gives a compact expression for the Legendre polynomials, namely: $P_n(x) = \frac{1}{2^n n!}\frac{d^n}{dx^n}(x^2-1)^n$.

In the simulations, we assume a negligible size for the source and detectors, and no intervening intermediate radiations for the $^{11}/_{2}$ state. Thus, we take U_{λ_j}, G_λ, and Q_λ as each equal to 1. Coefficients A_λ and B_{λ_j} are explicitly calculated and given as an output of the simulations, and so is the resulting angular distribution $W(\theta)$ plotted as a two-dimensional figure.

5.2.3 Evaluating spin orientation

Nuclear orientation can be described using $B_\lambda(I_0)$ parameters up to the maximum allowed λ, as introduced above, as well as using the notation of Tolhoek and Cox [140]. Among all parameters, the most frequently used are these with $\lambda = 1, 2$, namely the first- and second-order orientation parameters, also known as *polarization* and *alignment*, respectively.

The polarization (also known as vector polarization [127]), i.e. the first-order orientation parameter f_1, is defined as an average value of the spin projection on the selected orientation axis (usually taken to be the z-axis) I_Z, normalized with the absolute spin value I [128]:

$$f_1(I) = \frac{\langle I_Z \rangle}{I} = \sum_m \left(\frac{m}{I}\right) p_m = -B_1(I)\sqrt{\frac{I+1}{3\,I}}\;. \tag{5.5}$$

The sign of polarization changes if the direction of the spins gets inverted.

Alignment (also known as tensor polarization [127]), i.e. the second-order orientation parameter f_2, on the other hand, quantifies the deviation from the uniform spin distribution towards a distribution favoring the spin projections along the z-axis:

$$f_2(I) = \sum_m \left(\frac{m}{I}\right)^2 p_m - \frac{I+1}{3I} = B_2(I)\sqrt{\frac{(2I+3)\,(I+1)\,(2I-1)}{45\,I^3}}\;, \tag{5.6}$$

where B_2 here is the nuclear orientation parameter B_{λ_j} for $\lambda_j = 2$. Alignment is a measure of axially symmetric distribution of the spins, which means that the following is true: $p_m = p_{-m}$ (unlike for polarization where $p_m \neq p_{-m}$) [80]. Alignment is positive if the majority of spins are oriented along or against the z-axis, and negative if they are oriented perpendicular to it. The second-order parameter (as well as higher-order parameters with even values of λ) does not change in value if the direction of the nuclear spins is reversed.

The degree of polarization and alignment (i.e. f_1 and f_2) can be related to a given spin temperature β and be provided as the output of the simulation together with the asymmetry in γ-ray emission.

5.2.4 Simulation of mXe γ-decay asymmetry detection for selected spin temperatures β

In the first step of calculations outlined in previous sub-chapters, the coefficients A_λ and B_λ for mXe decay (with $I_0 = {}^{11}\!/_{2}$ and $\lambda = 2, 4, 6, 8$) were calculated for selected spin temperatures that represent an increasing degree of orientation. Next, they were used as input for MATLAB simulations of experimental γ-ray asymmetry for several detector geometries.

Figures 5.3 and 5.4 illustrate the geometry used in these simulations with three γ-ray detectors placed in two planes (blue in the x − y plane; red and green in the y − z plane), around an ensemble of γ-ray emitting xenon nuclei in a single voxel (i.e. a volume of space). The two panels represent the case of no nuclear alignment (in Fig. 5.3) and the case of perfectly aligned spins (in Fig. 5.4) along the external static magnetic field $\vec{\mathbf{B}}$ (z-axis), and thus emit γ-rays preferentially in the plane orthogonal to $\vec{\mathbf{B}}$.

The size of the detectors was set to $9\text{x}9\,\mathrm{mm}^2$, while the source was assumed to be point-like unless specified otherwise. The distance of the detectors to the source d_{sd} (set to be the same for three detectors) was a variable examined in this study, also represented as a solid angle Ω of γ-ray detection. The spherical and elliptical shapes of non-zero dimensions in Figures 5.3 and 5.4 are the 3-dimensional reconstructions of the angular distribution of γ-ray emission from the source.

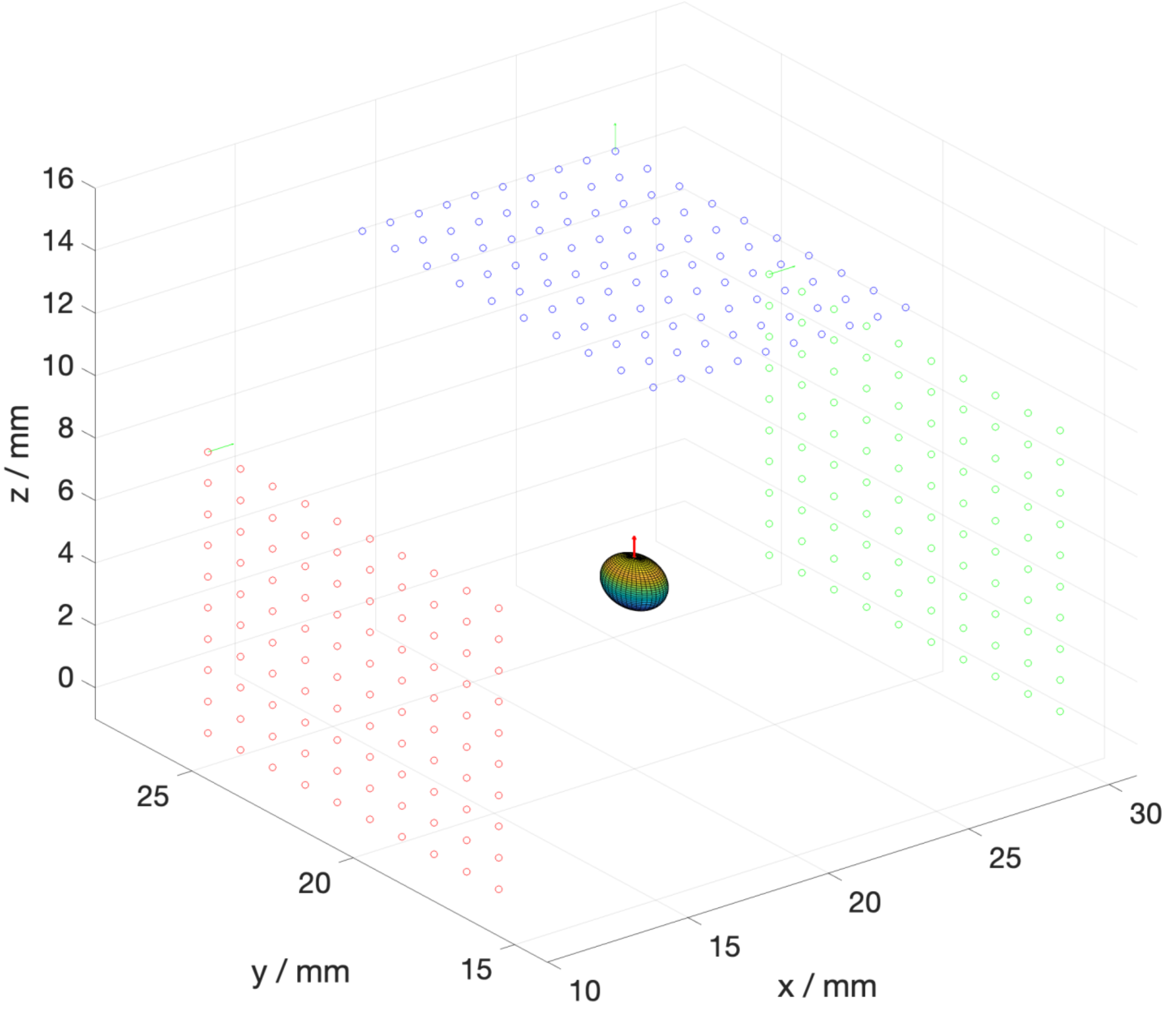

Figure 5.3: The first of two exemplary MATLAB simulation outputs of an ensemble of γ-ray emitting Xe nuclei emitted by a point-like source. Three detectors (green, blue, and red) with 10x10 sensors each are located around a sample of one voxel visualized with a red vector indicating its spin orientation and with a 3D surface plot indicating the directional distribution of emitted γ radiation. Here, γ radiation is emitted isotropically from randomly oriented nuclei (no nuclear orientation: $\beta = 0$, $f_1 = 0$, and $f_2 = 0$), which is represented as a spherical 3D surface plot.

Given an equidistant placement of the γ-ray detectors from the point-like or finite-size not oriented source, the recorded count rate should be equal for all three detectors. In the case of nuclear alignment however, the γ-ray count rate increases for a detector placed transversely to $\vec{\mathbf{B}}$, and decreases for the detector placed longitudinally to $\vec{\mathbf{B}}$.

Let us consider an example for a point-like source of 30 MBq activity: with perfect detectors of the dimensions given above and placed at 20 mm from the source, one should expect to register $7.1 \cdot 10^5$ photon counts per second (cps) in all 3 detectors, if the sample is not oriented ($\beta = 0$), as shown in Fig. 5.3. For a (near) perfectly aligned sample ($\beta = 10$, shown in Fig. 5.4), one may expect $12.9 \cdot 10^5$ cps in the detector placed transversely to $\vec{\mathbf{B}}$, and $3.7 \cdot 10^5$ cps in the detector placed

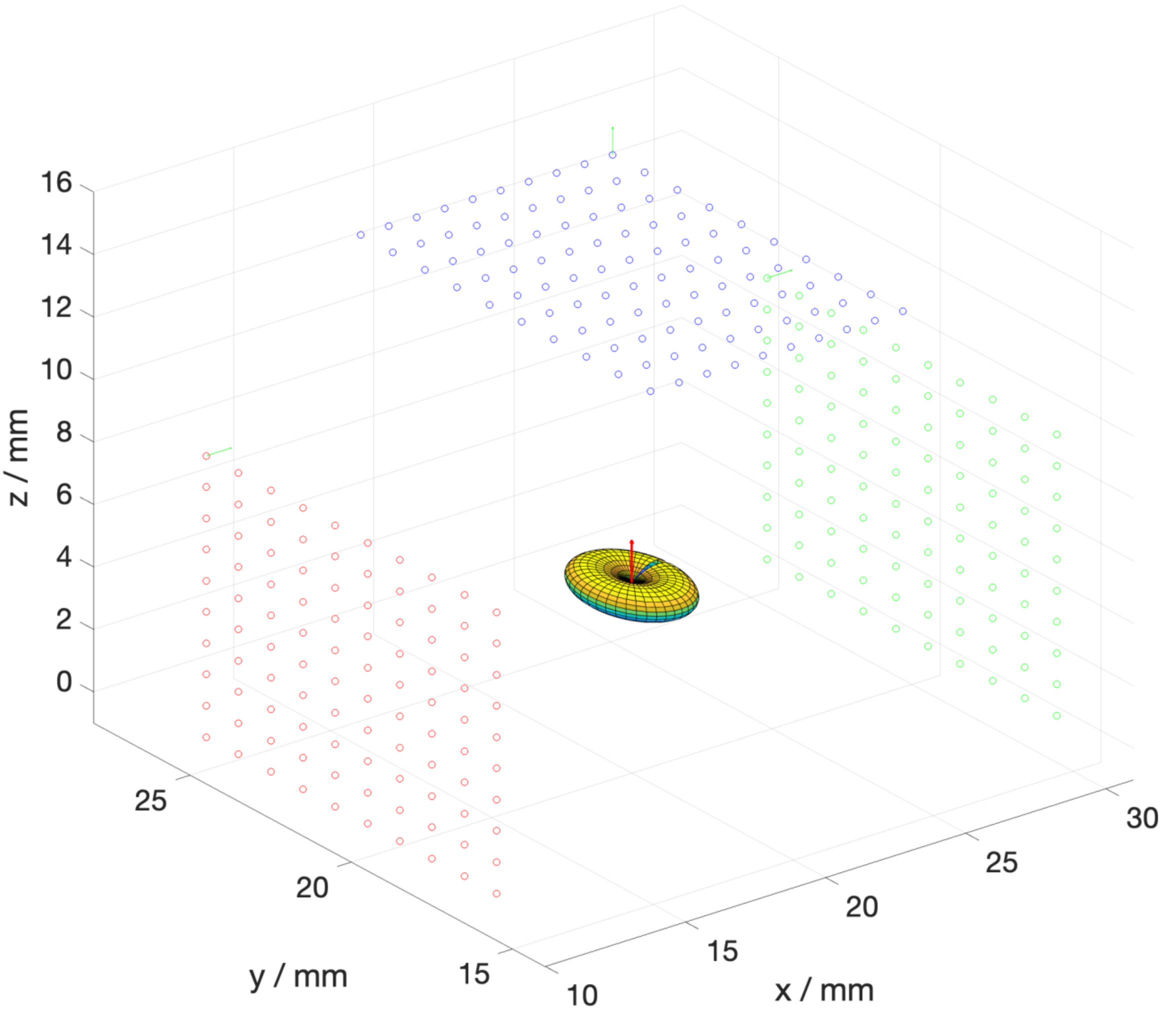

Figure 5.4: The second of two exemplary MATLAB simulation outputs of an ensemble of γ-ray emitting Xe nuclei emitted by a point-like source. Three detectors (green, blue, and red) with 10x10 sensors each are located around a sample of one voxel visualized with a red vector indicating its spin orientation and with a 3D surface plot indicating the directional distribution of emitted γ radiation. Here, γ radiation is emitted anisotropically from (nearly) perfectly aligned spins ($\beta = 10$, $f_1 = 1$, and $f_2 = 0.606$), which is represented as an ellipsoidal 3D surface plot.

longitudinally to $\vec{\mathbf{B}}$. This is a significant change in the count rates of both detectors, which can be used as an efficient way of detecting the change in spin orientation, e.g. under rf excitations, as will be done in the GAMMA-MRI project.

5.3 Numerical results

Here, we present the magnetic substate populations for $^{\text{129m,131m,133m}}$Xe at selected spin temperatures, and the resulting γ-ray counts registered in the detectors placed longitudinally and transversely to $\vec{\mathbf{B}}$ (at 0° and 90°).

5.3.1 Study cases

Fig. 5.5 below presents magnetic sublevel population probabilities p_m for $^{129\text{m},131\text{m},133\text{m}}$Xe corresponding to selected positive β values. Although, unlike real temperature, T_s and β can be both positive and negative, because the angular distribution of γ radiation is a function of even powers of m, it does not depend on the sign of T_s. Therefore, we have selected only positive β values. Selected cases comprise:

- $\beta = 0$ resulting in isotropic γ-ray emission: $p_m = \frac{1}{12} = 0.08\dot{3}$ and all $B_\lambda = 0$;
- $\beta = 10$ giving extremely anisotropic γ-ray emission: $p(m = -11/2) = 0.99995$ (when $\beta \to \infty$, all populations are concentrated in m_{min}: $p(m_{\text{min}}) = 1$ and alignment is maximal: $f_2(\beta = 10) \approx f_2(\beta \to \infty) = 0.606$);
- Intermediate β values, including an example with $\beta = 0.38$, as discussed in [134].

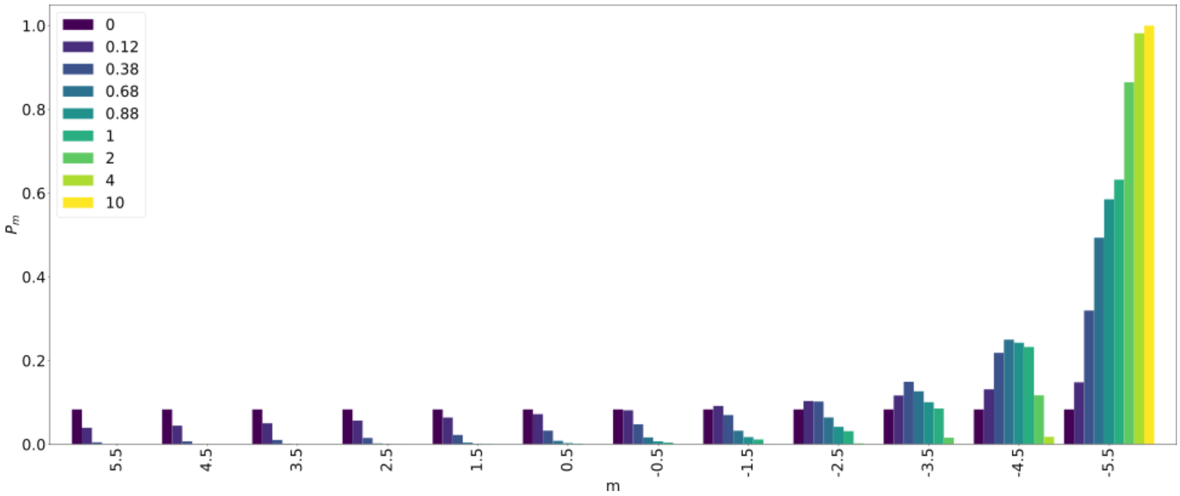

Figure 5.5: Population probability distributions p_m of magnetic sublevels m for mXe with $I_0 = {}^{11}\!/_2$ for selected values of spin temperature parameter β. Values of β are shown in the legend in the top-left corner.

As detailed in Table 5.1 and in the plot of $f_i(\beta)/f_i(\beta_{\text{max}} = 10)$ (Fig. 5.6), analyzed β values span across the entire value range of the f_2 (and f_1) parameter. $\beta = 10$ is close to $\beta = \infty$ because 99.95% of population is in the most extreme substate $m_{\text{min}} = -I$ and alignment value f_2 identical to 5 significant digits. Thus, $\beta = \infty$ was approximated by $\beta = 10$ in simulations input and $\beta = \infty$ was used for normalization.

Table 5.1: Nuclear orientation parameters f_1 and f_2 for studied spin temperature parameter β for mXe ($I_0 = {}^{11}\!/_2$).

β	0	0.12	0.38	0.68	0.88	1	2	4	10
$f_1(I_0)$	0	-0.251	-0.630	-0.814	-0.871	-0.894	-0.972	-0.997	-1.000
$f_2(I_0)$	0	0.025	0.178	0.336	0.405	0.436	0.556	0.600	0.606
$\frac{f_1(I_0)}{f_{1max}(I_0)}$ [%]	0	25	63	81	87	89	97	99.7	100
$\frac{f_2(I_0)}{f_{2max}(I_0)}$ [%]	0	4	29	55	67	72	92	99	100

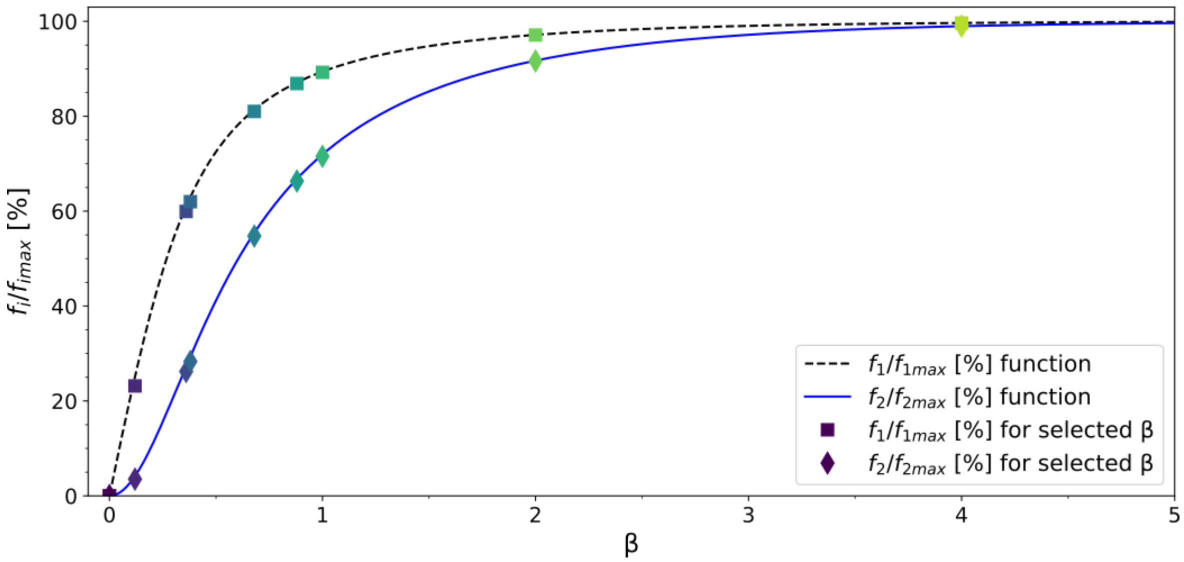

Figure 5.6: mXe spin polarization f_1 and spin alignment f_2 relative to their maximum values ($f_{1\text{max}} = 1$ and $f_{2\text{max}} = 0.606$) as a function of the spin temperature parameter β. $\beta = 10$ was used for normalization, as for this value, extremely high alignment and near-unity polarization are already achieved ($f_2(\beta \to \infty) \approx f_2(\beta = 10)$ and $f_1(\beta \to \infty) \approx f_1(\beta = 10)$).

Note that f_1 and f_2 are not mutually exclusive, and certain distributions of magnetic sublevels can be described simultaneously by non-zero values of polarization and alignment.

5.3.2 Numerical simulation of γ-ray angular distribution $W(\theta)$

For the study cases of mXe, the γ-ray multipolarity is $L = 4$ and thus $\lambda_{\text{max}} = 8$. The angular distribution coefficients A_λ of this transition and the corresponding nuclear orientation coefficients B_λ for selected β values are listed in Table 5.2. As mentioned in Section 5.2.2, we take U_{λ_j}, G_λ, and Q_λ as each equal to 1. Thus, Eq. 5.4 takes the form:

Table 5.2: A_λ and $B_\lambda(\beta)$ coefficients for $M4$ γ-ray transition of $^{129\text{m},131\text{m},133\text{m}}$Xe from I = $^{11}/_2$ to I = $^3/_2$ for selected values of spin temperature parameter β.

λ	2	4	6	8
A_λ	0.89	0.44	0.03	0.26
$B_\lambda(\beta = 0)$	0	0	0	0
$B_\lambda(0.12)$	0.07	$7.4{\cdot}10^{-4}$	$9.8{\cdot}10^{-5}$	$5.6{\cdot}10^{-5}$
$B_\lambda(0.38)$	0.51	0.05	$1.5{\cdot}10^{-3}$	$3.2{\cdot}10^{-5}$
$B_\lambda(0.68)$	0.96	0.22	0.02	$8.5{\cdot}10^{-4}$
$B_\lambda(0.88)$	1.16	0.36	0.05	$3.1{\cdot}10^{-3}$
$B_\lambda(1)$	1.25	0.45	0.07	$5.5{\cdot}10^{-3}$
$B_\lambda(2)$	1.59	0.96	0.32	0.06
$B_\lambda(4)$	1.72	1.23	0.53	0.13
$B_\lambda(10)$	1.74	1.28	0.57	0.15

$$W(\theta) = 1 + B_2 A_2 P_2(cos\ \theta) + B_4 A_4 P_4(cos\ \theta) + B_6 A_6 P_6(cos\ \theta) + B_8 A_8 P_8(cos\ \theta). \tag{5.7}$$

Legendre polynomials P_λ, using Rodrigues' formula, take the representation listed in Table 5.3 for $\lambda = 2, 4, 6, 8$. From Table 5.2, one can see that as a general rule $B_2 > B_4 > B_6 > B_8$. Fig. 5.7 presents the angular distribution of γ radiation for different β scenarios for mXe ($I = {}^{11}/_2$).

Table 5.3: P_λ parameters for $M4$ transition $I = {}^{11}\!/_2$ to $I = {}^{3}\!/_2$ in ${}^{129\mathrm{m},131\mathrm{m},133\mathrm{m}}$Xe.

λ	$P_\lambda(\cos\theta)$
2	$\frac{1}{2}\left(3\cos^2\theta - 1\right)$
4	$\frac{1}{8}\left(35\cos^4\theta - 30\cos^2\theta + 3\right)$
6	$\frac{1}{16}\left(231\cos^6\theta - 315\cos^4\theta + 105\cos^2\theta - 5\right)$
8	$\frac{1}{128}\left(6435\cos^8\theta - 12012\cos^6\theta + 6930\cos^4\theta - 1260\cos^2\theta + 35\right)$

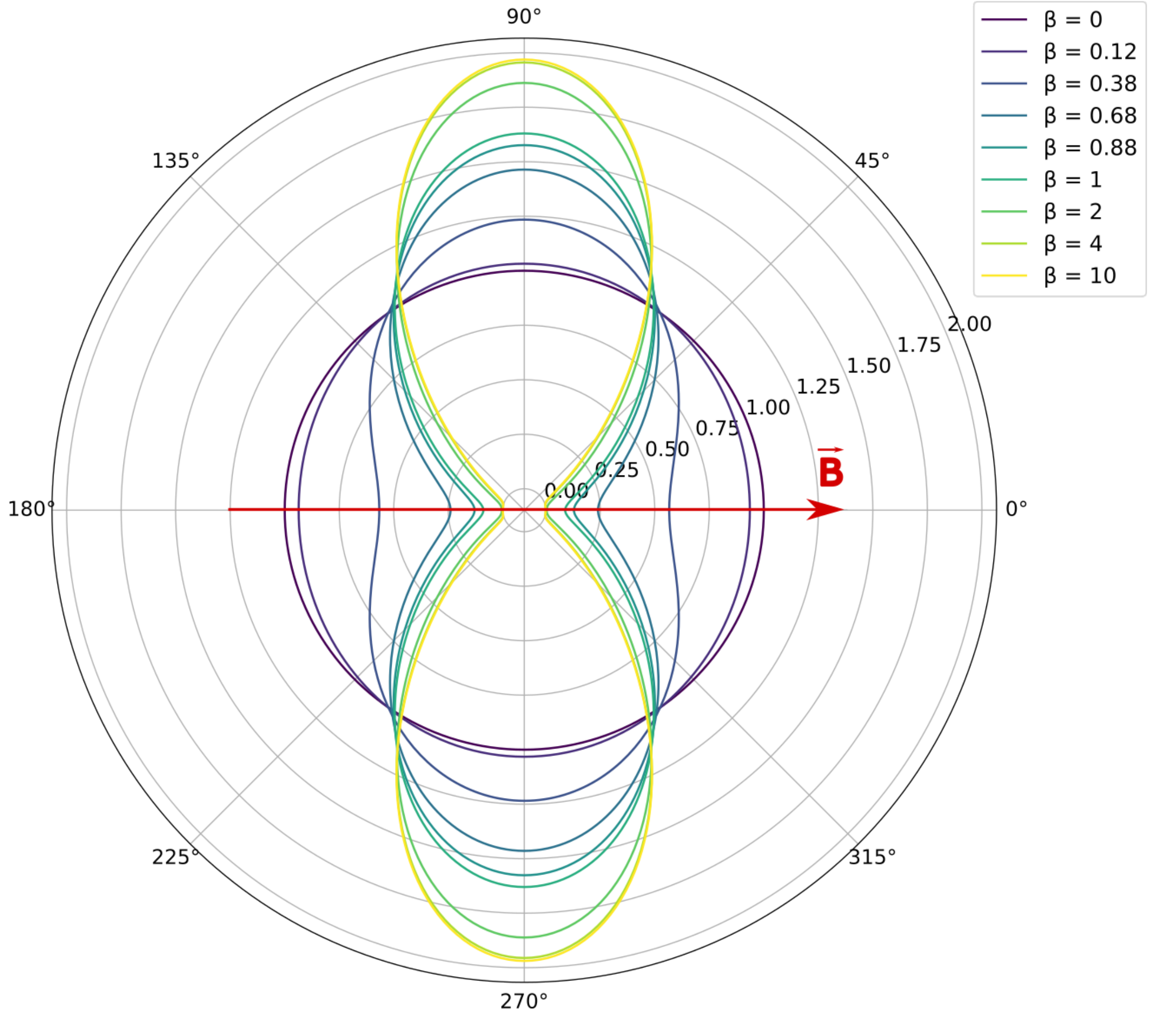

Figure 5.7: The angular distribution $W(\theta)$ of M4 γ radiation from mXe for the simulated cases of magnetic sublevel populations calculated using selected values of spin temperature parameter β. The direction of the external static magnetic field vector $\vec{\mathbf{B}}$ is marked in red. The extreme cases are marked in purple (isotropic emission of γ radiation with $f_2 = 0$ for $\beta = 0$) and yellow (anisotropic emission of γ radiation with $f_{2\max} = 0.606$ for $\beta = 10$). The remaining plots represent $W(\theta)$ for the intermediate values of f_2 and β.

The presented distributions are 2D cross-sections through 3D angular distributions along the $\mathrm{x} - \mathrm{z}$ plane (or $\mathrm{y} - \mathrm{z}$ plane due to the axial symmetry with respect to the x and y axes). Points at angles $\theta = 0^\circ$ and $\theta = 180^\circ$ lie in the axis of the magnetic induction vector $\vec{\mathbf{B}}$, denoted in red in Fig. 5.7. Along this axis, γ-ray emission decreases with an increasing degree of nuclear alignment (and spin temperature β). Points at angles $\theta = 90^\circ$ and $\theta = 270^\circ$ correspond to the plane orthogonal to the magnetic induction vector $\vec{\mathbf{B}}$. Along this plane, γ-ray emission increases with an increasing degree of nuclear alignment.

5.3.3 Simulation of γ-ray asymmetry observed with finite-size detectors

In this section, we look at the asymmetry of γ-ray detection, i.e. the difference in counts registered by finite-size detectors placed at $\theta = 0^\circ$ and $\theta = 90^\circ$ with respect to vector $\vec{\mathbf{B}}$. The detectors are placed around a point-like mXe source, all at the same distance d_{sd}.

Using Eq. 5.7, we first calculate the intensity of γ radiation for $\theta = 0^\circ$ and for $\theta = 90^\circ$, for which the biggest difference in the intensity of the emitted radiation is expected (see also Fig. 5.7 for the graphical representation of these equations):

$$W(0) = 1 + B_2A_2 + B_4A_4 + B_6A_6 + B_8A_8, \tag{5.8}$$

and

$$W(90) = 1 - \frac{1}{2}B_2A_2 + \frac{3}{8}B_4A_4 - \frac{5}{16}B_6A_6 + \frac{35}{128}B_8A_8. \tag{5.9}$$

The resulting γ-ray asymmetry, i.e. relative difference in counts Asm_{Eq} at $\theta = 0^\circ$ and $\theta = 90^\circ$ angles, is given as:

$$\begin{aligned} Asm_{Eq}\left(W(0), W(90)\right) &= \frac{W(0) - W(90)}{W(0) + W(90)} \\ &= \frac{192B_2A_2 + 80B_4A_4 + 168B_6A_6 + 93B_8A_8}{256 + 64B_2A_2 + 176B_4A_4 + 88B_6A_6 + 163B_8A_8}. \end{aligned} \tag{5.10}$$

The values of asymmetry from Eq. 5.10 calculated including only selected B_λ parameters are illustrated in Fig. 5.8 for the range of investigated $\beta \in \langle 0, 10 \rangle$. From the figure, it is clear that one needs to include at least $\lambda = 2$ and $\lambda = 4$ to obtain asymmetry that is close to the value including all four orders of B_λ. As the contribution from $\lambda = 6$ and $\lambda = 8$ is below 2% for $\beta > 2$, and even below $0.2\,\%$ for $\beta \leq 1$, these two terms can be neglected in practical applications. Given that B_2 alone is not enough to describe accurately the decay asymmetry of mXe states, when discussing and interpreting γ-ray asymmetry, one should use both B_2 (alignment) and B_4 or spin temperature β.

Using MATLAB simulations, we then studied the value of experimental asymmetry at selected β values for a point- or finite-size source, and finite-size detectors placed at varying distances d_{sd} representing different solid-angle coverage Ω, as summarized in Table 5.4.

Table 5.4: Size of γ-ray source, distance and size of detectors, and observed asymmetry obtained with a MATLAB code relative to asymmetry for point-like source and detector.

Label	d_{sd} [mm]	Source [mm]	Solid angle Ω [%]	Asm/Asm_{eq}
Asm_{10s3}	10	3	–	0.9614
Asm_{10}	10	point-like	6.45	0.9834
Asm_{20}	20	point-like	1.61	0.9996
Asm_{50s20}	50	20	–	0.9995
Asm_{100}	100	point-like	0.01	1
Asm_{1000}	1000	point-like	$6.45{\cdot}10^{-4}$	1

All datasets obtained from MATLAB simulations used detectors of size $9\text{x}9\,\text{mm}^2$, but a different distance d_{sd} from the source and various sizes of the source. One detector was located at $\theta = 0$,

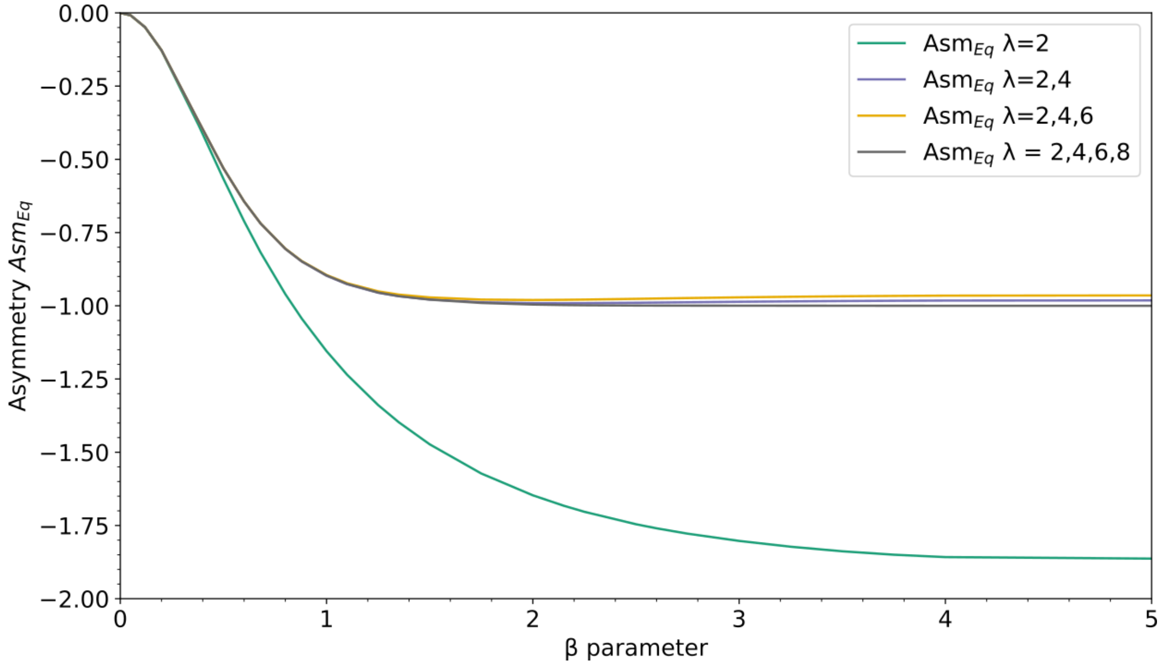

Figure 5.8: Analytical value of γ-ray asymmetry (between $\theta = 0^{\circ}$ and $\theta = 90^{\circ}$) emitted by mXe in the function of spin temperature parameter β. Four plots represent the expansion of $Asm_{Eq}\left(W(0), W(90)\right) = \frac{W(0)-W(90)}{W(0)+W(90)}$ formula to higher orders of λ: only $\lambda = 2$, $\lambda \in \{2,4\}$, $\lambda = \in \{2,4,6\}$, and all orders $\lambda = \in \{2,4,6,8\}$.

i.e. in the plane longitudinal to $\vec{\mathbf{B}}$ (blue detector in Fig. 5.3), while the second - at $\theta = 90$, in the plane transverse to $\vec{\mathbf{B}}$ (green or red detector in Fig. 5.3). All d_{sd} tabulated in Table 5.4 were studied with point-like and finite-size sources, but for larger distances, $d_{sd} = 100\,\text{mm}$ and $1000\,\text{mm}$, no difference in Asm was observed. Thus, Asm values for finite-size sources are presented here only for smaller d_{sd}.

The values of Asm_{sd} for different d_{sd} in the function of spin temperature parameter β are represented with points in Fig. 5.9. For comparison, Asm_{Eq} for $\lambda = 2,4,6,8$ is shown as a black line. All combinations of source and detector size, and distance, reach near-unity asymmetry at $\beta = 10$, except for $d_{sd} = 10\,\text{mm}$. This is because in the latter case, the solid angle covered by one detector is not any more negligible.

5.4 Conclusions and outlook

The purpose of this manuscript was to link the degree of nuclear orientation in metastable states of $^{129\text{m},131\text{m},133\text{m}}$Xe isotopes of spin $I = {}^{11}\!/_{2}$ with the experimental asymmetry of their γ-ray emission. To this end, exact and approximate analytical equations, as well as numerical simulations were used to calculate the number of γ-rays reaching point-like and finite-size detectors placed at 0°and 90°to the spin direction. The study cases presented here correspond to the spin temperature parameter values $\beta \in \langle 0, 10\rangle$, which is expected to describe the distribution of the magnetic sub-level population after Xe orientation with Spin Exchange Optical Pumping.

Nuclear orientation parameters f_1 and f_2, known also as respectively polarization and alignment, were also derived for each spin temperature value. These two parameters are commonly used to

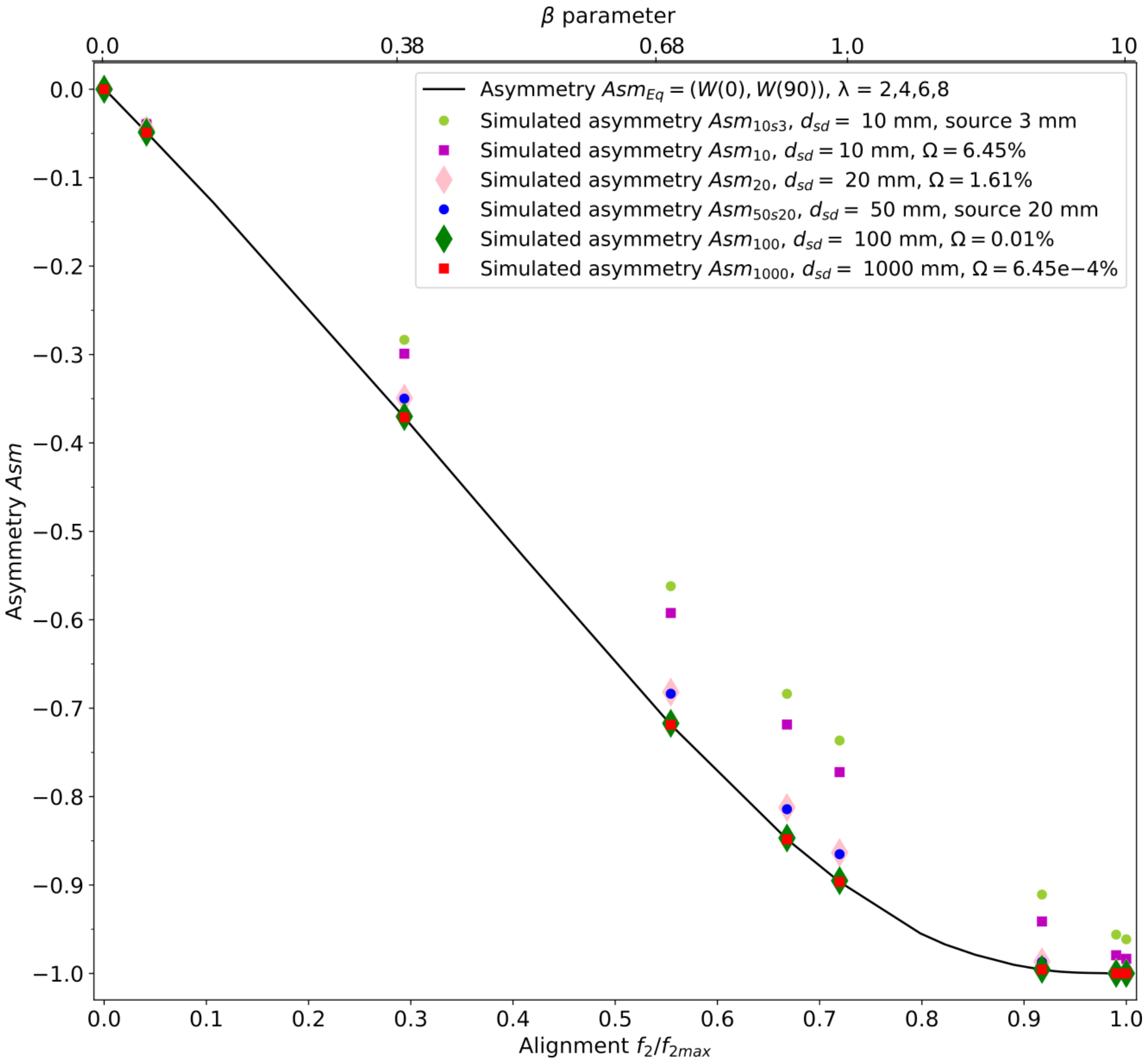

Figure 5.9: Simulated γ-decay asymmetry Asm for different source, detector sizes, and distances d_{sd} as a function of spin temperature parameter β (top x-axis) and the corresponding relative alignment (bottom x-axis, $\frac{f_2}{f_{2\max}}$). For two datasets finite-size source was considered: 3 mm for Asm_{10s3} and 20 mm for Asm_{50s20}. For other datasets, a point-like source was assumed.

describe the nature and degree of spin orientation (it should be noted that they are not mutually exclusive and rather describe different orders/types of spin orientation). Although both are non-zero for most distributions of magnetic sublevels studied here, it is only the alignment that is relevant for the angular distribution of γ radiation. Furthermore, we saw that when assuming spin temperature, a relatively high polarization is accompanied by significantly lower relative alignment, except for high spin temperatures $\beta \geq 2$, where both parameters go over 90 % of their maximal values. For instance, for $\beta = 0.38$ reached in [134] the degree of alignment corresponds to only 29 % of its maximal value, while the polarization is already at 63 %. Similar values were reached by [136].

Parameters A_λ, B_λ and Legendre polynomials $P_\lambda(\cos\theta)$ were then calculated to find the distribution of emitted γ radiation $W(\theta)$ and asymmetry $Asm\,(W(0), W(90))$. B_1 (proportional to spin polarization) and higher B_λ with odd λ do not appear in the equation for $W(\theta)$ in γ decay, while even B_2 (spin alignment), B_4, B_6, and B_8 do. Their values for different β were calculated. Gamma decay asymmetry was then determined analytically for a point-like source and detectors, as well as using MATLAB simulations that included also finite sizes.

Next, the importance of higher-order orientation parameters B_λ was then studied. It was shown in particular that it is necessary to include B_4 parameter, while higher orders B_6 and B_8 can be fully neglected for spin temperature parameter $\beta < 1$, while giving a small, 2% correction for $\beta \geq 2$.

Furthermore, as expected, the smaller the solid angle covered by the detectors, the closer the asymmetry is to the idealized case of point-like detectors at 0°and 90°to the spin direction.

In the GAMMA-MRI project, a high degree of γ-decay asymmetry is desired. We have illustrated here that to achieve this goal, one ideally needs to reach with SEOP such a high spin temperature value that it corresponds not only to a high degree of polarisation, but also that of alignment. In addition, the solid angle covered by the detectors should be as small as possible. Since the physical size of the detectors is a constraint, to increase the asymmetry, one can increase the distance to the source or/and use a small source. However, in the former case, the intrinsic detection probability of the γ-ray detectors and the activity of the γ-ray source have to be high enough to provide sufficient count rate statistics.

Recording angular γ-ray asymmetry is the basis for signal acquisition in the γ-ray detected MRI. For this reason, it was important to calculate the expected asymmetry for a range of experimental parameters, such as detector size and distance, and to test different analytical approximations. Such an analysis, presented in this manuscript, allowed to determine that a high degree of spin polarisation does not guarantee high alignment and high γ-ray asymmetry. Also, certain approximations in the formula describing asymmetric decay are allowed. Finally, detector solid angles below 1 % provide optimal geometries.

The above observations are of use for the GAMMA-MRI project, which aims to bring in a hybrid technique that combines the advantages of magnetic resonance imaging and nuclear medicine imaging.

The current proof-of-concept apparatus being built within that project provides the functionalities necessary for SEOP hyperpolarization and γ-ray asymmetry acquisition. Funding was received from the European Union's Horizon 2020 research and innovation program under grant agreement no. 964644 (GAMMA-MRI) to finance the progress of the prospective setup. The next steps in the project cover among others realistic simulations, including biological modeling of the evolution of oriented mXe *in vivo* in the organ of interest, and the time dependence of the measured signal.

Acknowledgement

The authors wish to thank Dr. Jean-Noël Hyacinthe for early discussions and involvement in this project, and Ms. Emma Wistrom for additional simulations at earlier stages of the project. The authors also wish to acknowledge support via the Swiss Excellence Government Scholarship (to KK), and via the CERN Medical Application Fund (GAMMA-MRI; to RBJ and MK).

Data availability statement

The additional data that support the findings of this study is available upon request.

Conflict of interest

The authors declare that they have no known competing financial interests or personal relationships that could have appeared to influence the work reported in this paper.

Chapter 6

Proof-of-principle experiments: SEOP and γ-ray detection

The first proof-of-principle experiments with hyperpolarization (HP) of produced mXe and detection of emitted γ radiation are described in the following. They are the result of teamwork in the GAMMA-MRI collaboration in the years 2018–2019. The first batch of $^{133\mathrm{m}}$Xe produced at CERN-ISOLDE in 2018 was used for setup validation and protocol testing. Its production was coordinated by S. Pallada and is briefly summarized in Ch. A. The following batches of the long-lived isomers $^{129\mathrm{m}}$Xe and $^{131\mathrm{m}}$Xe produced in 2019 at the High-Flux Reactor (RHF) in the Institute Laue-Langevin (ILL) were used in the HP experiments. Their production and handling were executed by K. Kulesz and are described in detail in Ch. 4.

The hyperpolarization and detection setups were installed at the radioactive ion beams facility ISOLDE at CERN, where the samples imported from ILL were handled. The setup elements and instructions for their operations were provided by the collaboration, mainly:
— prof. M. Kowalska and her group (K. Kulesz, J. Croese, S. Pallada, E.L. Wistrom) from CERN, Switzerland;
— prof. J.N. Hyacinthe and his group (T.P. Lê, E. Vickenbosh) from HES-SO University of Applied Sciences and Arts of Western Switzerland;
— and prof. J.M. Udias and his group (prof. L.M. Fraile, dr J. Benito Garcia, dr M. García-Díez, and dr V. Sánchez-Tembleque) from Universidad Complutense de Madrid, Spain.

The hyperpolarization and γ-ray detection experiments carried out in 2019 and presented in this chapter were performed mainly by K. Kulesz, E.L. Wistrom, M. Kowalska, V. Sánchez-Tembleque, J.N. Hyacinthe, and T.P. Lê. The data collected in 2019 and presented in this chapter was analyzed by L. Dupont, K. Kulesz, and S. Warren.

6.1 Experiment apparatus

The study aimed to conduct proof-of-principle experiments with mXe manipulation, the first ones to be done within the scope of the GAMMA-MRI project. Hyperpolarization of mXe via Spin Exchange Optical Pumping (SEOP) was tested using a benchtop setup and γ radiation from mXe was recorded with 4 detectors placed in the orthogonal planes.

Prior to the experiment, a SEOP-compatible gas mixture was prepared in a glass cell (in SEOP jargon called *a pumping cell*) of 15 cm in length and 7 cm in diameter. First, the pumping cell was filled with 50–90 mg of natural rubidium (with isotopic abundance ratio of ^{85}Rb and ^{87}Rb: 73% and 27%) in the presence of nitrogen buffer gas inside an inert atmosphere glove box, see Figure 6.1. Rubidium has a melting point of 39 °C, and thus upon gentle heating on a laboratory heating plate,

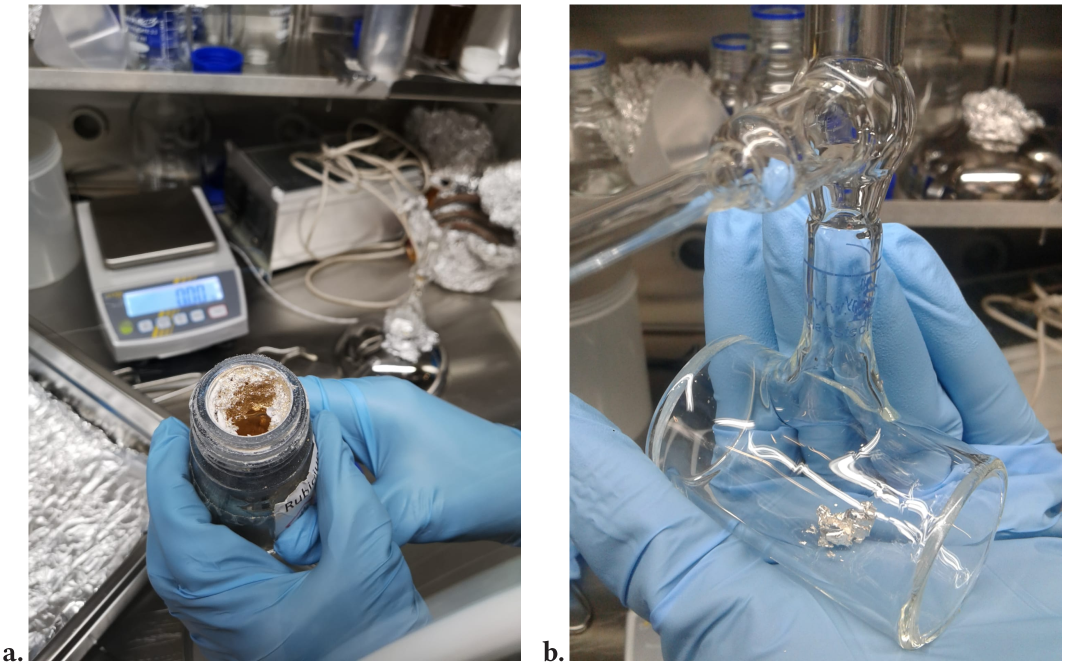

Figure 6.1: Rubidium reservoir filling. Reservoir with rubidium (**a.**) dedicated to storage and a glass cell (**b.**) dedicated to Spin Exchange Optical Pumping (SEOP).

rubidium would reach a liquid state and could be precisely portioned and moved from the storage reservoir to the pumping cell using a metallic spatula.

Next, the cell was attached to a gas system dedicated to SEOP gas mixture preparation. As shown in Figure 6.2, in the gas system there were four segments isolated with the valves: (A) mXe in a transport container, (B) a pumping cell placed in a liquid nitrogen cryotrap, (C) a connection to the pumping system, and (D) high-purity nitrogen grade 5.0 (purity of 99.999%) in a gas bottle with pressure reducer.

The cell was emptied from N_2 buffer gas using the vacuum pump system and refilled with precisely known pressure (from the test range of 50 to 100 mbar) of high-purity N_2. The pumping cell was isolated by closing the valve and the remainder of N_2 was evacuated from the system. Next, the pumping cell volume and mXe segment volume were connected by opening the valves, and mXe gas was collected in the pumping cell using LN_2 cryotrap. Assuming a transfer without loss, the maximum partial pressure of mXe in the pumping cell would be 1.4 mbar. The loss, measured with a Geiger–Müller counter was 10–20 %.

A conventional hyperpolarization setup was modified by the addition of the compact γ-ray detectors, as presented in Figure 6.3. The retained standard elements were: an infrared laser system for optical pumping, the static magnetic field necessary for setting the nuclear orientation axis, and a heating system providing thermal optimum for the SEOP process.

The laser system, labeled **a** in Fig. 6.3 consisted of a compact diode laser (continuous-wave output at 795 nm up to 50 W) from QPC Lasers Co., Ltd. (Sylmar, US-CA), providing circularly polarised parallel beam. The static magnetic field of 4.5 mT was provided by a pair of current-controlled Helmholtz coils, labeled **b**. An insulating oven (**c** in Fig. 6.3) of rectangular shape 20x15x15 cm^3 made of $\mathrm{Ca_2SiO_4}$ accommodated the pumping cell pre-filled with several mg of Rb and the gas mixture of mXe and nitrogen. The cell was placed in the vicinity of the isocenter of the static magnetic field.

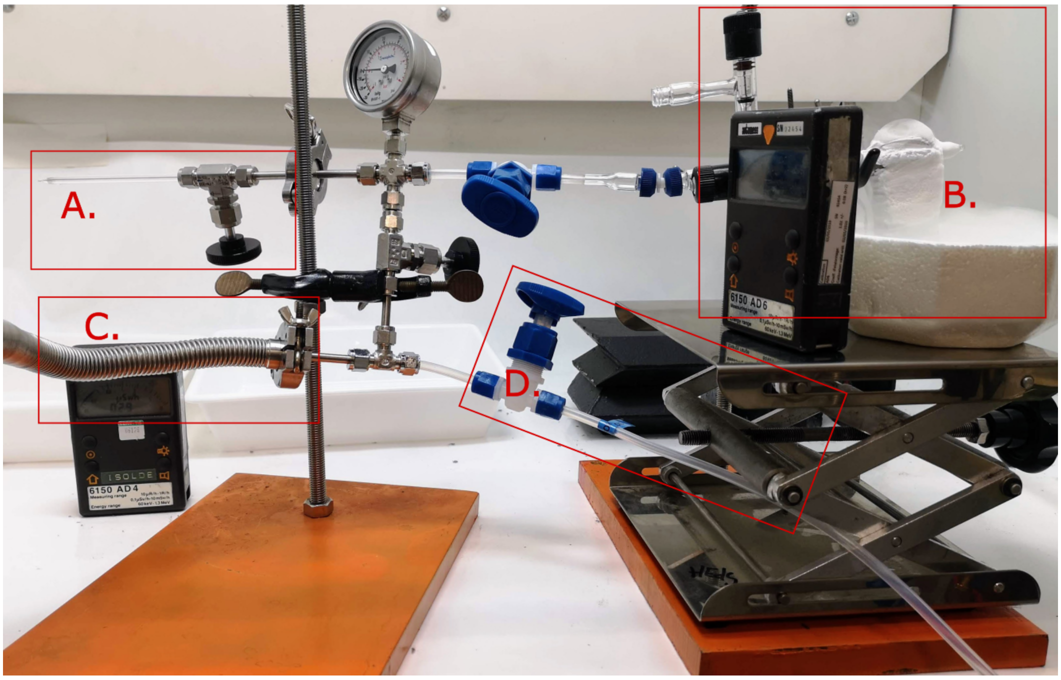

Figure 6.2: Gas system for SEOP (**S**pin **E**xchange **O**ptical **P**umping) cell preparation: A. mXe in a transport container, B. SEOP cell in liquid nitrogen cryotrap, C. a connection to the pumping system, D. a connection to high-purity nitrogen grade 5.0.

The oven had a large circular opening for the laser beam, and a pinhole for the optical fiber mounting on the opposite side of its long axis. A fraction of the laser light transmitted through the cell was registered with an optical fiber coupled to a portable wavemeter, to monitor the absorption of the polarising light by the Rb valence electrons. The cell was heated by hot airflow circulated through the oven's inner volume and controlled with a set of thermocouples. The temperature sensors were coupled to a LabView-controlled feedback loop to provide thermal stability for the pumping cell. The build-up of nuclear orientation of radioactive noble gases was monitored conveniently with fast magnetic-field-compatible gamma radiation detectors instead of rf detection coils used in the conventional SEOP setups. This method offers an advantage over conventional MRI as, unlike radio-frequency (RF) photons, even individual γ ray photons can be detected with high probability.

The selection of gamma detectors was driven by the limited space, by the presence of magnetic fields, and by the expected requirement of high-rate capability. For these reasons, small scintillating crystals coupled to silicon photomultipliers (SiPMs) were chosen. In the experiments three GAGG(Ce) detectors (Fig. 6.4 a.) and a LaBr$_3$(Ce) detector (Fig. 6.4 b.) were used.

Cerium-doped gadolinium aluminum gallium garnet scintillator — GAGG(Ce) — scintillator crystals were chosen due to their high photon yield of over 50 photons per keV, lack of internal activity and large stopping power. Our detectors were composed of 10x10x30 mm^3 GAGG(Ce) crystals coupled to 6x6 mm^2 SiPM photosensors, model S13360-6075CS from Hamamatsu.

The LaBr$_3$(Ce) detector was composed of cerium-doped lanthanum bromide scintillator with a cylindrical shape of 20 mm in diameter and 20 mm in height by EPIC Crystals, coupled to a matrix of 6x6 mm^2 pixels from SensL Technologies Ltd. (Dublin, Irland). This scintillator was chosen based on its very high photon yield of 63 photons per keV and fast decay constant (16 ns), which makes it

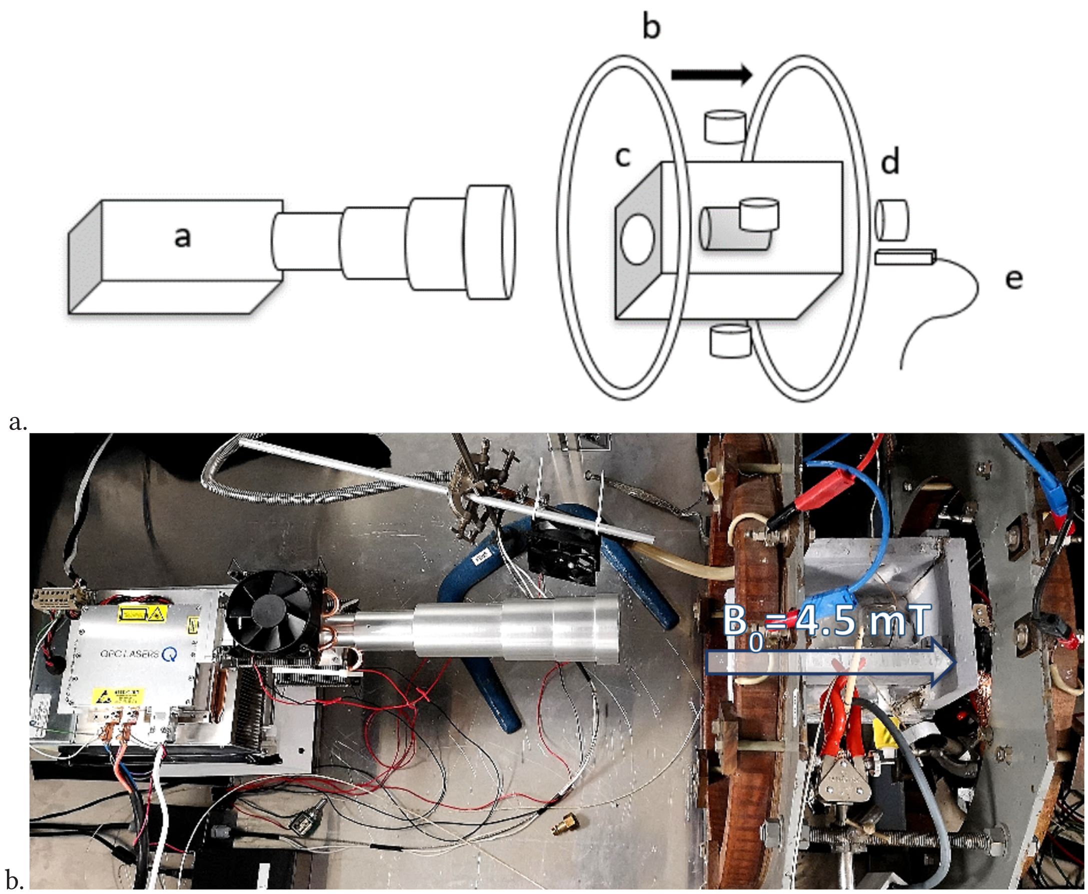

Figure 6.3: The scheme (a.) and the illustration (b.) of SEOP polariser with detectors: (**a**) laser diode array with the telescopic lenses; (**b**) pair of Helmholtz coils; (**c**) insulating oven accommodating the pumping cell; (**d**) set of four SiPMs with: three GAGG(Ce) scintillating crystals and one $LaBr_3$(Ce) scintillating crystal; (**e**) optical fiber for monitoring of polarized light absorption.

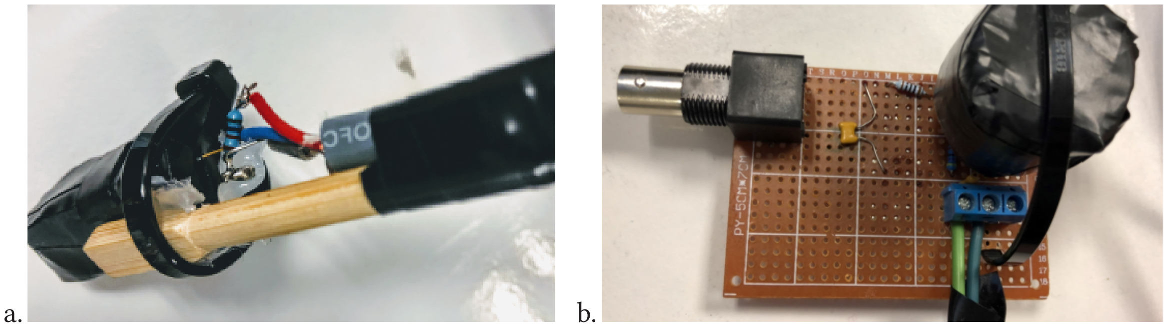

Figure 6.4: Two types of scintillators used in the experiment: a. GAGG(Ce) and b. $LaBr_3$(Ce). As a most external protection, a layer of Tedlar film was used to stop the unwanted light absorption.

suitable for high-rate measurement with a good energy resolution. $LaBr_3$(Ce) has a smaller stopping power than GAGG(Ce), but this was balanced by the larger size of the crystal.

A fully digital DAQ able to acquire about 1 sample every 100 ns per channel was employed, in order to digitize the SiPM signals and to handle large rates with no dead-time losses. This was enough to analyze the pulses, which spanned about 1.5 μs, in the GAGG(Ce)+SiPM combination. In contrast, for $LaBr_3$(Ce), a shaping circuit was employed to stretch the pulses. With this DAQ and detectors combination, we obtained an energy resolution of about 7.5% and 5% for the 662 keV peak [141], for GAGG(Ce) and LaBr$_3$(Ce) respectively [142]. The system used a 4-channel digital oscilloscope (Picoscope 2406B from Pico Technology Ltd., Cambridgeshire, UK)[143] acquiring in streaming mode, in which the signal was digitized and continually sent to the PC in a trigger-less fashion. The software employed a pipeline architecture using multiple threads: two of them reading the scope data, another one identifying pulses from the trigger conditions, removing baseline, performing the energy integral, and writing the binary list-mode event files, and finally the last one performing energy histograms, rates and run time plots.

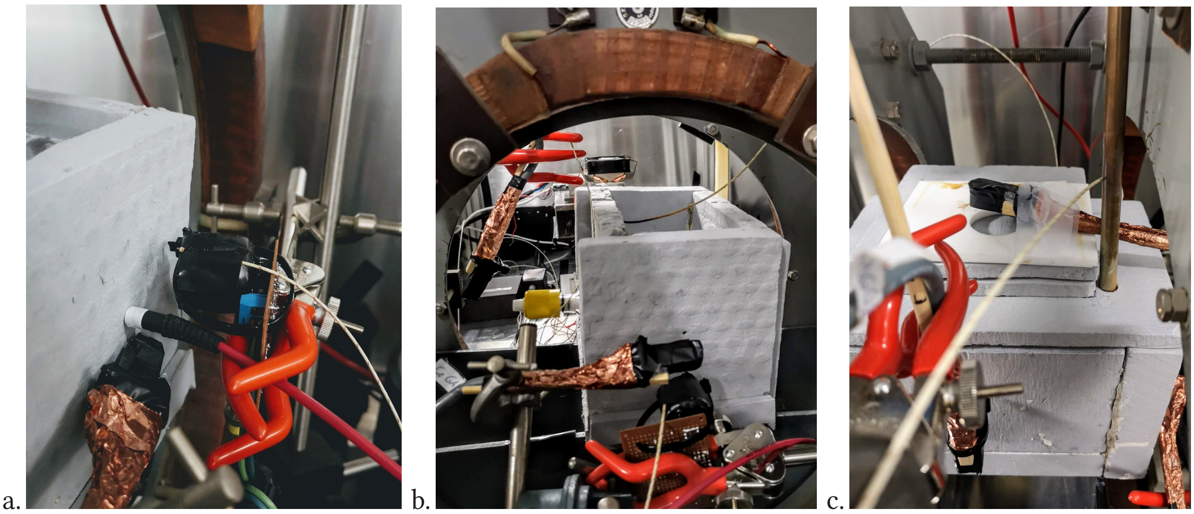
a. b. c.

Figure 6.5: Detectors position as seen: from the back of the oven (a. and b.) and from the top of the oven (c.).

6.2 Experimental protocol

The goal of the experiments was to compare gamma decay spectra of aligned and unaligned mXe.

For the purpose of achieving nuclear alignment, a set of conditions had to be met simultaneously: (i) bringing and maintaining the temperature in the pumping cell at rubidium vaporization point, (ii) placing the cell in a homogeneous magnetic field, (iii) exposing the cell to circularly polarised light resonant with Rb atoms. It was assumed that achieving nuclear alignment takes a minimum of 10-15 min, following the protocols in [144, 145]. It was assumed no-alignment state is when the magnetic field and the laser are turned off.

Detectors were placed as shown in Figures 6.6, three GAGG(Ce) detectors labeled 1/2/3, and a LaBr$_3$(Ce) detector labeled 4. The same numbering of the detectors is used in Section 6.3 for the description of the results. The presented placement of detectors allowed for the acquisition of γ radiation from mXe in the plane (GAGG(Ce) detectors labeled 1,2) which $\vec{\mathbf{B}}$ is normal to, and in the axis of alignment (GAGG(Ce) detector labeled 3 and LaBr$_3$(Ce) detector labeled 4). Those placements correspond, respectively, to angles 90/270 °and 0/180 °described in Ch. 5.

To assure that observables are independent of the parameters of the setup (vibrations, detectors illumination with laser light, magnetic field), the acquisition of γ radiation was carried out with each of the following elements: the laser, the heating, the Helmholtz coils. A temperature-related drift in the

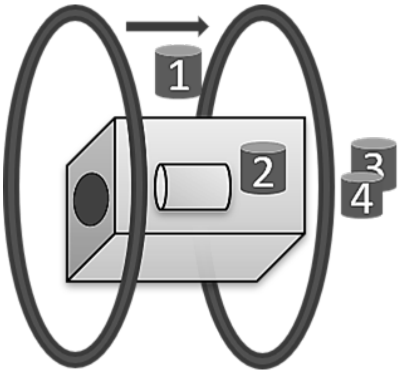

Figure 6.6: Detectors placements (1-4) in the frame of reference of the oven hosting the pumping cell: in the plane (GAGG(Ce) detectors labeled 1,2) which $\vec{\mathbf{B}}$ is normal to, and in the axis of alignment (GAGG(Ce) detector labeled 3 and LaBr$_3$(Ce) detector labeled 4).

detectors' gain amplifiers was observed and appropriate steps were taken to minimize the influence of this drift on the analysis and interpretation, including improved temperature stabilization and time-binned histogram summation. Other effects on the detectors and acquired data were excluded.

To condition the setup for the nuclear alignment, we shone the circularly polarized laser light on the SEOP cell placed in a homogeneous magnetic field while maintaining the cell at the temperature of $110 \pm 4\,^\circ$ C and $150 \pm 4\,^\circ$ C, respectively for $^{129\mathrm{m}}$Xe and $^{131\mathrm{m}}$Xe, as recommended in the literature [83, 102].

The experimental protocol included γ-ray acquisition of tens of minutes in conditions conducive to nuclear alignment and no-nuclear-alignment.

We monitored the count rate in the detectors and the light signal detected by the optical fiber at the axis of the SEOP cell. The recordings were processed after the data collection.

6.3 Data analysis and results

The collected data was processed with C++ and Python scripts, with the use of ROOT libraries. Gain-shift was corrected by the implementation of time bins of several seconds. These short-time-acquisition spectra were energy calibrated using the peaks of mXe γ transitions as reference. This resulted in multiple "scans" of 10-second-long time bins and 5-keV-wide energy bins for the GAGG(Ce) detectors and 2-keV-wide energy bins for the LaBr$_3$(Ce) detector, due to its higher energy resolution. These scans underwent automated analysis where: (i) mXe peaks at 196.56 keV and 163.93 keV (isomeric transitions of $^{129\mathrm{m}}$Xe and $^{131\mathrm{m}}$Xe to ^{129}Xe and ^{131}Xe, respectively) were identified in spectra, (ii) the peaks were fitted with a single Gaussian function, as shown for $^{129\mathrm{m}}$Xe in Figure 6.7, and (iii) the area of the fit was calculated for each scan. The area $N(\mathrm{det})$ of the Gaussian fit for each detector was used to determine the number of γ-ray counts resulting from the isomeric transition. An exemplary scan is presented in Figure 6.7.

As seen in the spectra, a non-negligible number of γ rays was scattered in the experimental setup, resulting in lower energy than the energy of the isomeric transition counts registered by the detector. When the energy range for Gaussian fitting included the region where the tail started being visible, it would decrease the quality of the fit (evaluated by the χ^2 value). Therefore, through

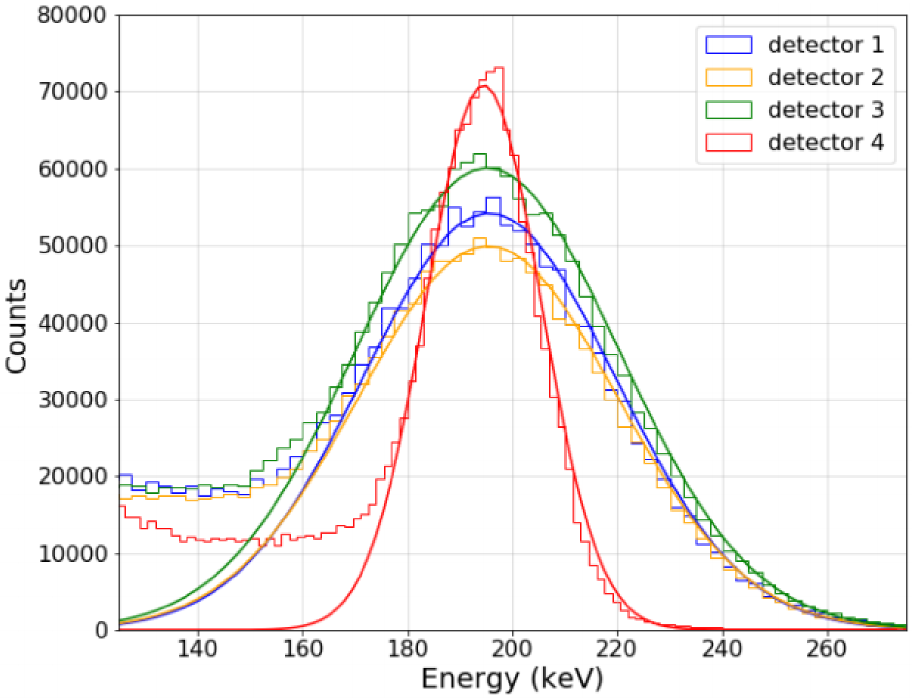

Figure 6.7: Calibrated gamma spectra of $^{129\mathrm{m}}$Xe acquired with the four detectors (1-3: GAGG(Ce), 4: LaBr$_3$(Ce)). Note the better energy resolution of the LaBr$_3$(Ce) detector. Single Gaussian fitting was applied using the optimal binning parameters: 10-second-long time bins for energy calibration, energy bins of 5 keV (GAGG(Ce)) and of 2 keV (LaBr$_3$(Ce)), fitting range above 170 keV (GAGG(Ce)) and above 180 keV (LaBr$_3$(Ce)).

systematic checks, the energy range corresponding to the best fit was found for GAGG(Ce) and LaBr$_3$(Ce) detectors (e.g. for $^{129\mathrm{m}}$Xe: > 170 keV and > 180 keV, respectively). The goodness of the fit was also confirmed with the χ^2 test.

The area $N(\mathrm{det})$ under each fitting curve was the starting point to calculate the percent difference in the number of counts registered by each pair of the detectors (difference $\delta(\mathrm{det_i}, \mathrm{det_j})$:

$$\delta(\mathrm{det_i}, \mathrm{det_j}) = \frac{N(\mathrm{det_i}) - N(\mathrm{det_j})}{N(\mathrm{det_i})} \cdot 100\%, \tag{6.1}$$

where $N(\mathrm{det_i})$ and $N(\mathrm{det_j})$ are the numbers of counts as calculated by integration of the counts in the fitted Gaussian over the full energy range. The absolute number of counts would change with the width parameter of the energy bin, but the relative magnitude of the change was almost the same for all detectors. Thus, although the absolute number of the γ-ray counts might have had a systematic offset, it didn't influence the final difference $\delta(\mathrm{det_i}, \mathrm{det_j})$.

In Figure 6.8, the count differences $\delta(\mathrm{det_i}, \mathrm{det_j})$ acquired in a long acquisition from $^{129\mathrm{m}}$Xe are presented. Data sets $\delta\ (4/1)$ and $\delta\ (3/2)$ represent the count difference for the detectors placed in the same plane that is normal to the alignment axis. There, $\delta\ (4/1)$ and $\delta\ (3/2)$ should remain indifferent with respect to conditions of nuclear alignment. On the contrary, $\delta(2/1)$ and $\delta(4/3)$ represent the count difference for the detectors in the axis of alignment and orthogonal to it.

In the first half of the run, until 1250 s, the magnetic field providing the quantization direction is not present, and thus, there's no nuclear alignment of $^{129\mathrm{m}}$Xe. After 1250 s, all conditions necessary for the successful nuclear alignment of $^{129\mathrm{m}}$Xe spins are met. The difference in counts seen by the

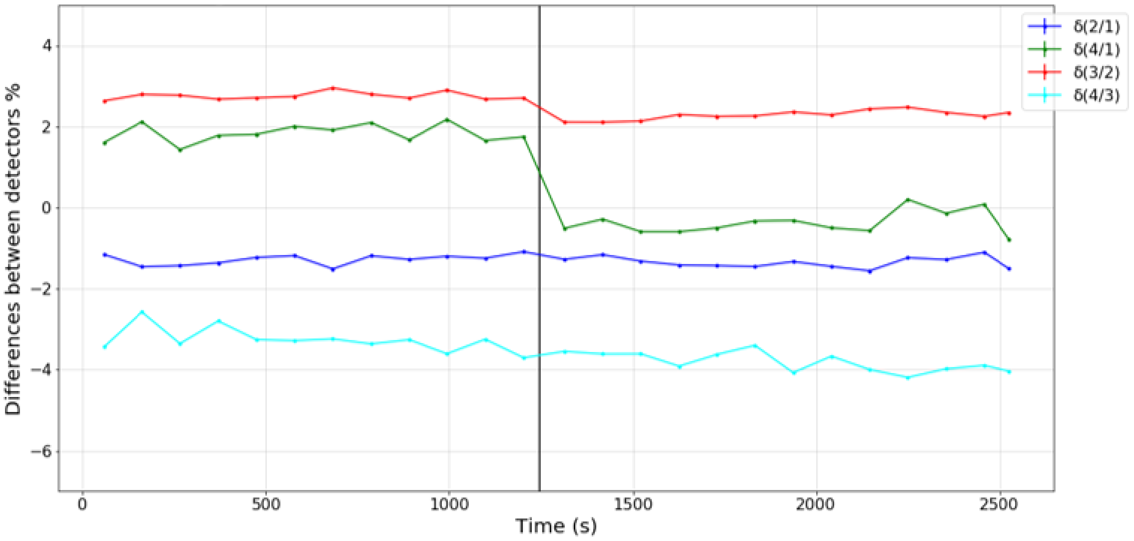

Figure 6.8: The figure representing the difference in the γ-ray counts in the experimental conditions between *no alignment* and *alignment* states. Percent difference (and asymmetry) in γ-ray counts is observed by different pairs of detectors (transversal detectors - dark blue, longitudinal detectors - light blue, transversal versus longitudinal - red and green). Timeframe 0–1250 s: the magnetic field is not present. Timeframe 1250–2550 s: all conditions for successful mXe orientation are met. Note the change in counts for green and red curves when the magnetic field was turned on, but not the blue ones.

detectors placed in the same plane ($\delta(2/1)$ and $\delta(4/3)$) doesn't experience a change at the moment when the magnetic field is turned on. On the contrary, the count difference (and asymmetry) of 1 to 2% is visible for the pairs of detectors situated in orthogonal planes (δ $(4/1)$ and δ $(3/2)$). Although small, this count difference is consistently present in the made recordings. This observation is in line with the γ-ray asymmetry simulations corresponding to the mXe population preferentially in substates with higher absolute |m|, as expected from the SEOP process.

6.4 Discussion

In this chapter, the first proof-of-principle (POP) experiments for mXe alignment and γ-ray asymmetry detection were reported. The dedicated setups for mXe alignment and for γ-ray asymmetry detection were constructed and commissioned. A standard SEOP setup was used and adapted to the project with the application of the state-of-the-art γ-ray detectors — fast and efficient, magnetic-field compatible and extremely compact $LaBr_3(Ce)$ and GAGG(Ce) scintillating crystals coupled to Si photomultipliers. The polariser with compact gamma detectors was enclosed in a transportable aluminum rig (see Figure 6.3) that can be implemented in laboratories already engaged in the polarisation of stable Xe or very close, if not within, a hospital. This was dictated by laser safety concerns but also made the whole system mobile. However, without properly controlled air circulation, the temperature inside the rig proved to be highly variable, to the extent that it affected the response of gamma detectors. Thus, an air-cooling system had to be designed, which allowed for regulated temperature control.

After the test runs, the first alignment studies with produced radioisotopes were performed. The experimental protocols were designed such that, as the magnetic field (the axis of nuclear orientation) is present, the change in γ-ray counts observed in different detectors can be tested to prove the presence of the asymmetry of the angular distribution of emitted γ-rays.

The asymmetry of 1–2% was recorded. These experiments showed that mXe isomers can be aligned and even if the degree of asymmetry is small (and significantly smaller than that of ^{129}Xe), it is still detectable. In that regard, the POP experiments not only proved the feasibility of this technique but also validated the choice of used γ-ray detectors and stimulated the development of the data analysis pipeline of energy spectra. The asymmetry value is limited by the degree of nuclear spins' alignment and the solid angle of γ-ray acquisition. Further systematic studies of SEOP optimization and of γ-ray acquisition are thus required. Next, they could be combined with the rf excitation and MRI-type images.

Chapter 7

Discussion

This thesis presented the initial technical developments of GAMMA-MRI and proof-of-principle experiments proving the feasibility of the technique. GAMMA-MRI strives to combine the best in the MRI and SPECT techniques to provide high-resolution single photon imaging using highly aligned γ-ray-emitting nuclei. Thus, unlike the existing dual-modality imaging instrumentation that superposes images produced independently by MRI and SPECT, the approach of GAMMA-MRI combines the physics behind these two techniques. GAMMA-MRI technique development includes: (1) optimization of xenon production and purification, (2) obtaining and maintaining the highest possible nuclear spin alignment, and (3) efficient data acquisition strategy to limit acquisition time to a maximum of several minutes using gradient coils for testing two- and three-dimensional image acquisition, rf coils for excitations, and high-countrate, magnetic-field compatible γ-ray detectors for asymmetry registration.

The thesis covers the subject of mXe production, alignment, and detection, in particular:

- mXe production via neutron activation and via the decay of the mother isotopes for mXe,
- proof-of-principle experiments of mXe alignment and detection
- the theoretical study of the nuclear orientation and corresponding alignment.

7.1 Metastable xenon production

7.1.1 Summary: produced activity and sample purity

Table 7.1 summarizes the production methods of metastable xenon introduced within this manuscript. The values exclude possible extraction or cry-collection factors. Only ISOLDE production can be used for the production of all 3 demanded isotopes. It is also currently the only method that can deliver $^{133\mathrm{m}}$Xe.

Each method is evaluated with different parameters and thus different units: [MBq/h] for ISOLDE, [MBq μmol $\cdot$ cm$^2\cdot$ s] for Reactors, and [MBq per 100 MBq of ^{131}I] for ^{131}I. A comparison of methods will be given in Table 7.2 in the subsequent subchapter on the example of 10 MBq of mXe activity being a minimum benchmark for GAMMA-MRI project [115].

In Chapter 3, a thermal sublimation generator of the long-lived excited state (isomer) $^{131\mathrm{m}}$Xe was reported on. This production method utilized the decay of ^{131}I, obtained commercially from a pharmaceuticals supplier and relying on a flexible delivery schedule (medical ^{131}I is available > 350 d/yr). γ-ray spectroscopy showed that with consecutive heat treatments between 40 °C and 400 °C and cryogenic trapping of released $^{131\mathrm{m}}$Xe, up to 88(3)% of the estimated produced $^{131\mathrm{m}}$Xe was collected. An encouraging fact is that up to 69% can be collected at room temperature without complicating the system with the heat treatments. The combined efficiency of the $^{131\mathrm{m}}$Xe cryo-collection and of the ^{131}I powder twas up to 82(4)%. Precisely, the activity of collected $^{131\mathrm{m}}$Xe ranged

Table 7.1: Overview of mXe production. The production rates use different normalization and, thus, different units for each described method. The activities are given for the end of collection/irradiation.

Isomers	**ISOLDE** [MBq/h]	**Reactors** [MBq μmol · cm^2· s]	^{131}**I** [MBq per 100 MBq of ^{131}I]
^{129m}Xe	0.70(5)	7 – 17	Not applicable
^{131m}Xe	1.2(1)	8 – 18	0.00323(1)
^{133m}Xe	3.1(2)	Not produced	Not applicable
	Combined extraction and cryo-collection efficiency [%]		
	70(3) – 73(3)	76(2) – 92(2)	53(3) – 82(4)
	Radionuclidic and chemical purity[%] (normalized to mXe activity)		
^{129m}Xe	^{129}Xe ground state	^{131m}Xe <0.21, ^{133m}Xe <0.02, ^{133}Xe <0.01, ^{127}Xe <0.03	Not applicable
^{131m}Xe	^{131}Xe ground state	^{129m}Xe <0.05, ^{133m}Xe <0.005, ^{133}Xe <0.007, ^{127}Xe <0.04	^{131}I <0.19, stable ^{131}Xe
^{133m}Xe	^{133}Xe, assumed isomeric ratio of ^{133}Xe to ^{133m}Xe was 0.77:0.23 [146]	Not produced	Not applicable
	Cost scalability per 10 MBq of mXe		
	low	medium to high	high
	Dose to operator per 10 MBq of mXe *		
	varying, but low	medium	high
	Production time flexibility		
	rather low	average	very high
	Extraction time flexibility		
	average	average	average
	Facility availability		
	April – Nov	3 – 4 cycles (150 – 200 days)	close to 365 days/year

* Evaluated in the framework of the dose limits in the occupational exposure

from 99(2) to 204(1) kBq for the ordered batches of ^{131}I, 50 MBq each at delivery but with different pre-history of ^{131m}Xe saturation. With no pre-history of ^{131}I powder saturation with ^{131m}Xe the produced ^{131m}Xe activity would be 0.323 MBq per 100 MBq of decaying ^{131}I. This method provided an isomeric mixture of ^{131m}Xe and ^{131}Xe.

In Chapter 4, the production of xenon isomers ^{129m}Xe and ^{131m}Xe via neutron activation in High Flux Reactor at ILL and in MARIA reactor at NCBJ was presented. Since the reactors operate with different fluxes and even for each of them the variance of the activity of the samples was up to 40%, the results were normalized and presented as the production rates, i.e. defined as the molar activities [MBq/μmol] normalized to the thermal neutron flux applied [cm^{-1}· s^{-1}]. γ-ray spectroscopy done on all samples upon reception from HFR and MARIA allowed for determining the slope of the linear regression fits to be: $7.35 \cdot 10^{-14} [\frac{\text{MBq}}{\mu\text{mol}} \cdot \text{cm} \cdot \text{s}]$ for ^{129m}Xe and $8.34 \cdot 10^{-14} [\frac{\text{MBq}}{\mu\text{mol}} \cdot \text{cm} \cdot \text{s}]$ for ^{131m}Xe. These values are in good agreement with the literature values. The distribution of the production rate in Figures 4.4 and in the mXe activity in different vials can be explained by the differences in the following parameters:

- Neutron flux, which decreases as the fuel element is used up throughout the cycle,
- Position of the capsule with samples within the shaft

- Length of irradiation: the nominal value was 7 days,
- Initial amount of material sent for irradiation (varying by 10% due to the flame-closing of the ampoule).

This has led to variation in the production rate up to a factor of 5. The cry-collection efficiency was 76(2)–92(2)%. In terms of the GAMMA-MRI project's requirements, all neutron-activated samples had sufficient activity to allow for subsequent sample manipulations.

In Annex A, the production of ^{129m}Xe, ^{131m}Xe and ^{133m}Xe isomers in the radioactive-ion-beam facility ISOLDE was described. The results reported by Mateusz Chojnacki in [147] show the production rates delivered of 0.70(5) MBq/h, 1.2(1) MBq/h, 3.1(2) MBq/h respectively for ^{129m}Xe, ^{131m}Xe, ^{133m}Xe. As reported in [148], the fluctuations of mXe yields were up to a factor of 100 with the possibility to improve the aforementioned production rates. This is because it depends on the proton beam intensity, target material and its behavior under a pulsed proton beam and heating to high temperatures, efficiency of ionization and of extraction, efficiency of transmission, and material chosen for collection/implantation. All these factors weigh into the final reproducibility. The extraction efficiency was 84(1)% and cryo-collection efficiency was 81(3)% – 87(2)%. Thus far, it is the only method that accomplished the production of all 3 isotopes.

In the ISOLDE collections, the contaminants can come from the impurities present in the beam with mass A around that of collected xenon and from heating the oxidized foils. However, it should be noted only the volatile contaminants that freeze in the LN$_2$ would be transferred with mXe while others would deposit on the inner surface of the UHV setup or simply not adsorb efficiently to the cold surface of the cryo-trap. The pressure at the moment of Xe transfer higher than the radioactive content would suggest pointed to the presence of non-radioactive contaminants from the setup out-gassing and the diffusion from the implantation foils. That happened despite the high-temperature annealing of the foils prior to the implantation. The amount of stable contaminants can be minimized in the future by keeping the implanted foils under a vacuum between the annealing, implantation and extraction.

Detailed analysis of γ-ray spectroscopy of the samples received from the reactor and the neutron activation calculated for the stable Xe samples with CASTOR software established the stable and radioactive contaminants of samples from the reactor. The main contaminants present in the ampoules and collected in the cryo-traps were listed in Chapter 4 (and summarized in Table 7.1) and these were isotopes of xenon and possibly Kr isotopes (sublimation pressure at LN2 temperature would cause them to adsorb to the cold surface of the trap) but in the amount below the threshold of the minimum detectable activity in the γ-ray spectroscopy. Separation of these isotopes from ^{129m}Xe and ^{131m}Xe can only be done by methods such as state-of-the-art gas centrifugation and in gas quantities larger than the samples dealt with. However, owing to their high biocompatibility and more so useful anesthetic effect, their presence is not harmful for a prospective patient but it can add to the complexity of SEOP dynamics. Other isotopes calculated to have been co-produced in the ampoules (e.g. ^{125}I, ^{78}Kr, ^{127}I, ^{126}I, ^{125}Te) have short half-lives (from seconds to hours) or don't get adsorbed at the cryotrap.

γ-ray spectroscopy confirmed the radionuclide purity of the delivered sample. The only radioactive contaminant present in the $^{131\text{m}}$Xe sample was ^{131}I with the activity <0.19% that of activity of $^{131\text{m}}$Xe. The capsule was received with the ingredients added to the powder in the course of chemical treatment of the powder for pharmaceutical applications (referred to as *excipients*). Amongst them, the most abundant were: disodium phosphate dihydrate (229.2 mg), sodium thiosulphate (22.9 mg) and sucrose (22.9 mg). We avoided heating the powder to outgas these ingredients because it could cause a loss of $^{131\text{m}}$Xe and ^{131}I. The gas pressure at the order of individual mbar present in the HV setup (10^{-6}mbar) points to the presence of stable contaminants i.e. mostly ground state 131Xe and decomposed excipients ingredients (phosphate molecules, CO_2, H_2O).

These findings are important as for the moment metastable radioactive xenon is not present in the commercial offer of the radiopharmaceuticals suppliers. In the following, the comparison of these methods is given, the advantages and the inconveniences of each method are discussed, and the recommendations for future production are given.

7.1.2 Comparison of mXe production techniques

The necessary $^{131\text{m}}$Xe activity in GAMMA-MRI project is: 50–100 MBq and 10–30 MBq, respectively for the polarization optimization and for proof-of-principle experiments in a preclinical MRI device built within the GAMMA-MRI project [115]. Table 7.1 presents the comparison of the conditions necessary for achieving 10 MBq using each of the techniques. Thus, the listed activity values account for losses present during extraction and cryo-collection steps (their efficiencies listed in Table 7.1).

Table 7.2: Comparison of the mXe production in reference to 10 MBq activity benchmark in the GAMMA-MRI project. The activities produced via the three described production routes are derived using the aforementioned production rates.

Evaluation criteria	**$^{129\text{m}}$Xe**	**$^{131\text{m}}$Xe**	**$^{133\text{m}}$Xe**
ISOLDE: collection time [h]	20.4 h *	11.9 h *	4.6 h *
HFR: number of ampoules for 10 MBq	16 – 29	9 – 26	Not produced
MARIA: number of ampoules for 10 MBq	3 – 8	2 – 7	Not produced
^{131}I: min. mother activity	Not applicable	4140 MBq	Not applicable

* Extrapolated based on minutes-long collections.

Presented collection time at ISOLDE is relatively long and has not yet been optimized as mentioned in the previous subchapter. However, even with the current production rates, the goal of 10 MBq is feasible for all 3 mXe isomers. Given that the reproducibility of the mXe yield is improved, RIB method could offer the best control and flexibility over the produced activity. Scaling this production method up would imply implanting more mXe ions in a single collection matrix — feasible up to the handling limit imposed by radioprotection regulations.

Neutron activation in HFR and MARIA reactor can already provide for multiple 10 MBq batches of $^{129\text{m}}$Xe or $^{131\text{m}}$Xe from just a single ampoule. $^{133\text{m}}$Xe isomer was not yet produced using this method.

Production of $^{131\text{m}}$Xe from ^{131}I decay was done with the maximum quantity of ^{131}I that can be handled in a class C laboratory. The minimum activity of ^{131}I necessary to obtain the benchmark of

10 MBq of $^{131\text{m}}$Xe would be 4.14 GBq. This value is within the limits of what the radiopharmaceuticals provider can deliver in the form of a single capsule. ^{131}I is a β, γ-emitter. Due to the high stopping power of electrons in tissue and the high dose effective dose to the operator, it is recommended not to increase the ^{131}I activity to such an amount. In addition, in such circumstances, the cost of the ^{131}I batch and the effort into collective and personal radiological protection would increase significantly.

7.1.3 Time and schedule

Nuclear facility operation time depends on many factors including the frequency of maintenance, the dependence on the existing infrastructure, and the staffing. To use these facilities for mXe production, a scientific proposal or access request has to be submitted several months in advance of experiments and it must include the desired dates of experiments (i.e. date, the desired number of shifts at RIB or the desired number of ampoules with the Xe sample).

Moreover, in the framework of GAMMA-MRI, a RIB facility is only of use if it can produce the mXe beam, i.e. has the specific target material (e.g. UC$_x$, TC$_x$, molten lead), sufficient proton beam energy, and the technology to extract mXe from the target and deliver it to the collection site. Each year ISOLDE is in operation for several months. That usually is mid-May – mid-November every year, except every 5 – 6 years, when maintenance and upgrade periods take place at CERN. Based on the ISOLDE schedule, a team can expect to be assigned 2–4 'beamtimes' per year, each being about 2–5 days long. The beamtime preparation including, the foils annealing and UHV setups testing requires about 4 weeks of preparations for newly designed setups, and 1 week for pre-existing setups.

Owing to the high cross-section of the reactions with xenon, neutron activation for GAMMA-MRI can take place in any reactor with the minimal thermal flux of $6.5 \cdot 10^{13}$ and $4.7 \cdot 10^{13}$ neutrons per cm^2 per s, respectively for $^{129\text{m}}$Xe and $^{131\text{m}}$Xe. Like ISOLDE, the reactors are also subject to longer shutdowns due to maintenance and upgrades every few years. Each year HRF-ILL provides 150 – 200 days of the neutron beam, usually divided into 3–4 cycles, about 50-day-long each in between which fuel element exchange and the maintenance works take place. The stable xenon ampoules can be prepared using the setup in Figure 4.1 at a frequency of up to 6 ampoules per day. The samples need to reach the reactors prior to the irradiation allowing for the time necessary for ampoules and capsules preparation for lowering into the reactor's pool, i.e. 4–6 weeks for ILL-HFR and 1 week for MARIA. Upon delivery to CERN, the handling of irradiated samples depends on the availability of the laboratories. 1 to 2 working days should be accounted for the steps from the reception of activity at CERN to the cryotrapping of xenon at the collection vial. Once the radioactive surface contamination of the ampoules is removed, the extraction of mXe from ampoules and the transfer to the reusable container can be performed multiple times per week. Each of the activated ampoules can serve for multiple batches of 10 MBq activity of mXe.

Sodium iodide ^{131}I capsules are manufactured in the network of nuclear facilities and they are distributed by a pharmaceutical company to the hospitals on a weekly basis throughout the year. The shipped activity is tailored to match the ordered value within 10% uncertainty on the day prior to the delivery at 12:00 pm. The activity can be tailored to the needs of the customer within 37 MBq to

7.4 GBq range. There are no schedule limitations to commercially obtain ^{131}I throughout the year in the quantities required for GAMMA-MRI needs as long as the receiving laboratory allowed to handle this special isotope is available. For a given activity of ^{131}I, the activity of Xe produced via ^{131}I decay can be precisely estimated, although due to the history of each ^{131}I batch and its saturation level with $^{131\mathrm{m}}$Xe, the amount of extracted $^{131\mathrm{m}}$Xe might be higher than anticipated. Regardless of the initial handled ^{131}I activity, the total production, extraction, and collection time amounts to 14 days if the maximum activity of $^{131\mathrm{m}}$Xe is to be collected.

7.1.4 Costs and radiological risks

All 3 production routes required a high vacuum environment and consumables related to maintaining it. In addition, certain shared ISOLDE equipment (e.g. annealing furnaces, high resolution γ-ray detectors) was available free of charge.

Access to ISOLDE beams was free of charge after the acceptance of the scientific proposal. The incurred costs thus involved the equipment and consumables bought explicitly for the project, i.e. metallic foils and collection chamber adjustments. Since the handling of the foils post-collection was in-house, no costs of radioactive shipping were involved at that point.

The collection at ILL was free of charge, as it took place within the scientific collaboration of GAMMA-MRI. The main expenses incurred at the preparation stage were the isotopically enriched stable xenon supplied in small bottles (^{128}Xe and ^{130}Xe) and the high-purity quartz vials for irradiation. In addition, the transport fees of radioactive samples from ILL to CERN were the ampoules were further manipulated had to be handled.

The main cost of the method of $^{131\mathrm{m}}$Xe production via ^{131}I decay was the cost of that isotope paid to the pharmaceutical distributor. In the event of scaling the produced activity of $^{131\mathrm{m}}$Xe up to the GAMMA-MRI benchmark, the cost of the initial 4.14 GBq activity of ^{131}I used for the decay would be 3.5 times higher than for the batch used in the performed experiments.

Prior to the experiments, the radiological analysis was performed using Nucleonica and CERN internal software to determine the dose rates, allowed working distance and time, and the minimum manpower. Throughout the work time with radioactive specimens, the effective dose and the absorbed dose were always monitored and discussed. Table 7.3 lists the ambient dose rates H*(10) at a working distance of 40 cm (the distance between the source and the detector/operator) for handled isotopes present with the highest activity. To compare the dose rates, the same nominal value of 10 MBq activity was used. The dose rates H*(10) of $^{129\mathrm{m}}$Xe, $^{131\mathrm{m}}$Xe, and $^{133\mathrm{m}}$Xe are identical regardless of the production method. High licensing limits (*limite d'autorisation LA*) allow for working with large activities of mXe in low-level radiological laboratories.

The dose received by the operators in ISOLDE collection remained at a low level compared to the two remaining methods. The main contribution to that dose comes from mXe and the radioactive contaminants which varied significantly (and included at times isotopes of ^{131}I and ^{133}I whose radiation has a high biological effect) across the collections.

Table 7.3: Ambient Dose Rate H*(10) at a working distance of 40 cm (the distance between the source and the detector/operator) for handled isotopes with the highest activity. For comparison, 10 MBq activity benchmark of the GAMMA-MRI project was used.

Isotope	**Calculated ambient Dose Rate H*(10) [μSv/h]**
^{129m}Xe	2.022
^{131m}Xe	0.8244
^{133m}Xe	1.072
^{131}I (10 MBq)	4.092
^{131}I (4140 MBq)	$1.694{\cdot}10^{3}$
^{24}Na	30.79
^{182}Ta	11.98

The dose received by the operators in the neutron activation was medium to high. That is mainly because the ampoules had to be cleaned from the surface contamination (a mixture of radioisotopes e.g. ^{24}Na, ^{182}Ta, ^{183}Ta) upon arrival to CERN and prior to that they were manually placed in the transport container in the hall of the nuclear reactor.

The dose received by the operators of a thermal generator of ^{131m}Xe in ^{131}I decay would be the highest, in particular, if 10 MBq of ^{131m}Xe was to be produced.

7.1.5 Summary and recommendation

Based on the studies performed until now, there is no one route that is superior to the others for all the aforementioned points. The three explored routes of mXe production differ in the isomers' variety, purity, and production rates, in the schedule flexibility, costs, dose rate, and the time of mXe handling. Due to their high production rates with respect to costs and radiological exposure, ISOLDE and nuclear reactors are more beneficial to obtain the benchmark activities for GAMMA-MRI operations. The production at ISOLDE brings hundreds of MBq activity, but it is seasonal, it depends on the overall ISOLDE schedule, relies on an accepted scientific proposal and has to be requested at the beginning of the calendar year with the exact date and number of beamtime shifts being refined several months before the collection. ISOLDE production allows for the biggest flexibility in collected activity. It can be tailored to the demands of the user who has control over the time of the collection. The neutron activation method can provide the biggest activity which makes it suitable for the planned intense demand on xenon supplies. The procedures of ^{129m,131m}Xe extraction from the neutron-activated quartz ampoule and the collection in the cryotrap are well understood and under control. The produced activity fluctuates by up to a factor of 5. The production schedules at ILL and MARIA are less seasonal than at ISOLDE, but they are subject to longer shutdowns every few years. The exact production time has to be planned several months in advance and includes specifying the number of ampoules lowered into the reactor's pool. The sublimation generator represents a way to obtain low-activity batches of ^{131m}Xe with high radionuclidic purity throughout the year, piggybacking on the well-established distribution network of ^{131}I capsules. It is a good complementary method that is independent of the operation schedules of nuclear facilities and it allows for the production of small batches of ^{131m}Xe that can serve SEOP setup validation. Even though feasible it is not advised to scale the production of ^{131m}Xe up to 10 MBq, because of the high β, γ dose rate to the operator.

7.2 Hyperpolarization and detection

A dedicated polarisation and γ-ray asymmetry detection setup has been constructed and commissioned. After the setup validation tests, the first nuclear orientation studies with produced radioisotopes were performed. They showed that mXe isomers can be aligned and that the γ-ray asymmetry, which is at the heart of the GAMMA-MRI technique, can be recorded with the γ-ray acquisition system prepared for this project.

The quality of images that GAMMA-MRI will deliver is limited by the maximal attainable angular asymmetry of the spatial distribution of γ radiation emitted by mXe. Obtaining a high degree of nuclear spins' alignment and achieving a high purity of the radioactive sample can only be achieved by having a rigorous and reliable mXe production and purification methods combined with an optimised SEOP setup, and by ensuring the reproducibility of these initial steps.

Table 7.4 presents a comparison between conventionally used Xe SEOP and mXe hyperpolarisation studies of GAMMA-MRI, Zheng *et al.* [136], and Calaprice *et al.* [134]. mXe-based approaches can work with $\sim 10^{10}$ nuclei, in comparison with much higher requirements when using stable ^{129}Xe. However, ^{129}Xe has no electric quadrupole moment, while ^{129m,131m,133m}Xe do. This significantly decreases their spin relaxation times due to the interaction of the quadrupole moment with the electric field fluctuations and gradients in the environment. GAMMA-MRI is the only group to make attempts at performing SEOP with a variety of 3 isomers produced via different techniques. The activity used by [136] and [134] is 37 MBq i.e. 1 mCi. That is within the range established in the GAMMA-MRI project.

Table 7.4: Comparison of xenon production and polarisation approaches used by GAMMA-MRI, by Zheng *et al.* [136], by Calaprice *et al.* [134], and by conventional SEOP of stable ^{129}Xe [149].

Parameters	**GAMMA-MRI**	**Zheng *et al.***	**Calaprice *et al.***	**conv. SEOP**
Xe isotopes	129m, 131m, 133	131m	131m, 133m, 133	129s
Production	RIBs, neutron activation, ^{131}I decay	^{131}I decay	RIBs	purchase
Activity [MBq]	10 – 100	37	0.37	0
Atoms number	10^{14}	10^{13}	10^{11}	10^{24}
Cell coating	no	yes	no mention	yes
Temperature [°C]	100–190	140, 190	110–160	100
Static field [mT]	4.5	0.7	0.2	2.7
Laser power[W]	50	40	0.4	25
Detection	$LaBr_3$(Ce), GAGG(Ce) with SiPMs	NaI with PMs	Ge(Li)	rf coils
γ-ray asymmetry as "$f_i/f_{imax} \cdot 100$"	asymmetry<2% i.e. f_2<2%	f_1 = 60% i.e. f_2 = 28%	f_2 = 29%	not applicable

In all cases of metastable xenon studies, a standard SEOP setup was adapted by the replacement of the signal acquisition system. In GAMMA-MRI, a fast and efficient, magnetic-field compatible and extremely compact solution was applied: $LaBr_3$(Ce) and GAGG(Ce) scintillating crystals coupled to Si photomultipliers. In [136] semiconductor γ-ray detectors coupled to a conventional photomultiplier were used, while the Calaprice group [134] used liquid nitrogen-cooled Ge(Li) detectors with the highest resolution of the solutions discussed.

Calaprice *et al.* [134], reported 29% of maximum possible alignment f_2 (similarly for ^{133m}Xe and ^{133}Xe) and a 56% change in γ-ray counts for the one detector placed parallel to the magnetic field. That change is defined as a ratio of counts registered at two different points in time: with and without nuclear alignment. Using the definition given in Equation 6.1 the change reported in [134] would amount to 40%. Zheng *et al.*[136] reported f_1 = 60% of maximum possible polarization, which, as proven in Figure 5.1, amounts to the alignment f_2 = 28% of maximum possible alignment. In the GAMMA-MRI experiments presented in this manuscript, the experimental asymmetry values of 1% to 2% were obtained which according to the calculations in Figure 5.9, could extrapolate to f_2/f_{2max} = 1–2% and f_1/f_{1max} = 20%

In spite of the differences in parameters describing the γ-ray asymmetry, the GAMMA-MRI results are still an order of magnitude lower than the literature values reported in Table 7.4. Several possible causes are investigated. Firstly, the GAMMA-MRI experiments involved large solid angles of γ-ray asymmetry acquisition and that was due to the large dimensions of the pumping cell and its relatively small distance to the detectors. As given in Figure 5.9 that could not be the unique cause. Secondly, the SEOP configuration was not yet fully optimized for maximum alignment production rate and minimum relaxation rate. Additional pumping cells with and without coating should be tested as well as the gas mixtures of various total gas pressures.

7.3 Conclusions and outlook

The final goal of the FET-funded GAMMA-MRI project is to develop a pre-clinical prototype of an innovative biomedical imaging modality. As a whole, the milestones of the project aims to: (i) produce and hyperpolarize efficiently several radioactive isotopes of xenon (mXe) with optimized properties, (ii) use biocompatible encapsulation strategies to maintain the hyperpolarisation of mXe in vivo on the order of several seconds to reach the targeted site from the administration site; (iii) develop imaging sequences based on fast MRI- and emerging AI-based strategies to obtain images in minutes; (iv) develop compact, fast, magnetic-field-compatible high-performance γ-ray detectors and electronics; (v) build a pre-clinical prototype for in vitro and in vivo demonstration of the GAMMA-MRI technique; (vi) and record the first in vivo GAMMA-MRI image of a rodent's brain using the prototype and hyperpolarized mXe. In addition, contextual information on future developments is included in publications i.e Chapters 3, 4, and 5, in Chapter 6 describing the POP experiments and below:

- Improvements to the collection of ^{129m}Xe, ^{131m}Xe at RIB facility, ISOLDE are planned. The UHV extraction and collection setups that allow minimizing the amount of oxygen and water vapour are already in use. Xe neutron activation and thermal generator of ^{131m}Xe are already well optimized, but a relatively pure and intense production of ^{129m}Xe, ^{131m}Xe with an enhanced reproducibility to reach up to 50 MBq for each isomer can be still achieved. That would require to amount to a yield of $5{\cdot}10^8$ ions/s, i.e. 1.6 MBq/h for ^{129m}Xe and 1.2 MBq/h for ^{131m}Xe.
- Obtaining and maintaining the highest possible mXe spin alignment. This will also include the investigation of Xe cages, in case longer relaxation times are needed. A setup with improved air circulation will be tested with different buffer gas ratios in uncoated and coated pumping

cells. The γ-ray acquisition setup will be modified from the hardware side, by additional temperature-stabilised LaBr3(Ce) scintillators coupled to SiPM and from the software side, by an intuitive user-interface and online data analysis.

- A tailor-made preclinical-size magnet was already tested with ^{1}H MRI and is ready to be incorporated into the GAMMA-MRI prototype, where the optical pumping system was already installed. At present, detector calibration and polarisation tests with $^{129\mathrm{m}}$Xe from reactors are ongoing. Once the radioactivity has decayed away, stable Xe polarisation and ^{129,131}Xe NMR inside the prototype will be tested.

The consortium (established between the University of Applied Sciences and Arts of Western Switzerland (HES-SO), the University of Maastricht, the Complutense University of Madrid, CERN, KU Leuven, and the two companies RS2D and Tecnologias Avanzadas Inspiralia SL) will work on the optimization of all these aspects of GAMMA-MRI, and on the design of a preclinical prototype to explore the advantages, and constraints, of this technology.

Appendices

Appendix A

mXe production at CERN-ISOLDE

The results presented here are, for the most part, the effects of the work of Stavroula Pallada (2018 experiments) and Mateusz Chojnacki (2021 and 2022) and serve merely for comparison (in Chapter 7 with techniques presented in Chapters 3 and 4. My contribution to both works was limited either to assisting in the experiments (data curation in 2018) or to conceptualization and methodology (in 2021/2022) due to prior-assembled installations for xenon extraction. The full scope of the work will be available in the doctoral thesis of Mateusz Chojnacki.

Xenon beams are produced at the ISOLDE facility [150] at CERN when bunches of 1.2 GeV-protons from PSB impinge on thick targets to produce a wide variety of unstable nuclei. In the case of mXe, one uses thorium carbide (ThC$_x$) or uranium carbide (UC$_x$) target heated to 2000° C and coupled to a plasma ion source with a cooled transfer line (to eliminate less volatile elements from the beam). The extracted beam is then accelerated to 30–60 keV and mass-separated using a dipole magnet. mXe is then implanted into a host, e.g. a thin metallic foil, before being extracted from it by foil outgassing at high temperature and enclosed in a tight container suitable for gas transport.

In the first stages of the GAMMA-MRI project covered by the present publication, the feasibility of mXe production at ISOLDE was tested during two experiments in 2018. The encouraging results led to more experiments in 2021 and 2022, which will be presented in a separate article by M. Chojnacki *et al.* In the mentioned experiments the isotopes with the interesting mass/charge ratio (i.e. A = 129, 131, or 133) were transported through the GPS (General Purpose Separator) magnet and collected on thin foils at the GLM (General Low Mass) beamline (see Figure A.1, top). In 2018 different implantation materials were tested, including tantalum, carbon, and aluminum (see Figure A.1, bottom) to optimize subsequent xenon extraction. In 2021/2022, silver and golden foils were used.

In 2018 the collected activity of $^{133\mathrm{m}}$Xe was measured to be between 80 and 270 MBq for different foils (the differences were mostly due to the time of the collections, not the implantation material). γ-ray spectrometry for each foil showed the purity of the implanted beam. In 2018 experiments with $^{133\mathrm{m}}$Xe, the activity came mostly from the ground- and isomeric-state of ^{133}Xe, with very small contributions from isobars or neighboring masses: $^{133,133\mathrm{m}}$Ba, $^{135,135\mathrm{m}}$Xe, ^{131}La, ^{131,133}Sb, ^{133}I. Small quantities of ^{235}U, ^{57}Co, and ^{201}Tl were also detected which came most probably from previous collections in the GLM chamber. γ-ray spectrometry showed also that $^{133\mathrm{m}}$Xe, corresponded to 70% of the total ^{133}Xe activity. In 2021 and 2022, the production rates delivered by Mateusz Chojnacki could be summarized to 0.70(5) MBq/h, 1.2(1) MBq/h, 3.1(2) MBq/h respectively for $^{129\mathrm{m}}$Xe, $^{131\mathrm{m}}$Xe, $^{133\mathrm{m}}$Xe. Detailed xenon yields measured in 2021/2022 are presented in Figure A.2. mXe yields had fluctuations of up to 2 orders of magnitude [148]. The beam purity characteristic was also not reproducible. The team addressed these issues by concentrating on understanding the lack of results' reproducibility: the use of the main GLM chamber without connecting a dedicated chamber to ensure high beam purity and the use of the short test collections in aluminum foils with varying parameters

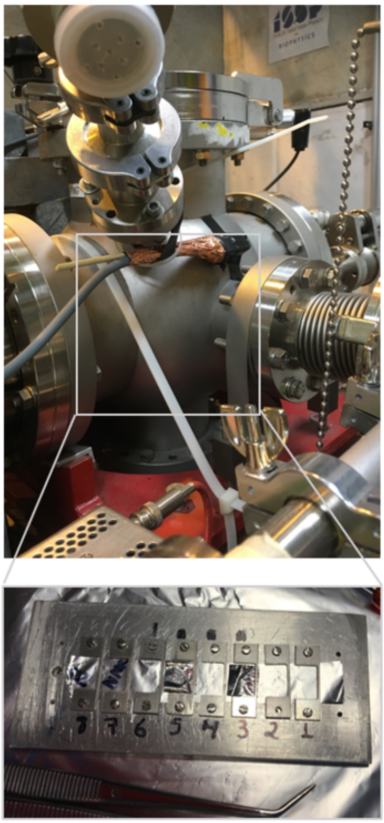

Figure A.1: Top: Collection chamber at the end of the General Low Mass beamline at ISOLDE-CERN. Bottom: Implantation matrices of Ta, C, Ni, Al, Ti mounted on an Al sample holder in 2018. Different implantation materials were tested to optimize subsequent xenon extraction.

to characterize the mXe yield. The contaminants present in the beam and implanted in the foils were in the region of A $\in < 129, 133 >$. The details are presented in the Master thesis of Ilaria Michelson [146].

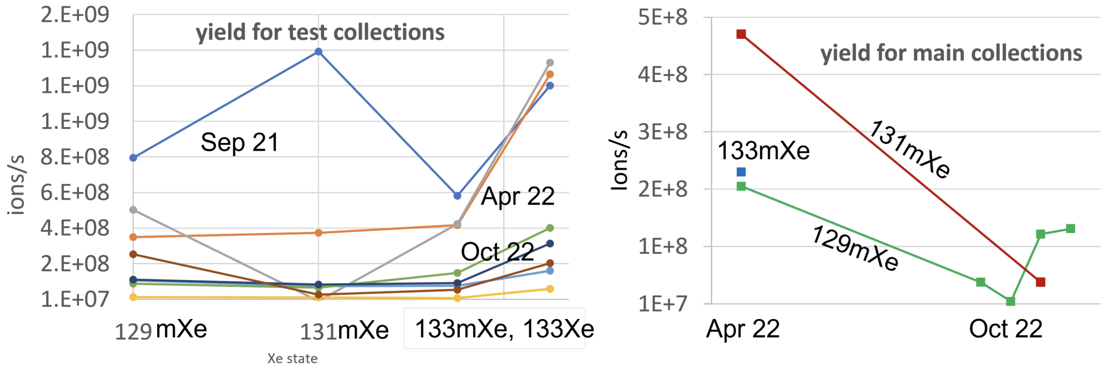

Figure A.2: Xenon yields in 2021 – 2022 collections measured with the high-resolution γ-ray spectroscopy. Source: [148].

After a several-hour-long collection on GLM, the sample holder with foils was removed from the GLM collection chamber, and exposed to atmospheric conditions. Next, they were placed one-by-one in a quartz vial (see Fig. A.3 right) within a vacuum system (10^{-6} mbar) dedicated to xenon separation. The quartz vial was inserted into an annealing furnace (see Fig. A.3 left) and heated for tens to hundreds of minutes to a few hundred degrees to release the implanted xenon. Xenon was captured inside a cryotrap — a separate vial immersed in a LN_2 bath.

Gamma spectroscopy revealed the combined extraction and cryo-collection efficiency was around 20(1)%, with an average collected ^{133m}Xe activity of 30 MBq in 2018. In experiments in 2021 and 2022 this efficiency was improved significantly. As reported by Mateusz Chojnacki in [147] extraction efficiency was 84(1)% and cryo-collection efficiency was 81(3)% – 87(2)%.

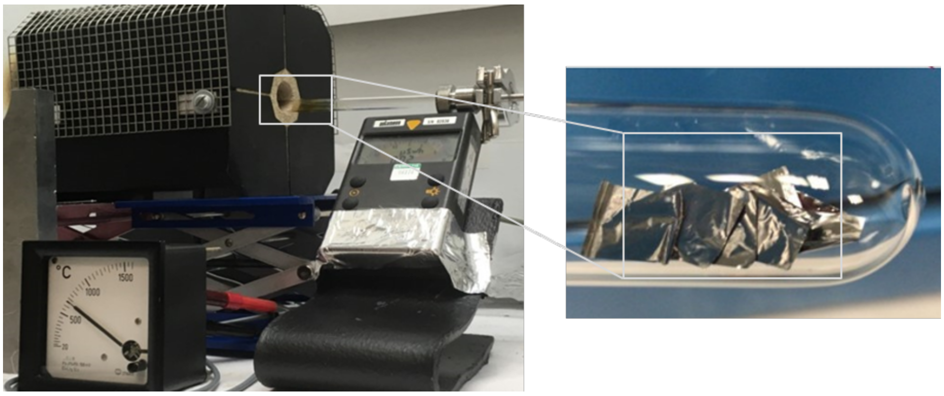

Figure A.3: Annealing furnace (left) used for heating the quartz tube with mXe collection foils (right).

Bibliography

[1] V. Kuperman. *Magnetic resonance imaging : physical principles and applications.* Academic Press, 2000, p. 182. ISBN: 0080535704. URL: https://books.google.com/books/about/Magnetic_Resonance_Imaging.html?id=DGnVDgTfcZwC.

[2] S. Vandenberghe, P. Moskal, and J. S. Karp. "State of the art in total body PET". In: *EJNMMI Physics* 7 (1 Dec. 2020), pp. 1–33. ISSN: 21977364. DOI: 10.1186/S40658-020-00290-2/FIGURES/16. URL: https://ejnmmiphys.springeropen.com/articles/10.1186/s40658-020-00290-2.

[3] F.-M. Lu and Z. Yuan. "PET/SPECT molecular imaging in clinical neuroscience: recent advances in the investigation of CNS diseases." In: *Quantitative imaging in medicine and surgery* 5 (3 June 2015), pp. 433–47. ISSN: 2223-4292. DOI: 10.3978/j.issn.2223-4292.2015.03.16. URL: http://www.ncbi.nlm.nih.gov/pubmed/26029646%20http://www.pubmedcentral.nih.gov/articlerender.fcgi?artid=PMC4426104.

[4] S. Mattsson and M. Söderberg. "Radiation dose management in CT, SPECT/CT and PET/CT techniques". In: *Radiation Protection Dosimetry* 147 (1-2 Sept. 2011), pp. 13–21. ISSN: 01448420. DOI: 10.1093/rpd/ncr261.

[5] *What are the Radiation Risks from CT? | FDA*. https://www.fda.gov/radiation-emitting-products/medical-x-ray-imaging/what-are-radiation-risks-ct. Accessed: 2023-05-22.

[6] J. E. Streeter *et al.* "Improving Sensitivity in Ultrasound Molecular Imaging by Tailoring Contrast Agent Size Distribution: In Vivo Studies". In: *Molecular imaging* 9 (2 Mar. 2010), p. 87. ISSN: 15353508. DOI: 10.2310/7290.2010.00005. URL: /pmc/articles/PMC2945694/%20/pmc/articles/PMC2945694/?report=abstract%20https://www.ncbi.nlm.nih.gov/pmc/articles/PMC2945694/.

[7] F. A. Mettler *et al.* "Effective doses in radiology and diagnostic nuclear medicine: a catalog". In: *Radiology* 248 (1 July 2008), pp. 254–263. ISSN: 1527-1315. DOI: 10.1148/RADIOL.2481071451. URL: https://pubmed.ncbi.nlm.nih.gov/18566177/.

[8] M. N. Hoff *et al. Safety considerations of 7-T MRI in clinical practice.* 2019. DOI: 10.1148/radiol.2019182742.

[9] B. Vachha and S. Y. Huang. *MRI with ultrahigh field strength and high-performance gradients: challenges and opportunities for clinical neuroimaging at 7 T and beyond.* Dec. 2021. DOI: 10.1186/s41747-021-00216-2.

[10] M. E. Ladd *et al. Pros and cons of ultra-high-field MRI/MRS for human application.* Dec. 2018. DOI: 10.1016/j.pnmrs.2018.06.001.

[11] M. Dahlbom. *Physics of PET and SPECT Imaging.* Ed. by A. Karellas and B. R. Thomadsen. CRC Press, Feb. 2017, p. 621. ISBN: 978-1-4665-6013-0. DOI: 10.1201/9781315374383. URL: https://www.taylorfrancis.com/books/9781466560147.

[12] *The Nobel Prize in Chemistry. Lecture 1904 | Sir William Ramsay.* Accessed June 6, 2023. URL: https://www.nobelprize.org/prizes/chemistry/1904/ramsay/lecture/.

[13] "Noble Gases". In: *Encyclopedia of the Elements.* John Wiley Sons, Ltd, 2004. Chap. 51, pp. 1109–1140. ISBN: 9783527612338. DOI: https://doi.org/10.1002/9783527612338.ch51. eprint: https://onlinelibrary.wiley.com/doi/pdf/10.1002/9783527612338.ch51. URL: https://onlinelibrary.wiley.com/doi/abs/10.1002/9783527612338.ch51.

[14] N. N. Greenwood and A. Earnshaw. *Chemistry of the Elements.* Elsevier, 1997.

[15] G. Wang *et al.* "Design and fabrication of an LED lantern based on light condensing technology". In: *Journal of International Council on Electrical Engineering* 8 (1 Jan. 2018), pp. 14–18. DOI: 10.1080/22348972.2018.1436894.

[16] M. Frandina *et al.* "Status of the Next Ion Thruster Long Duration Test". In: (July 2005). DOI: 10.2514/6.2005-4065. URL: https://arc.aiaa.org/doi/10.2514/6.2005-4065.

[17] J. L. V. Noord. "Lifetime assessment of the NEXT ion thruster". In: *Collection of Technical Papers - 43rd AIAA/ASME/SAE/ASEE Joint Propulsion Conference* 3 (2007), pp. 2717–2740. DOI: 10.2514/6.2007-5274. URL: https://arc.aiaa.org/doi/10.2514/6.2007-5274.

[18] *NASA - Ion Propulsion | NASA.* Accessed June 2, 2023. URL: https://www.nasa.gov/centers/glenn/about/fs21grc.html.

[19] J. Aalbers *et al.* "A next-generation liquid xenon observatory for dark matter and neutrino physics". In: *Journal of Physics G: Nuclear and Particle Physics* 50 (1 Jan. 2023), p. 013001. ISSN: 0954-3899. DOI: 10.1088/1361-6471/ac841a. URL: https://iopscience.iop.org/article/10.1088/1361-6471/ac841a.

[20] Y. Tolaymat *et al.* "Inhaled Gases for Neuroprotection of Neonates: A Review". In: *Frontiers in Pediatrics* 7 (Jan. 2020). DOI: 10.3389/fped.2019.00558. URL: https://doi.org/10.3389/fped.2019.00558.

[21] M. Ebert *et al.* "Nuclear magnetic resonance imaging with hyperpolarised helium-3". In: *The Lancet* 347.9011 (May 1996), pp. 1297–1299. DOI: 10.1016/s0140-6736(96)90940-x. URL: https://doi.org/10.1016/s0140-6736(96)90940-x.

[22] J. R. MacFall *et al.* "Human lung air spaces: potential for MR imaging with hyperpolarized He-3." In: *Radiology* 200.2 (Aug. 1996), pp. 553–558. DOI: 10.1148/radiology.200.2.8685356. URL: https://doi.org/10.1148/radiology.200.2.8685356.

[23] J. P. Mugler *et al.* "MR imaging and spectroscopy using hyperpolarized ^{129}Xe gas: Preliminary human results". In: *Magnetic Resonance in Medicine* 37.6 (June 1997), pp. 809–815. DOI: 10.1002/mrm.1910370602. URL: https://doi.org/10.1002/mrm.1910370602.

[24] H. Marshall *et al.* "In vivo methods and applications of ^{129}Xe magnetic resonance". In: *Progress in Nuclear Magnetic Resonance Spectroscopy* 122 (Feb. 2021), pp. 42–62. DOI: 10.1016/j.pnmrs.2020.11.002. URL: https://doi.org/10.1016/j.pnmrs.2020.11.002.

[25] L. Cander. "Solubility of inert gases in human lung tissue". In: *Journal of Applied Physiology* 14.4 (July 1959), pp. 538–540. DOI: 10.1152/jappl.1959.14.4.538. URL: https://doi.org/10.1152/jappl.1959.14.4.538.

[26] P. K. Weathersby and L. D. Homer. “Solubility of inert gases in biological fluids and tissues: a review”. en. In: *Undersea Biomed. Res.* 7.4 (Dec. 1980), pp. 277–296.

[27] J. Ladefoged and A. M. Andersen. “Solubility of ^{133}Xe at $37deg$C in Water, Saline, Olive Oil, Liquid Paraffin, Solutions of Albumin, and Blood”. In: *Physics in Medicine and Biology* 12.3 (July 1967), pp. 353–358. DOI: 10.1088/0031-9155/12/3/307. URL: https://doi.org/10.1088/0031-9155/12/3/307.

[28] J. P. Mugler and T. A. Altes. “Hyperpolarized ^{129}Xe MRI of the human lung”. In: *Journal of Magnetic Resonance Imaging* 37.2 (Jan. 2013), pp. 313–331. DOI: 10.1002/jmri.23844. URL: https://doi.org/10.1002/jmri.23844.

[29] M. S. Albert *et al. Magnetic resonance imaging using hyperpolarized noble gases.* Patent number: US5789921A . Assignees: Research Foundation of State University of New York, Princeton University. Application filed: 1995-06-07. Published: 1998-08-04.

[30] M. Kirby *et al.* “Hyperpolarized ^{129}Xe MR Imaging in Healthy Volunteers and Patients with Chronic Obstructive Pulmonary Disease”. In: *Radiology* 265.2 (Nov. 2012), pp. 600–610. DOI: 10.1148/radiol.12120485. URL: https://doi.org/10.1148/radiol.12120485.

[31] J. P. Mugler *et al.* “Simultaneous magnetic resonance imaging of ventilation distribution and gas uptake in the human lung using hyperpolarized ^{129}Xe”. In: *Proceedings of the National Academy of Sciences* 107.50 (Nov. 2010), pp. 21707–21712. DOI: 10.1073/pnas.1011912107. URL: https://doi.org/10.1073/pnas.1011912107.

[32] Z. Wang *et al.* “Using hyperpolarized ^{129}Xe gas-exchange MRI to model the regional airspace, membrane, and capillary contributions to diffusing capacity”. In: *Journal of Applied Physiology* 130.5 (May 2021), pp. 1398–1409. DOI: 10.1152/japplphysiol.00702.2020. URL: https://doi.org/10.1152/japplphysiol.00702.2020.

[33] J. T. Grist *et al.* “Hyperpolarized ^{129}Xe MRI Abnormalities in Dyspneic Patients 3 Months after COVID-19 Pneumonia: Preliminary Results”. In: *Radiology* 301.1 (Oct. 2021), E353–E360. DOI: 10.1148/radiol.2021210033. URL: https://doi.org/10.1148/radiol.2021210033.

[34] J. T. Grist *et al.* “Lung Abnormalities Detected with Hyperpolarized ^{129}Xe MRI in Patients with Long COVID”. In: *Radiology* 305.3 (Dec. 2022), pp. 709–717. DOI: 10.1148/radiol.220069. URL: https://doi.org/10.1148/radiol.220069.

[35] *Xenon Drug Classification | FDA.* https://drugs.ncats.io/drug/3H3U766W84. Accessed: 2023-06-11.

[36] R. D. Sanders, D. Ma, and M. Maze. “Xenon: elemental anaesthesia in clinical practice”. In: *British Medical Bulletin* 71 (1 Jan. 2005), pp. 115–135. ISSN: 1471-8391. DOI: 10.1093/bmb/ldh034. URL: https://academic.oup.com/bmb/article/71/1/115/276002.

[37] J. Jayapaul and L. Schröder. “Molecular Sensing with Host Systems for Hyperpolarized ^{129}Xe”. In: *Molecules* 25.20 (Oct. 2020), p. 4627. DOI: 10.3390/molecules25204627. URL: https://doi.org/10.3390/molecules25204627.

[38] N. Li *et al.* “Nuclear Spin Attenuates the Anesthetic Potency of Xenon Isotopes in Mice”. In: *Anesthesiology* 129.2 (Aug. 2018), pp. 271–277. DOI: 10.1097/aln.0000000000002226. URL: https://doi.org/10.1097/aln.0000000000002226.

[39] N. P. Franks *et al.* “How does xenon produce anaesthesia?” In: *Nature* 396 (6709 Nov. 1998), pp. 324–324. ISSN: 0028-0836. DOI: 10.1038/24525. URL: https://www.nature.com/articles/24525.

[40] B. W. Roose, S. D. Zemerov, and I. J. Dmochowski. *Xenon–Protein Interactions: Characterization by X-Ray Crystallography and Hyper-CEST NMR.* 2018. DOI: 10.1016/bs.mie.2018.02.005. URL: https://linkinghub.elsevier.com/retrieve/pii/S0076687918300612.

[41] K. Aoki *et al.* “Generation of ventilation/perfusion ratio map in surgical patients by dual-energy CT after xenon inhalation and intravenous contrast media”. In: *Journal of Cardiothoracic Surgery* 13 (1 May 2018). ISSN: 17498090. DOI: 10.1186/s13019-018-0737-2.

[42] I. V. Baldon *et al.* “The extravasation of contrast as a predictor of cerebral hemorrhagic contusion expansion, poor neurological outcome and mortality after traumatic brain injury: A systematic review and meta-analysis”. In: *PLOS ONE* 15.7 (July 2020). Ed. by J. H. Sherman, e0235561. DOI: 10.1371/journal.pone.0235561. URL: https://doi.org/10.1371/journal.pone.0235561.

[43] X. Kong *et al.* “Xenon-Enhanced Dual-Energy CT Lung Ventilation Imaging: Techniques and Clinical Applications”. In: *American Journal of Roentgenology* 202.2 (Feb. 2014), pp. 309–317. DOI: 10.2214/ajr.13.11191. URL: https://doi.org/10.2214/ajr.13.11191.

[44] J. K. Goodrich *et al.* “^{133}Xe measurement of regional ventilation”. In: *Radiology* 103 (3 1972), pp. 611–619. ISSN: 0033-8419. DOI: 10.1148/103.3.611. URL: https://pubmed.ncbi.nlm.nih.gov/5022960/.

[45] G. J. Bouma and J. P. Muizelaar. “Evaluation of Regional Cerebral Blood Flow in Acute Head Injury by Stable Xenon-Enhanced Computerized Tomography”. In: *Monitoring of Cerebral Blood Flow and Metabolism in Intensive Care.* Springer Vienna, 1993, pp. 34–40. DOI: 10.1007/978-3-7091-9302-0_6. URL: https://doi.org/10.1007/978-3-7091-9302-0_6.

[46] R. Ansorge and M. Graves. *The Physics and Mathematics of MRI.* Morgan Claypool Publishers, 2016. ISBN: 978-1-6817-4068-3. DOI: 10.1088/978-1-6817-4068-3. URL: http://dx.doi.org/10.1088/978-1-6817-4068-3.

[47] S. R. C.O. Mariager. “Hyperpolarized xenon by d-DNP using the clinical GE SpinLab polarizer system”. In: 2017.

[48] A. Capozzi *et al.* “Optimal Glass-Forming Solvent Brings Sublimation Dynamic Nuclear Polarization to ^{129}Xe Hyperpolarization Biomedical Imaging Standards”. In: *The Journal of Physical Chemistry C* 119.9 (Feb. 2015), pp. 5020–5025. DOI: 10.1021/jp5124053. URL: https://doi.org/10.1021/jp5124053.

[49] A. Comment *et al.* “Hyperpolarizing Gases via Dynamic Nuclear Polarization and Sublimation”. In: *Physical Review Letters* 105.1 (July 2010). DOI: 10.1103/physrevlett.105.018104. URL: https://doi.org/10.1103/physrevlett.105.018104.

[50] T. G. Walker and W. Happer. “RMP Colloquia Spin-exchange optical pumping of noble-gas nuclei”. In: (1997).

[51] M. Kitano *et al.* “Measurement of magnetic dipole moments of ^{129m}Xe and ^{131m}Xe by spin exchange with optically pumped Rb”. In: *Physical Review C* 34 (5 1986).

[52] C. J. Flower. “Observation of Rb Clusters in ^{129}Xe Spin-Exchange Optical Pumping Cells By Electron Microscopy by Abstract Observation of Rb Clusters in ^{129}Xe Spin-Exchange Optical Pumping Cells By Electron Microscopy by”. In: (2016).

[53] I. A. Nelson. “Physics of practical spin-exchange optical pumping”. In: *Ph.D. Thesis* (2001), p. 1908. URL: https://ui.adsabs.harvard.edu/abs/2001PhDT........15N.

[54] C. V. Rice and D. Raftery. “Rubidium-xenon spin exchange and relaxation rates measured at high pressure and high magnetic field”. In: *Journal of Chemical Physics* 117 (12 2002), pp. 5632–5641. ISSN: 00219606. DOI: 10.1063/1.1500733.

[55] M. Kelley and R. T. Branca. “Theoretical models of spin-exchange optical pumping: Revisited and reconciled”. In: *Journal of Applied Physics* 129 (15 Apr. 2021). ISSN: 10897550. DOI: 10.1063/5.0037440.

[56] B. N. Berry-Pusey *et al.* “Nuclear spin relaxation of ^{129}Xe due to persistent xenon dimers”. In: (). DOI: 10.1103/PhysRevA.74.063408.

[57] B. Chann *et al.* “^{129}Xe-Xe Molecular Spin Relaxation”. In: *Physical Review Letters* 88 (11 Feb. 2002), p. 113201. DOI: 10.1103/PhysRevLett.88.113201. URL: https://link.aps.org/doi/10.1103/PhysRevLett.88.113201.

[58] K. Jackowski and M. Jaszunski, eds. *Gas Phase NMR*. Royal Society of Chemistry, Feb. 2016. ISBN: 978-1-78262-161-4. DOI: 10.1039/9781782623816. URL: http://ebook.rsc.org/?DOI=10.1039/9781782623816.

[59] Z. I. Cleveland *et al.* “Hyperpolarized ^{83}Kr and ^{129}Xe NMR Relaxation Measurements of Hydrated Surfaces: Implications for Materials Science and Pulmonary Diagnostics”. In: (2007). DOI: 10.1021/ja065994t. URL: https://pubs.acs.org/sharingguidelines.

[60] N. J. Rogers *et al.* “Molecular hydrogen and catalytic combustion in the production of hyperpolarized ^{83}Kr and ^{129}Xe MRI contrast agents”. In: *Proceedings of the National Academy of Sciences of the United States of America* 113 (12 2016), pp. 3164–3168. ISSN: 10916490. DOI: 10.1073/pnas.1600379113.

[61] M. Raftery. *Optical pumping and xenon NMR*. Lawrence Berkeley National Laboratory (LBNL), Nov. 1991. DOI: 10.2172/6653527. URL: http://www.osti.gov/servlets/purl/6653527-JyxHTw/.

[62] G. D. Cates *et al.* “Laser production of large nuclear-spin polarization in frozen xenon”. In: *Physical Review Letters* 65.20 (Nov. 1990), pp. 2591–2594. DOI: 10.1103/physrevlett.65.2591. URL: https://doi.org/10.1103/physrevlett.65.2591.

[63] M. Gatzke *et al.* “Extraordinarily slow nuclear spin relaxation in frozen laser-polarized ^{129}Xe”. In: *Physical Review Letters* 70.5 (Feb. 1993), pp. 690–693. DOI: 10.1103/physrevlett.70.690. URL: https://doi.org/10.1103/physrevlett.70.690.

[64] R. J. Fitzgerald *et al.* “^{129}Xe spin relaxation in frozen xenon”. In: *Physical Review B* 59.13 (Apr. 1999), pp. 8795–8811. DOI: 10.1103/physrevb.59.8795. URL: https://doi.org/10.1103/physrevb.59.8795.

[65] K. Sauer, R. Fitzgerald, and W. Happer. “Laser-polarized liquid xenon”. In: *Chemical Physics Letters* 277.1-3 (Oct. 1997), pp. 153–158. DOI: 10.1016/s0009-2614(97)00876-2. URL: https://doi.org/10.1016/s0009-2614(97)00876-2.

[66] M. V. Romalis and M. P. Ledbetter. “Transverse Spin Relaxation in Liquid ^{129}Xe in the Presence of Large Dipolar Fields”. In: *Physical Review Letters* 87.6 (July 2001). DOI: 10.1103/physrevlett.87.067601. URL: https://doi.org/10.1103/physrevlett.87.067601.

[67] N. Stone. *TABLE OF NUCLEAR ELECTRIC QUADRUPOLE MOMENTS IAEA Nuclear Data Section.* 2021. URL: http://www-nds.iaea.org/publications.

[68] K. F. Stupic *et al.* “Hyperpolarized ^{131}Xe NMR spectroscopy”. In: *Journal of Magnetic Resonance* 208.1 (2011), pp. 58–69. ISSN: 10907807. DOI: 10.1016/j.jmr.2010.10.004.

[69] W. W. Warren and R. E. Norberg. “Nuclear quadrupole relaxation and chemical shift of ^{131}Xe in liquid and solid xenon”. In: *Physical Review* 148 (1 1966), pp. 402–412. ISSN: 0031899X. DOI: 10.1103/PhysRev.148.402.

[70] H. A. Fogarty *et al.* “A Cryptophane Core Optimized for Xenon Encapsulation”. In: *Journal of the American Chemical Society* 129.34 (Aug. 2007), pp. 10332–10333. DOI: 10.1021/ja073771c. URL: https://doi.org/10.1021/ja073771c.

[71] J. Timar, Z. Elekes, and B. Singh. “Nuclear Data Sheets for A = 129”. In: *Nuclear Data Sheets* 121 (Sept. 2014), pp. 143–394. ISSN: 00903752. DOI: 10.1016/j.nds.2014.09.002.

[72] Y. Khazov, I. Mitropolsky, and A. Rodionov. “Nuclear Data Sheets for A = 131”. In: *Nuclear Data Sheets* 107.11 (Nov. 2006), pp. 2715–2930. ISSN: 0090-3752. DOI: 10.1016/J.NDS.2006.10.001.

[73] Y. Khazov, A. Rodionov, and F. G. Kondev. “Nuclear Data Sheets for A = 133”. In: *Nuclear Data Sheets* 112 (4 Apr. 2011), pp. 855–1113. ISSN: 00903752. DOI: 10.1016/j.nds.2011.03.001.

[74] E. Lopienska. *The CERN accelerator complex, layout in 2022.* https://cds.cern.ch/record/2800984. accessed on 24 July 2023.

[75] M. Kowalska. *The many faces of isolde. EP News.* https://ep-news.web.cern.ch/content/many-faces-isolde. accessed on 24 July 2023.

[76] J. P. Ramos Pintos. “Titanium carbide-carbon porous nanocomposite materials for radioactive ion beam production: processing, sintering and isotope release properties”. Presented 26 Jan 2017. 2017. URL: https://cds.cern.ch/record/2243566.

[77] *Reactor safety FAQ.* https://www.ill.eu/reactor-and-safety/safety/reactor-safety-faq. accessed on 24 July 2023.

[78] J. Salacz. “Reprocessing of irradiated ^{235}U for the production of ^{99}Mo, ^{131}I and ^{133}Xe radioisotopes”. In: *Fission molybdenum for medical use. Proceedings of a technical committee meeting organized by the IAEA 1987.* International Atomic Energy Agency (IAEA). 1989.

[79] A. Abragam and W. G. Proctor. “Spin Temperature”. In: *Phys. Rev.* 109 (5 Mar. 1958), pp. 1441–1458. DOI: 10.1103/PhysRev.109.1441. URL: https://link.aps.org/doi/10.1103/PhysRev.109.1441.

[80] G. Neyens. *Nuclear magnetic and quadrupole moments for nuclear structure research on exotic nuclei.* 2003, pp. 633–689.

[81] K. Alder and A. Winter. *Electromagnetic Excitation.* North-Holland, Amsterdam, 1975. ISBN: 0720402883. URL: http://inis.iaea.org/search/search.aspx?orig_q=RN:07232300.

[82] M. Kowalska. “Ground state properties of neutron-rich Mg isotopes: The ’island of inversion’ studied with laser and beta-NMR spectroscopy”. PhD thesis. University of Mainz, 2006.

[83] Y. Zheng. “Low Field MRI and the Development of Polarized Nuclear Imaging (PNI) — A New Imaging Modality.” In: *Ph.D. Thesis* (2014 2015).

[84] A. M. Oros and N. J. Shah. “Hyperpolarized xenon in NMR and MRI”. In: *Physics in Medicine and Biology* 49 (20 2004). ISSN: 00319155. DOI: 10.1088/0031-9155/49/20/R01.

[85] G. Crișan *et al.* “Radiopharmaceuticals for PET and SPECT Imaging: A Literature Review over the Last Decade”. In: *International Journal of Molecular Sciences* 23 (9 May 2022). ISSN: 14220067. DOI: 10.3390/ijms23095023.

[86] Y. Zheng and Z. Zhou. “SPECT and PET in Vascular Dementia”. In: *PET and SPECT in Neurology*. Springer International Publishing, 2021, pp. 563–575. ISBN: 978-3-030-53167-6. DOI: 10.1007/978-3-030-53168-3_18. URL: http://link.springer.com/10.1007/978-3-030-53168-3_18.

[87] D. Wisser and M. Hartmann. “^{129}Xe NMR on Porous Materials: Basic Principles and Recent Applications”. In: *Advanced Materials Interfaces* 8 (4 Feb. 2021). ISSN: 21967350. DOI: 10.1002/admi.202001266.

[88] M. Boventi, M. Mauri, and R. Simonutti. “^{129}Xe Xe: A Wide-Ranging NMR Probe for Multiscale Structures”. In: *Applied Sciences (Switzerland)* 12 (6 Mar. 2022). ISSN: 20763417. DOI: 10.3390/app12063152.

[89] T. G. Walker and W. Happer. “Spin-exchange optical pumping of noble-gas nuclei”. In: *Rev. Mod. Phys.* 69 (2 Apr. 1997), pp. 629–642. DOI: 10.1103/RevModPhys.69.629.

[90] M. R. Rao *et al.* “Measuring ^{129}Xe transfer across the blood-brain barrier using MR spectroscopy”. In: *Magnetic Resonance in Medicine* 85.6 (June 2021), p. 2939. ISSN: 15222594. DOI: 10.1002/MRM.28646.

[91] P. Berthault and C. Boutin. “Biosensing and study of biological cells using hyperpolarized ^{129}Xe”. In: *New Developments in NMR* 2015-Janua.4 (2015), pp. 261–271. ISSN: 20442548. DOI: 10.1039/9781782628378-00261.

[92] A. Kimura, H. Imai, and H. Fujiwara. “Continuous flow and dissolved phase ^{129}Xe NMR/MRI for quantification in preclinical study as well as materials science”. In: *New Developments in NMR* 2015-Janua.4 (2015), pp. 301–316. ISSN: 20442548. DOI: 10.1039/9781782628378-00301.

[93] L. Q. Wang. “Hyperpolarized ^{129}Xe NMR in materials sciences: Pore structure, interconnectivity and functionality”. In: *New Developments in NMR* 2015-Janua.4 (2015), pp. 142–163. ISSN: 20442548. DOI: 10.1039/9781782628378-00142.

[94] K. Yokoe *et al.* “Usefulness of ^{99m}Tc-Technegas and ^{133}Xe dynamic SPECT in ventilatory impairment”. In: *Nuclear Medicine Communications* 27.11 (2006), pp. 887–892. ISSN: 14735628. DOI: 10.1097/01.MNM.0000239484.76651.6F.

[95] “Chapter 10 - Pulmonary System”. In: *Nuclear Medicine (Fourth Edition)*. Ed. by H. A. Ziessman, J. P. O’Malley, and J. H. Thrall. Fourth Edi. Philadelphia: W.B. Saunders, 2014, pp. 204–226. ISBN: 978-0-323-08299-0. DOI: https://doi.org/10.1016/B978-0-323-08299-0.00010-9.

[96] *GAMMA-MRI project website.* https://gamma-mri.eu. accessed on 30 August 2022.

[97] *The Supply of Medical Radioisotopes. Interim Report of the OECD/NEA High-level Group on Security of Supply of Medical Radioisotopes.* Tech. rep. Organisation for Economic Co-operation and Development, Nuclear Energy Agency (NEA), 2010. URL: www.oecd-nea.org.

[98] *Manual on Therapeutic Uses of Iodine-131, Practical Radiation Safety Manual No. 6.* Tech. rep. International Atomic Energy Agency (IAEA), 1996.

[99] *Molybdenum-99 for Medical Imaging.* Tech. rep. National Academies of Sciences, Engineering, and Medicine, Oct. 2016, pp. 1–245. DOI: 10.17226/23563. URL: https://www.nap.edu/catalog/23563.

[100] P. Bedrossian, G. Tóth, and L. Zsinka. “Herstellung von tragerarmem ^{131m}Xe durch eine Adsorptionsmethode”. In: *Isotopenpraxis. Isotopes in Environmental and Health Studies* 4.3 (1968), pp. 117–118. ISSN: 0021-1915. DOI: 10.1080/10256016808551947.

[101] McFarland. “An Improved Generator of ^{131m}Xe”. In: *International Journal of Applied Radiation and Isotopes* 25.1311 (1974), pp. 567–568.

[102] Y. Zheng *et al.* “A method for imaging and spectroscopy using γ-rays and magnetic resonance”. In: *Nature* 537.7622 (2016), pp. 652–655.

[103] H. Bateman. *The solution of a system of differential equations occurring in the theory of radioactive transformations. Vol. 15.* Proc. Cambridge Philos. Soc, 1910, pp. 423–427.

[104] G. Nahler. “European Pharmacopoeia (Eur Ph)”. In: *Dictionary of Pharmaceutical Medicine* (2009), pp. 69–69. DOI: 10.1007/978-3-211-89836-9_515.

[105] Curium Pharma. *Private correspondence.* May 2021.

[106] *Specification sheet of DT5730 / DT5730S 8 Channel 14 bit 500 MS/s Digitizer from CAEN.* https://www.caen.it/products/dt5730/. Accessed: 2022-08-30.

[107] Livi, R. *MAESTRO Multi-Channel Analyzer Software User’s Manual.* AMETEK ORTEC Inc. Vienna, Austria, 2007.

[108] D. E. Raeside and J. Brnetich. “A High-Resolution γ-Ray Spectrum of Background Radiation”. In: *American Journal of Physics* 39.11 (July 2005), p. 1396. ISSN: 0002-9505. DOI: 10.1119/1.1976670. URL: https://aapt.scitation.org/doi/abs/10.1119/1.1976670.

[109] Committee on Thyroid Screening Related to I-131 Exposure, Institute of Medicine, and Committee on Exposure of the American People to I-131 from the Nevada Atomic Bomb Tests, National Research Council. “Health Risks of I-131 Exposure”. In: *Exposure of the American People to Iodine-131 from Nevada Nuclear-Bomb Tests: Review of the National Cancer Institute Report and Public Health Implications.* National Academies Press (US), 1999. Chap. 3, pp. 45–55. ISBN: 0-309-52248-X. URL: http://www.nap.edu/catalog/6283.html.

[110] L. A. Currie. “Limits for Qualitative Detection and Quantitative Determination: Application to Radiochemistry”. In: *Analytical Chemistry* 40.3 (1968), pp. 586–593. ISSN: 15206882. DOI: 10.1021/ac60259a007.

[111] Mirion Technologies (Canberra) 2017. *Spectrum Analysis Manual.* "https://www.canberra.com/literature/fundamental-principles/pdf/Spectrum-Analysis.pdf". Accessed: 2022-08-01. (Visited on 08/01/2022).

[112] *Xenon* ^{133}*Xe Gas Factsheet.* Curium US LLC. 2018, pp. 1–2.

[113] *Xenon* ^{133}*Xe Gas Factsheet.* Nordion Inc. 2016, pp. 1–2.

[114] *Xenon* ^{133}*Xe Gas Factsheet.* March. Lantheus Medical Imaging Inc. 2018, pp. 1–2.

[115] *Gamma-MRI: the future of molecular imaging. Grant agreement ID: 964644.* GAMMA-MRI collaboration. 2021.

[116] *Ordonnance du 26 avril 2017 sur la radioprotection (ORaP). Etat le 1er janvier 2022.* Le Conseil fédéral suisse.

[117] *Manual for Reactor Produced Radioisotopes.* TECDOC Series 1340. Vienna: International Atomic Energy Agency, 2003. ISBN: 92-0-101103-2. URL: https://www.iaea.org/publications/6407/manual-for-reactor-produced-radioisotopes.

[118] *GAMMA-MRI collaboration website.* https://gamma-mri.eu. Accessed: 2023-07-26. GAMMA-MRI collaboration.

[119] H. Guyon and P. Geltenbort. “The high flux research reactor at the Laue-Langevin Institute (ILL)”. In: *Atw Internationale Zeitschrift fuer Kernenergie* 57.10 (57 2012).

[120] M. Migdal *et al.* “MARIA Reactor Irradiation Technology Capabilities towards Advanced Applications”. In: *Energies* 14.23 (2021). URL: https://doi.org/10.3390/en14238153.

[121] W. Stacey. *Nuclear Reactor Physics, 3rd edition.* John Wiley Sons, 2018.

[122] S. Mughabghab. “Atlas of Neutron Resonances (6th edition), Volume 1: Resonance Properties and Thermal Cross Sections Z= 1-60”. In: *National Nuclear Data Center, Brokhaven National Laboratory* (2018). DOI: 10.1016/C2015-0-00522-6.

[123] *Extended Range Coaxial Ge Detectors.* https://www.gammadata.se/assets/Uploads/XtRa-detectors-C49310.pdf. Accessed: 2023-05-20. Mirion Technologies (Canberra), Inc.

[124] *Practical Aspects of operating a neutron activation analysis laboratory.* TECDOC Series 564. Vienna: International Atomic Energy AgencyY, 1990. ISBN: 1011-4289. URL: https://www-pub.iaea.org/MTCD/publications/PDF/te_564_web.pdf.

[125] J. Cetnar. “General solution of Bateman equations for nuclear transmutations”. In: *Annals of Nuclear Energy - ANN NUCL ENERG* 33 (May 2006), pp. 640–645. DOI: 10.1016/j.anucene.2006.02.004.

[126] *IAEA - Human Health Campus website*. https://humanhealth.iaea.org/HHW/. Accessed: 2023-08-01. Internation Atomic Energy Agency.

[127] T. O. Niinikoski. *The Physics of Polarized Targets*. Cambridge University Press, Jan. 2020. DOI: 10.1017/9781108567435. URL: https://doi.org/10.1017/9781108567435.

[128] H. Postma and N. Stone. *Low-temperature nuclear orientation*. North-Holland, 1986.

[129] K. S. Krane. *Introductory Nuclear Physics*. 3rd. 1987. ISBN: 1118210093. URL: https://www.wiley.com/en-us/Introductory+Nuclear+Physics,+3rd+Edition-p-9780471805533.

[130] L. C. Biedenharn and M. E. Rose. “Theory of Angular Correlation of Nuclear Radiations”. In: *Reviews of Modern Physics* 25 (3 July 1953), pp. 729–777. ISSN: 0034-6861. DOI: 10.1103/RevModPhys.25.729. URL: https://link.aps.org/doi/10.1103/RevModPhys.25.729.

[131] H. Feshbach. “A unified theory of nuclear reactions. II”. In: *Annals of Physics* 19 (2 Aug. 1962), pp. 287–313. ISSN: 00034916. DOI: 10.1016/0003-4916(62)90221-X. URL: https://linkinghub.elsevier.com/retrieve/pii/000349166290221X.

[132] M. E. Rose. “The Analysis of Angular Correlation and Angular Distribution Data”. In: *Physical Review* 91 (3 Aug. 1953), pp. 610–615. ISSN: 0031-899X. DOI: 10.1103/PhysRev.91.610. URL: https://link.aps.org/doi/10.1103/PhysRev.91.610.

[133] A. Abragam and R. V. Pound. “Influence of Electric and Magnetic Fields on Angular Correlations”. In: *Physical Review* 92 (4 Nov. 1953), pp. 943–962. ISSN: 0031-899X. DOI: 10.1103/PhysRev.92.943. URL: https://link.aps.org/doi/10.1103/PhysRev.92.943.

[134] F. P. Calaprice *et al.* “Nuclear alignment and magnetic moments of ^{133}Xe, $^{133\mathrm{m}}$Xe, and $^{131\mathrm{m}}$Xe by spin exchange with optically pumped Rb87”. In: *Physical Review Letters* 54 (3 Jan. 1985), pp. 174–177. ISSN: 00319007. DOI: 10.1103/PhysRevLett.54.174.

[135] M. Kitano *et al.* “Nuclear orientation of radon isotopes by spin-exchange optical pumping”. In: *Physical Review Letters* 60.21 (May 1988), pp. 2133–2136. ISSN: 00319007. DOI: 10.1103/PhysRevLett.60.2133. URL: https://journals.aps.org/prl/abstract/10.1103/PhysRevLett.60.2133.

[136] Y. Zheng *et al.* “A method for imaging and spectroscopy using γ-rays and magnetic resonance”. In: *Nature* 537.7622 (Sept. 2016), pp. 652–655. ISSN: 0028-0836. DOI: 10.1038/nature19775. URL: http://www.nature.com/articles/nature19775.

[137] R. Y. Engel. “Planing, Simulation and Preparation of a Magnetic Resonant Imaging Experiment based on the Detection of Anisotropic gamma-Radiation from Hyperpolarized Isomers”. Presented 03 Jul 2018. 2018. URL: https://cds.cern.ch/record/2638538.

[138] G. Norquay *et al.* “^{129}Xe-Rb Spin-Exchange Optical Pumping with High Photon Efficiency”. In: *Physical Review Letters* 121 (15 2018), p. 153201. ISSN: 10797114. DOI: 10.1103/PhysRevLett.121.153201. URL: https://doi.org/10.1103/PhysRevLett.121.153201.

[139] P. Nikolaou *et al.* “Near-unity nuclear polarization with an open-source ^{129}Xe hyperpolarizer for NMR and MRI”. In: *Proceedings of the National Academy of Sciences of the United States of America* 110.35 (Aug. 2013), pp. 14150–14155. ISSN: 00278424. DOI: 10.1073/PNAS.1306586110/ASSET/32E4FF7C-0DF9-49FF-82AE-2FE25B549080/ASSETS/GRAPHIC/PNAS.1306586110EQ7.JPEG.

[140] H. A. Tolhoek and J. A. Cox. “Angular distribution and polarization of gamma radiation emitted by aligned radioactive nuclei”. In: *Physica* 18.5 (1952), pp. 357–358. ISSN: 00318914. DOI: 10.1016/S0031-8914(52)80159-4.

[141] M. García-Díez *et al.* “Evaluation of newest SiPM from SensL and Hamamatsu for energy and time resolution when coupled to LYSO, CeGAGG, PrLUAG and other scentillators”. In: *Contribution to IEEE Nuclear Science Symposium and Medical Imaging Conference 2018.* 2018.

[142] V. Sánchez-Tembleque. “Acquisition systems and state-of-art radiation detectors for basic nuclear physics and medical imaging”. PhD thesis. Universidad Complutense de Madrid.

[143] P. T. Ltd. *Ultra-compact PC oscilloscopes PicoScope ® 2000 Series.* Tech. rep. 2000. URL: https://www.picotech.com/download/datasheets/picoscope-2000-series-data-sheet.pdf.

[144] J. R. Birchall *et al.* “Helium-rich mixtures for improved batch-mode clinical-scale spin-exchange optical pumping of ^{129}Xe”. In: *Journal of Magnetic Resonance* 315 (2020), p. 106739. ISSN: 1090-7807. DOI: https://doi.org/10.1016/j.jmr.2020.106739. URL: https://www.sciencedirect.com/science/article/pii/S1090780720300574.

[145] T. Palasz *et al.* “Stop-Flow SEOP Polarizer for ^{129}Xe”. In: *Acta Physica Polonica A* 136 (Dec. 2019), pp. 1008–1017. DOI: 10.12693/APhysPolA.136.1008.

[146] I. Michelson. “Production of metastable Xenon isotopes for a new medical imaging modality, Gamma-MRI”. PhD thesis. University of Padova, 2022.

[147] M. Chojnacki. “Intense and pure samples of ^{129m,131m,133m}Xe for a novel medical imaging technique, gamma-MRI”. In: *Isolde Workshop and Users Meeting 2022.* 2022. URL: https://indico.cern.ch/event/1183259/contributions/5110851/attachments/2558836/4410257/ChojnackiMateusz_ISOLDEWORKSHOP2022.pdf.

[148] M. Chojnacki and M. Kowalska. *Addendum to the ISOLDE and Neutron Time-of-Flight Committee. Collection of ^{129m,131m,133m}Xe for the gamma-MRI project: IS691.* URL: https://cds.cern.ch/record/2845996/files/INTC-P-598-ADD-1.pdf.

[149] G. Norquay *et al.* “Optimized production of hyperpolarized ¹²⁹ Xe at 2 bars for <i>in vivo</i> lung magnetic resonance imaging”. In: *Journal of Applied Physics* 113.4 (Jan. 2013), p. 044908. ISSN: 0021-8979. DOI: 10.1063/1.4776763. URL: http://aip.scitation.org/doi/10.1063/1.4776763.

[150] M. J. G. Borge and B. Jonson. “ISOLDE past, present and future”. In: *Journal of Physics G: Nuclear and Particle Physics* 44.4 (Mar. 2017), p. 044011. DOI: 10.1088/1361-6471/aa5f03. URL: https://dx.doi.org/10.1088/1361-6471/aa5f03.